Tethered UAV Flight using a Spherical Position Controller

by

Michael R. Klinker

B.S., Aeronautics and Astronautics
Massachusetts Institute of Technology (2014)

Submitted to the Department of Aeronautics and Astronautics
in partial fulfillment of the requirements for the degree of

Masters of Science in Aeronautical and Astronautical Engineering

at the

MASSACHUSETTS INSTITUTE OF TECHNOLOGY

June 2016

Author .... Signature redacted ....
Department of Aeronautics and Astronautics
May 19, 2016

Certified by .... Signature redacted ....
Jonathan P. How
Richard C. Maclaurin Professor of Aeronautics and Astronautics
Thesis Supervisor

Accepted by .... Signature redacted ....
Paulo C. Lozano
Associate Professor of Aeronautics and Astronautics
Chairman, Graduate Program Committee

Tethered UAV Flight using a

Spherical Position Controller

by

Michael R. Klinker

Submitted to the Department of Aeronautics and Astronautics
on May 19, 2016, in partial fulfillment of the
requirements for the degree of
Masters of Science in Aeronautical and Astronautical Engineering

Abstract

In recent years, the aerospace community has seen a rise in the popularity of multirotor unmanned aircraft. This increase in popularity is in part due to the ability of a multirotor aircraft to hover, its simple dynamics, and its mechanical simplicity. Operating these unmanned aircraft indoors or outdoors is a well understood challenge, however these aircraft have predominantly been operated in an unconstrained area. This thesis investigates how to control a multirotor aircraft in a constrained environment, such as on the end of a tether. A position controller is presented for a multirotor UAV operating on the end of a fixed length, tensioned tether in spherical coordinates, which utilizes the vehicles relative position and tether dynamics to calculate control inputs and ensure flight stability. The proposed position controller was put through a series of verification and validation tests using both a simulated tether-aircraft system, as well as a quadrotor flown in the RAVEN indoor flight space in the MIT Aerospace Controls Laboratory. During simulated flight testing the spherical position controller showed a 35.7% decrease in tether tension, and during indoor flight testing the spherical position controller exhibited an 8.4% decrease in power consumption over the traditional Cartesian position controller while operating on the end of a fixed length tether.

Thesis Supervisor: Jonathan P. How
Title: Richard C. Maclaurin Professor of Aeronautics and Astronautics

This page intentionally left blank

Acknowledgments

First and foremost I would like to thank my advisor, Professor Jonathan How, for his support and guidance throughout my undergraduate and graduate studies. He has been an exceptional mentor, contributing thoughtful feedback and ensuring I maintain focus on solving the problems at hand and their relation to the big picture of my work.

This thesis was based upon work funded by Creare, LLC as part of the AeroWake project. I would like to acknowledge Creare for their support of this research project, and thank Ben Cameron, John Walthour, Matt Ueckermann, and the other individuals involved with the AeroWake project. Working with them has been a pleasure and I appreciate their willingness to help foster my education.

I would also like to thank all the members of the Aerospace Controls Lab. Their passion, knowledge, and work ethic constantly inspired me, and I feel honored to have been a member of the team. In particular, I would like to thank Mark Cutler for introducing me to the lab and aerospace controls as an undergraduate, and Brett Lopez for his support and friendship, whether it be solving software bugs or assisting with flight testing.

Lastly, I owe my final thanks to my family and friends. Without their encouragement, guidance, and support, I could not have achieved the highs nor endured the lows of my undergraduate and graduate studies over the past six years at the Massachusetts Institute of Technology.

This page intentionally left blank

Contents

This page intentionally left blank

List of Figures

List of Tables

Chapter 1

Introduction

1.1 Project Overview

The spherical position controller presented in this thesis was designed and developed for a unmanned aircraft that flies behind a moving ship on the end of tether. The purpose for this system is to survey the air wake behind a large ship utilizing a multi-directional pitot tube payload. The tether for this unmanned aircraft system served two important roles: to allow the forward motion of the ship to pull the aircraft, and allow a simple method of launch and recovery of the aircraft from a moving platform.

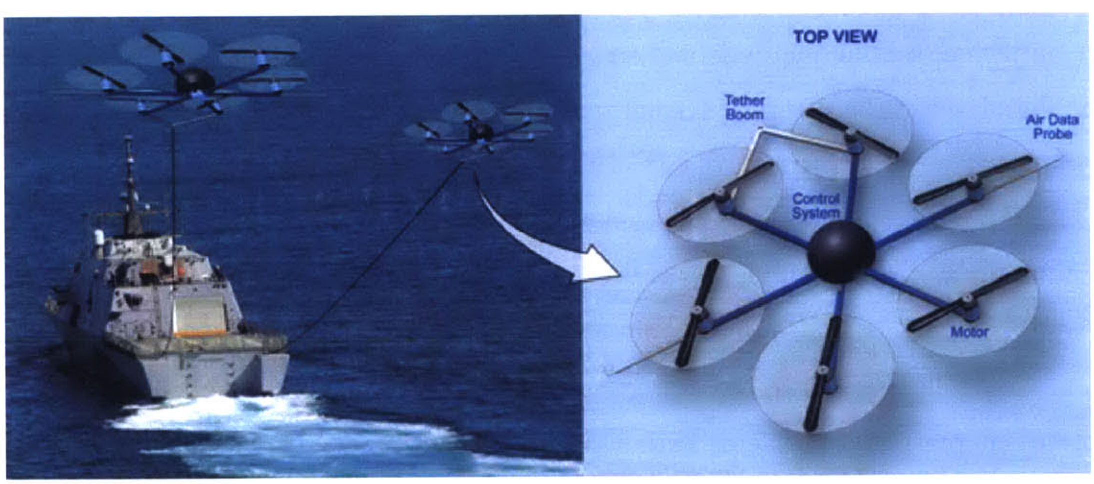

Figure 1-1: Operating UAV Multirotor behind Ship [7]

The introduction of a tether to the multirotor aircraft system introduced a variety of complex dynamics and constraints onto the aircraft. The controller design and testing in this thesis was aimed at creating a position controller capable of compensating for the tether system specific to this project. However the of this work is relevant to any scenario where it is desired to fly a multirotor aircraft on a tether.

Chapter 2 provides a full derivation of a multirotor aircraft rigid-body dynamics, and a derivation of the tether system shape and dynamics. These dynamics models will serve as the foundation of the position control system. The multirotor dynamics will be used primarily for vehicle attitude control, and the tether dynamics will be used for both reference command generation and tether dynamics feed forward control of the vehicles position.

Chapter 3 discusses the problem with traditional position control systems operating on the end of a tether and presents the proposed spherical position control system as the sum of three major components, each solving a specific problem with the traditional system. These three major components are the spherical PID/PD controller, a tether dynamics feed forward model, and a reference command generation algorithm. This proposed controller uses a typical attitude control system, which is also presented in this chapter.

Chapter 4 presents the methods of implementing the proposed controller for simulated and indoor flight verification and validation testing, covering the tether dynamics numerical solving methods and testing infrastructure. This chapter discusses the simulated vehicle and tether system, as well as the hardware used for indoor flight testing.

The experimental design and results of the proposed spherical position controller simulation and indoor flight testing is presented in Chapters 5 and 6 respectively. These chapters are broken into two major sections, controller verification and validation. Controller verification tests were established to ensure the controller components solved the presented problems with a traditional position control system. Controller validation tests were designed to ensure that the position controller remained stable and operated as expected in the presence of external disturbances and modeling error.

1.2 Motivation

In recent years, the aerospace community has seen a rise in the popularity of multirotor unmanned aircraft. This increase in popularity is in part due to a multirotor aircraft's hover ability, simple dynamics, and mechanical simplicity [3]. Operating these unmanned aircraft indoors or outdoors is a well understood challenge, and a significant amount of work has focused on exploring different flight envelopes for multirotor aircraft [16]. However a majority of this work involves aircraft operating in an unconstrained environment. Multirotor aircraft operating in an unconstrained environment are able to translate along all three Cartesian axes, and their position controllers are designed for free movement in space.

Flying on the end of a fixed length tether is an interesting regime for multirotors, and recent work has shown interest in this new flight regime [13]. There are a variety of applications where a tether can be advantageous, such as restricting a UAV's area of operation [9], using the tether to transmit power to the aircraft [17], or pulling the UAV behind a moving vehicle.

A significant problem arises when a multirotor that is equipped with an unconstrained space flight controller is used to operate in a constrained space. If the vehicle attempts to fly outside of the constrained space, the constraint is imposed, and the controller will be unable to reach its goal location. Even if the multirotor attempts to fly along the constrained surface, any small attempts to deviate outside the constrained space can yield lowered efficiency and potential instability. There are also significant challenges of controlling the aircraft in the presence of wind, as wind effects both the dynamics of the aircraft and tether system. The goal for the new position control algorithm proposed in this thesis is to allow the UAV to fly along a constrained three-dimensional surface without sacrificing vehicle power efficiency, positional accuracy, or most importantly, flight stability.

1.3 Literature Review

Multirotor aircraft, or quadrotors, have been an increasing common aircraft for recreation and research [3]. Their flight dynamics are well understood and well documented, making them an ideal candidate for a controls research platform. Their dynamics can often be approximated to be linear under slow flight conditions [18], however recent works have shown advanced non-linear dynamics models and control techniques [6, 16].

Recent research has shown interest in tethered flight of multirotor aircraft, as there is a variety of applications where tethered aircraft can useful. Lupashin et al. presents a position estimation method of a quadrotor operating as a kite [9]. This paper presents a novel method of determining the relative location of a multirotor and ground station connected via a tether utilizing an onboard inertial measurement unit, specifically an accelerometer. They utilize a proportional-derivative (PD) controller on position, a choice which removes error integration and eliminates a major problem with operating a PID controller on a tether. This problem will be discussed in Chapter 3, however removing error integration from the position controller makes the controller susceptible to steady state error due to modeling inaccuracies and external forces. This work also assumes that the tether has negligible mass and is straight, which an invalid assumption for longer tether lengths. While the proposed system does present an interesting method for relative position estimation, the real world application is limited due to the omission of error integrators and tension requirement for state estimation.

Another interest for tethered multirotors is to use the tether system to provide electrical power to the vehicle, allowing the vehicle to use a large ground-based power source to prolong flight time. Yibo et al. proposes a tether model that allows the use of a powered mooring tether [17]. The paper discusses methods for mooring a quadrotor and a model for an un-tensioned tether, however it does not address the condition where quadrotor intersects the boundary of the tether. This paper presents tether-vehicle dynamics, but does not address controlling the vehicle with the augmented tether dynamics. However the idea of powering a unmanned aircraft via a tether system is a high-interest topic, as it would allow the aircraft to fly for long periods of time without battery capacity limitations [15].

Previous work has presented tether-driven control systems [13] [14]. While this work corresponds to stabilizing helicopter unmanned aircraft on a tether, the control architecture is applicable to multirotor aircraft. A focus of this work is to stabilize the aircraft with respect to the moment forces on the aircraft due to tether dynamics, however the tension in the tether is assumed observable through a sensor on the ground. This work also fails to evaluate the system in the presence of disturbances, such as wind or modeling error.

1.4 Contributions

The main contributions of this thesis are the design, implementation, and testing of a position control algorithm for a multirotor UAV that operates on the end of a fixed length tether. This control system is comprised of three major components: a spherical PID/PD controller, a tether dynamics feed forward model, and a reference command generation method. Each of these components plays a critical role in controlling the interaction between the multirotor aircraft, the environment, and the tether system. This proposed controller solved the problems associated with a nominal Cartesian-based position controller operating on a tether, and showed a 8.4% decrease in power consumption over the nominal controller during indoor flight testing.

This page intentionally left blank

Chapter 2

Dynamics Model

This section will review the derivation for the dynamics of a multirotor at hover conditions in a Cartesian coordinate system. It will then discuss the dynamics of a tether system in a Cartesian coordinate system. These dynamics models will transformed into spherical coordinates and used by the spherical coordinate position controller in Chapter 3.

2.1 Multirotor Rigid Body Dynamics Model Derivation

The free-body diagram displayed in Figure 2-1 shows the forces acting upon a multirotor that is operating near hover conditions. There are two reference frames used when describing a multirotors position. The inertial reference frame I is centered at the origin O, and has unit vectors $(\mathbf{i_x}, \mathbf{i_y}, \mathbf{i_z})$. The body reference frame B is centered at the origin Q, and has unit vectors $(\mathbf{b_x}, \mathbf{b_y}, \mathbf{b_z})$. A multirotor with four motors, also referred to as a quadrotor, has four internal forces $(\mathbf{F_1}, \mathbf{F_2}, \mathbf{F_3}, \mathbf{F_4})$ and one external force $\mathbf{F_g}$ in standard hover conditions. With the presence of a tether on the multirotor, there are three additional forces acting upon the multirotor, $(\mathbf{F_{T,x}}, \mathbf{F_{T,y}}, \mathbf{F_{T,z}})$, in the inertial frame. These forces are described in Section 2.2.

The inertial orientation of the body frame is described using the 3-2-1 Euler angle

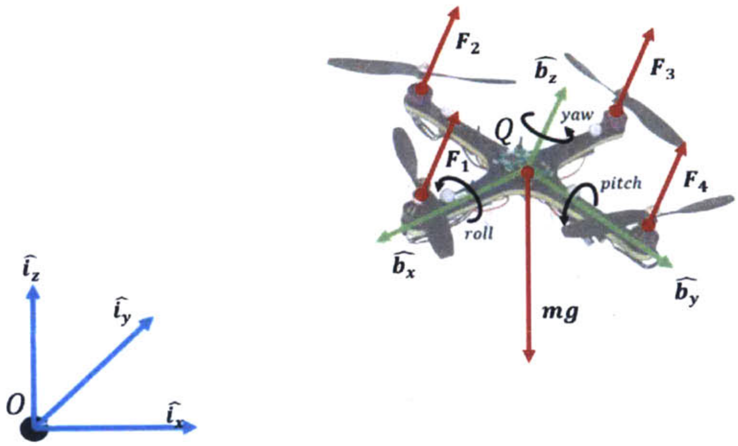

Figure 2-1: Multirotor Free Body Diagram at Hover Operating Conditions [16]

sequence: yaw (Ψ), pitch (Θ), then roll (Φ). The following equation is the transformation matrix from the body frame to the inertial frame:

$$^{I}R^{B} = \begin{bmatrix} c\Theta c\Psi & s\Phi s\Theta c\Psi - c\Phi s\Psi & c\Phi s\Theta c\Psi + s\Phi s\Psi \\ c\Theta s\Psi & s\Phi s\Theta s\Psi + c\Phi c\Psi & c\Phi s\Theta s\Psi + s\Phi c\Psi \\ -s\Theta & s\Phi c\Theta & c\Phi c\Theta \end{bmatrix}, \tag{2.1}$$

where $c\Theta$ and $s\Theta$ are abbreviations for $\cos\Theta$ and $\sin\Theta$, respectively. This abbreviation applies for the other Euler angles, Φ and Ψ.

The derivation for the equations of translational motion begins with Newton's 2nd Law:

$$\sum F = ma \tag{2.2}$$

As previously stated, there are four internal forces acting on the aircraft, and four external forces with the presence of a tether. The force due to gravity always points in the negative $\mathbf{i}_z$ direction. The four motor thrust forces all point in the $\mathbf{b}_z$ direction. The tether forces act in the inertial frame I. Newton's 2nd Law can be rewritten into translational equations of motion for the multirotor:

$$m \begin{bmatrix} \ddot{x} \\ \ddot{y} \\ \ddot{z} \end{bmatrix} = {}^{I}R^{B} \begin{bmatrix} 0 \\ 0 \\ F_{total} \end{bmatrix}_B - \begin{bmatrix} F_{T,x} \\ F_{T,y} \\ F_{T,z} + mg \end{bmatrix}_I \tag{2.3}$$

where F_{total} is the sum of the thrust forces, m is the mass of the aircraft, F_T is the force exerted on the aircraft by the tether system, and $\begin{bmatrix} \ddot{x} & \ddot{y} & \ddot{z} \end{bmatrix}^T$ is the second derivative of the position vector of the multirotor in the inertial frame $(\mathbf{p})$:

$$\mathbf{p} = x\mathbf{i}_x + y\mathbf{i}_y + z\mathbf{i}_z \tag{2.4}$$

The rotational equations of motion are derived from the rotational equivalent of Newton's 2nd Law:

$$\sum \tau = I\dot{\omega} \tag{2.5}$$

where τ is a torque, I is the inertia tensor, and $\dot{\omega}$ is the time derivative of the angular velocity of the multirotor body frame with respect to the inertial frame:

$$\omega = p\mathbf{b}_x + q\mathbf{b}_y + r\mathbf{b}_z \tag{2.6}$$

Note that rotation of the multirotor is defined about its center of mass. Thus torques are created from the thrust forces and the rotors spinning. Including these torques and rearranging gives the general form for the rotational equations of motion:

$$I\dot{\omega} = -\omega \times I\omega + \sum_{k=1}^{4} r_{k/cm} \times T_{k}. + \omega \times I_r\Omega \tag{2.7}$$

where I is the inertia tensor of the multirotor, I_r is the inertia tensor of the rotor, and $r_{k/cm}$ is the distance between the kth rotor and the center of mass of the quadrotor.

Multirotors are generally designed to be symmetric, and thus their inertia tensors are diagonal matrices. The rotor inertia tensors exhibit the same property.

$$I = \begin{bmatrix} I_x & 0 & 0 \\ 0 & I_y & 0 \\ 0 & 0 & I_z \end{bmatrix} \tag{2.8}$$

The rotational equations of motion are:

$$I_x \dot{p} = -(I_z - I_y)qr + d(F_3 - F_4) \tag{2.9}$$

$$I_y \dot{q} = -(I_x - I_z)rp + d(F_2 - F_1) \tag{2.10}$$

$$I_z \dot{r} = -(I_y - I_x)pq + c_m \sum_{k=1}^{4} F_k \tag{2.11}$$

where d is the distance from the rotor to the center of mass of the quadrotor and c_m is a constant relating the thrust force and the yawing moment caused by spinning the rotors. Note that for this model, the tether system that the multirotor is attached to is connected to its center of mass, and thus cannot generate a rotational moment on the airframe.

2.2 Tether Dynamics Model Derivation

This section will derive the forces exhibited onto a multirotor aircraft by a tether system, F_T, in the inertial frame. An assumption for a tether system used in previous work, as mentioned in Section 1.2, is that the tether is massless and perfectly straight. For the purpose of this project, a dynamics model for the tether with mass per unit length λ_m is used and hangs in a catenary curve. The objective of the tether dynamics model is to determine a the force exerted on a multirotor as a function of the aircrafts position and the tether length.

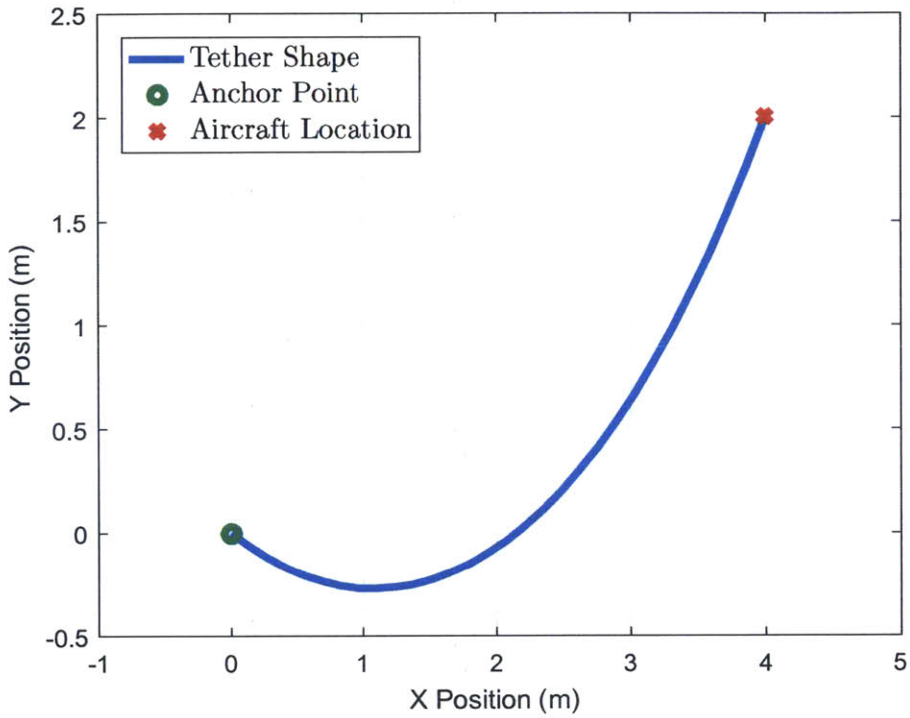

Figure 2-2: Example of a Catenary Curve with tether length $L = 5m$

2.2.1 Tether Shape Analysis

This derivation will begin with an analysis of the tethers shape, followed by a relation from this unique shape to the tension force in the tether. Tethers hang in a catenary curve under the downward force of gravity [8]. To begin, we can consider a 2 dimensional model for the tethers catenary curve. This model will be expanded to 3 dimensions and rotated into the inertial reference frame at the conclusion of the derivation.

The basic equation for a catenary curve is shown below. It has two free parameters, a and b, which determine the curvature and translation of the curve.

$$y(x; a, b) = a\left(\cosh\left(\frac{b+x}{a}\right) - \cosh\left(\frac{b}{a}\right)\right) \tag{2.12}$$

During operation, the aircrafts positional state and tether length are considered to be known values. Thus, we can define (X, Y), and L to be the known aircraft position and tether length respectively. In order to determine the two parameters a and b, we will set up a system of two equations: the catenary curve equation presented above, and the arclength of the catenary curve.

$$Y = a\left(\cosh\left(\frac{b+X}{a}\right) - \cosh\left(\frac{b}{a}\right)\right) \tag{2.13}$$

$$L = \int_0^X \sqrt{1+\left(\frac{dy}{dx}\right)^2}\, dx \tag{2.14}$$

$$\text{with } \frac{dy}{dx} = \sinh\left(\frac{b+x}{a}\right) \tag{2.15}$$

Analytically evaluating the integral for arc length at its limits yields the following simplified systems of equations. These two equations in this system are both transcendental equations in a and must be solved numerically. Discussion of the methods used to solve these equations numerically will be discussed in Section 4.

$$Y = a\left(\cosh\left(\frac{b+X}{a}\right) - \cosh\left(\frac{b}{a}\right)\right) \tag{2.16}$$

$$L = a\tanh\left(\frac{b+X}{a}\right)\sqrt{1+\sinh^2\left(\frac{b+X}{a}\right)} - a\tanh\left(\frac{b}{a}\right)\sqrt{\cosh^2\left(\frac{b}{a}\right)} \tag{2.17}$$

2.2.2 Tether Tension Force Balance

In the case of a tether hanging under the force of gravity as shown in Figure 2-2 and 2-3, there is an equilibrium of horizontal tension force at the point on the tether where $\frac{dy(x)}{dx} = 0$. Shown in Figure 2-3, this point X_c is the inflection point of the curve. At this point, $F_{\text{t,right}} = F_{\text{t,left}}$ and the vertical component of tension $F_{\text{T,y}} = 0$. Conveniently, the point X_c is equal to the negative of the catenary curve parameter b, such that $X_c = -b$.

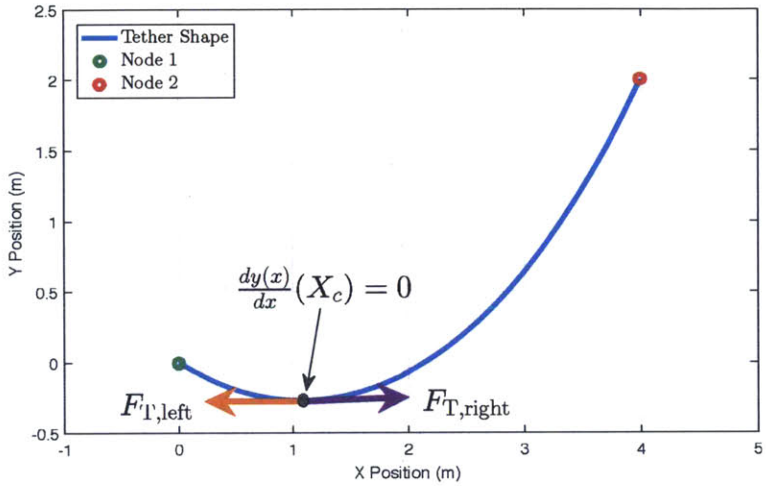

Figure 2-3: Horizontal Force Equilibrium at $\frac{dy}{dx} = 0$ in a Tether

The vertical components of tension $F_{\mathrm{T1,y}}$ at node 1 and $F_{\mathrm{T2,y}}$ at node 2 in Figure 2-3 can be conceptually described as the weight of the tether to the left and right of X_c respectively. Thus, the vertical components of tension at nodes 1 and 2 equate to:

$$F_{\mathrm{T1,y}} = -\lambda_m g \int_0^{X_c} \sqrt{1 + (\frac{dy}{dx})^2} dx \tag{2.18}$$

$$F_{\mathrm{T2,y}} = -\lambda_m g \int_{X_c}^{X} \sqrt{1 + (\frac{dy}{dx})^2} dx \tag{2.19}$$

$$\text{with } y(x; a, b) = a \left(\cosh\left(\frac{b+x}{a}\right) - \cosh\left(\frac{b}{a}\right) \right) \tag{2.20}$$

$$\text{and } \frac{dy}{dx} = \sinh\left(\frac{b+x}{a}\right) \tag{2.21}$$

The vertical component of tension at the aircraft, $F_{\mathrm{T2,y}}$, can be directly related to the total tension force exerted onto the aircraft, as well as the horizontal component of the tension force $F_{\mathrm{T2,x}}$ through the tethers angle of arrival γ.

$$\gamma = \arctan\left(\frac{dy(X)}{dx}\right) = \arctan\left(\sinh\left(\frac{b+X}{a}\right)\right) \tag{2.22}$$

And thus utilizing the previously computed $F_{\mathrm{T2,y}}$,

$$F_{\mathrm{T2}} = \frac{F_{\mathrm{T2,y}}}{\sin \gamma} \tag{2.23}$$

$$F_{\mathrm{T2,x}} = -F_{\mathrm{T2}} \cos \gamma \tag{2.24}$$

From the above derived tension forces exerted at the aircraft, shown as node 2 in Figure 2-3, along with an understanding of the shape of a catenary curve, a few important observations can be made about the tension force as a function of the aircrafts position (X, Y) and the tether length L. As X_c approaches the location of the aircraft X, the vertical component of tension $F_{\mathrm{T2,y}}$ approaches zero. However physically, due to the catenary curve this would require the aircrafts location be below the tether attachment point. If the aircraft is constrained such that $Y \geq 0$, we can find the minimum vertical force force component of tension for a given $X > 0$ is $F_{\mathrm{T2,y}} = \frac{L\lambda g}{2}$, or half of the mass of the tether. In this case if the attachment point is at the origin $(0, 0)$, the catenary curve sags such that the tether hangs below the attachment location, $y(X_c) < 0$. Fundamentally, a positive X_c will yield less force on the vehicle, however the tether will be in contact with the ground. A negative X_c will result in additional tension force, and ultimately undesired. The effect of varying X_c is shown in Figure 2-4

If we place boundaries on the aircrafts state and the shape of the tether (specifically X_c), we can create an ideal tether operating case given a radially constrained location from the origin, where the tether is under minimum tension and above the attachment point (not in contact with the floor).

$$Y > 0$$

$$X > 0$$

$$X_c = 0$$

When imposing the condition that $X_c = 0$, there is a problem as the aircraft attempts to land. It can be seen that the tension in the tether approaches ∞. This unbounded

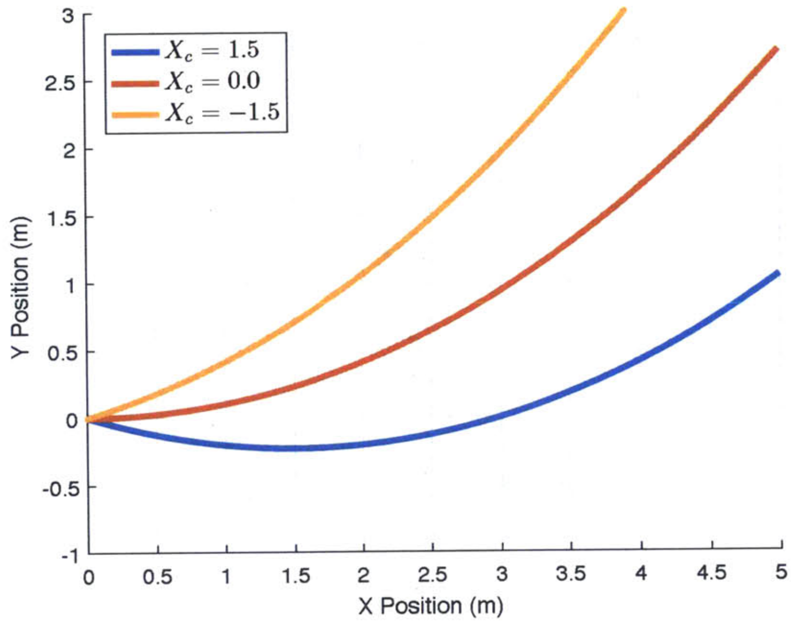

Figure 2-4: Impact on catenary curve while varying X_c

force of tension can be attributed to the fact that as the aircraft descends towards the ground, in order to maintain $X_c = 0$, the tether must have less curvature in order to not contact the ground. From the equation of the catenary curve, this is represented by a decrease in the a parameter.

$$\lim_{y \to 0} a(y; X, X_c) = 0 \tag{2.25}$$

$$\lim_{y \to 0} F_{\text{T2}} = \infty \tag{2.26}$$

Thus it is reasonable to place a lower bound of the catenary parameter a, by which places an upper bound on the force exerted by the aircraft to keep the tether off the ground. This presents a conflict: when this constraint is imposed, the tether dynamics and tether shape will be inconsistent. One solution to this is to use the following constraint

$$X_c \geq 0 \iff 0 < a \leq a_{\text{crit}} \tag{2.27}$$

which allows the lowest point on the tether, $y(X_c)$, to become positive during this

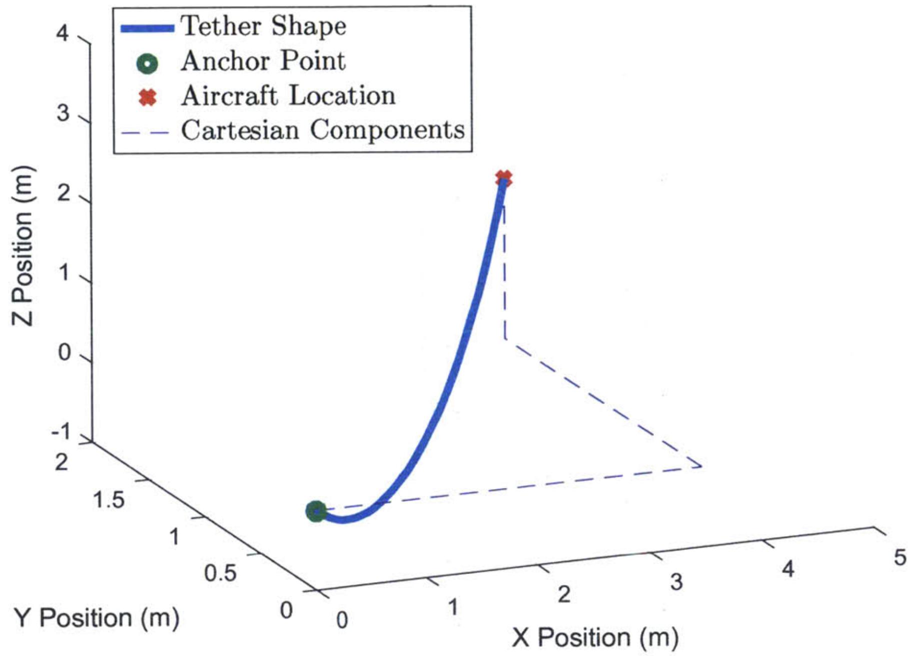

Figure 2-5: Example of a 3D Catenary Curve with tether length $L = 5.5m$ and $\phi = 30$deg

critical state, reducing the tension force within reasonable bounds set by a_{crit}.

2.2.3 Coordinate System Transformation

The previous analysis was performed in two dimensions. In order to transform this tether model into the aircrafts inertial frame of reference, a two axis solution to the tether dynamics can be rotated about $\mathbf{I_z}$ by ϕ to create a three axis solution. This transformation is shown below, and depicted in Figure 2-5.

$$z(x_r; a, b) = a\left(\cosh\left(\frac{b + x_r}{a}\right) - \cosh\left(\frac{b}{a}\right)\right) \tag{2.28}$$

$$\text{with } x_r = \sqrt{X^2 + Y^2} \tag{2.29}$$

The final force components of tension on the multirotor in the inertial reference frame can be resolved using the following equations. Note that $F_{\text{T,z}}$ is calculated first, followed by the total force of tension and the subsequent components.

$$F_{\mathrm{T,z}} = -\lambda_m g L \Big|_{X_c}^{x_r} \tag{2.30}$$

$$F_{\mathrm{T}} = \frac{F_{\mathrm{T,z}}}{\sin\gamma} \tag{2.31}$$

$$F_{\mathrm{T,x}} = -F_{\mathrm{T}} \cos\left(\arctan\left(\frac{Y}{X}\right)\right) \tag{2.32}$$

$$F_{\mathrm{T,y}} = -F_{\mathrm{T}} \sin\left(\arctan\left(\frac{Y}{X}\right)\right) \tag{2.33}$$

2.3 Summary

This section reviewed the free body dynamics of a multirotor aircraft in hover conditions in a Cartesian coordinate system, followed by the dynamics and equations describing a tether system. These two dynamics will form the underlying models for the spherical position controller that is presented in Chapter 3.

This page intentionally left blank

Chapter 3

Spherical Position Controller

This section will motivate and propose a position control system for a multirotor UAV that is operating on the end of a tether. This position controller utilizes a spherical coordinate system, a PID/PD controller, tether dynamics feed forward control, and specialized reference command generation method.

3.1 Motivation

The primary motivation behind designing a spherical coordinate position controller for a multirotor flying on a tether is an inherit problem with the traditional Cartesian PID position controller. This problem is that the Cartesian controller will exert an increasing force on the tether if the tether does not allow the aircraft to reach a desired reference location. This unnecessary force against the tether is generated by the control systems error integrators. Fundamentally, due to the tether dynamics, pulling harder on a tether will not yield significant radial displacement, while requiring excessive power by the aircraft. As the Cartesian position control axes do not align with the tether during operation, i.e. the direction of the tether $\hat{R}$ has X, Y, Z components, it is difficult to remove the components of error integration in the R direction. Removing all error integration to mitigate this problem will render the controller unable to reduce steady state error in directions not constrained by the tether system.

Another motivation behind designing the controller in spherical coordinates is for intuitive operation. During normal operation, the tether of length L can be described to span from the systems origin to the aircraft. Thus, it is intuitive to describe the location of the aircraft as a distance R from the origin (where $R < L$), with angular displacements ϕ and θ, such that the aircraft flies along a vector $\hat{R}$.

The following chapter will describe the proposed spherical position control system. For reference, a complete traditional Cartesian PID controller is derived in Appendix A.

3.2 Spherical Coordinate System

The proposed position control system operates using a spherical coordinate system. This coordinate system is a logical choice for a tethered multirotor, as the tether aligns with the $\hat{R}$ direction and the directions $\hat{\phi}$ and $\hat{\theta}$ are not constrained by the tether. During operation behind a ship or other moving vehicle, this coordinate system is rotated and translated relative to the back of the vehicle. For the scope of this derivation and flight testing, the coordinate system is fixed, however the flight control algorithm is extensible to a moving, relative coordinate system.

To convert a position (x, y, z) from Cartesian to spherical coordinates (ϕ, θ, r), the following formulae is used

$$r = \sqrt{x^2 + y^2 + z^2} \tag{3.1}$$

$$\theta = \arccos(\frac{z}{r}) \tag{3.2}$$

$$\phi = \arctan(\frac{y}{x}) \tag{3.3}$$

To convert a position (ϕ, θ, r) from spherical to Cartesian coordinates (x, y, z), the

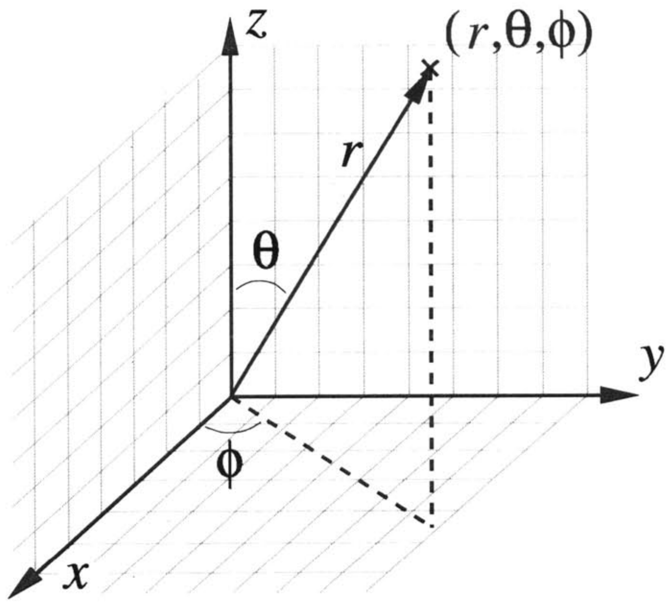

Figure 3-1: Spherical Coordinate System

following formulae is used

$$x = r \sin\theta \cos\phi \tag{3.4}$$

$$y = r \sin\theta \sin\phi \tag{3.5}$$

$$z = r \cos\theta \tag{3.6}$$

Converting velocity components $(\dot{x}, \dot{y}, \dot{z})$ from Cartesian to spherical is derived by taking the time derivative of the Cartesian to spherical coordinate conversion above. This conversion requires knowledge of the objects position (X, Y, Z).

$$\dot{\phi} = \frac{x\dot{y} - y\,\dot{x}}{x^2 + y^2} \tag{3.7}$$

$$\dot{\theta} = -\frac{x^2\,\dot{z} - z\,x\,\dot{x} + y^2\,\dot{z} - z\,y\,\dot{y}}{\sqrt{\frac{x^2+y^2}{x^2+y^2+z^2}}\,(x^2 + y^2 + z^2)^{\frac{3}{2}}} \tag{3.8}$$

$$\dot{r} = \frac{x\,\dot{x} + y\,\dot{y} + z\,\dot{z}}{\sqrt{x^2 + y^2 + z^2}} \tag{3.9}$$

Similarly, converting spherical velocity into Cartesian velocity components is accomplished by taking the time derivative of the conversion equations, listed as Equation 3.5-3.6 above.

$$\dot{x} = \sin(\phi)\ \sin(\theta)\ \dot{r} + \cos(\phi)\ \sin(\theta)\ r\dot{\phi} + \cos(\theta)\ \sin(\phi)\ r\dot{\theta} \tag{3.10}$$

$$\dot{y} = \sin(\phi)\sin(\theta)\dot{r} + \cos(\phi)\sin(\theta)r\dot{\phi} + \cos(\theta)\sin(\phi)r\dot{\theta} \tag{3.11}$$

$$\dot{z} = cos(\theta)\dot{r} - \sin(\theta)r\dot{\theta} \tag{3.12}$$

3.3 Reference Location

In order to fully utilize the tether dynamics as a feed forward control system, it is advantageous to use the tether dynamics in the reference location determination stage of control. According to the 3D tether dynamics presented in Chapter 2, for a tether length L, there is a horizontal distance X and altitude Z at which the multirotor should fly in order to minimize tether tension. Thus for a given tether length L and inclination angle θ, the optimal radial distance from the origin to minimize tether tension is calculable given a variety of operational constraints (keep tether off ground, altitude must be positive). The reference command generation algorithm takes $(\phi_{\text{ref}}, \theta_{\text{ref}}, L)$ as inputs, and outputs a desired R_{ref} that minimizes tether tension. The complete algorithm is shown below in Section 3.4.2.1 and the numerical solving method is presented in Chapter 4.

Knowledge of the constrained optimal tether operating conditions plays a significant role into how the reference commands for the spherical controller are used. When the tether dynamics model is used as a feed forward control term, the reference location for control is modified by the tether dynamics to yield the reference location that minimizes tether tension under the modeled conditions. As a result, the operator or path planning algorithm determines a desired $\hat{R}$ vector that the aircraft should fly upon, while the algorithm generates a distance R_{ref} to minimize tether tension subject to the constraints. The vector $\hat{R}_{\text{ref}}$ is specified through the two unconstrained state parameters ϕ_{ref} and θ_{ref}.

The PID/PD component of this position controller is fed two operator specified reference commands, ϕ_{ref} and θ_{ref}, as well as a calculated value R_{ref}. The $\hat{R}$ direction of this system is constrained by the tether system, and thus in order to reduce steady state error in R, the system runs a high risk of colliding with this constraint without absolute state knowledge, i.e. no modeling error. This condition is discussed in Section 3.1 as a leading motivation for developing this position controller. In order to avoid constrained operation, the reference command is given two degrees of freedom, $\hat{\phi}$ and $\hat{\theta}$. While the nominal system is expected to achieve zero steady state error in (ϕ, θ, R), the off-nominal system is expected to align the vehicles location with $\hat{R_{\text{ref}}}$ but to have steady state error in R.

3.4 Spherical Position Controller Design

3.4.1 Control Architecture

The control system architecture is designed to use two levels of successive feedback loop closure, and is similar to the algorithms presented in [3]. The outer most loop is the position control loop. This loop takes a reference position and tether length input of $(\phi_{\text{ref}}, \theta_{\text{ref}}, R_{\text{ref}})$, along with measured aircraft state information and tether dynamics model. It outputs a desired attitude to the inner control loop. The inner control loop is an attitude controller. This loop takes the output of the position controller (desired attitude) as inputs along with measured values for the attitude and angular rate of the quadrotor. Motor commands are the output of this control loop, which are fed into the equations of motion for a simulation, or the motor controllers for an hardware implementation. A top level block diagram of the system is shown in Figure 3-2 including high level inputs and outputs of each block.

3.4.2 Outer Loop Position Control

The following section describes the derivation of the proposed spherical coordinate position controller. This outer loop consists of three major components: the reference command generation, PID/PD controller, and the feed forward tether model.

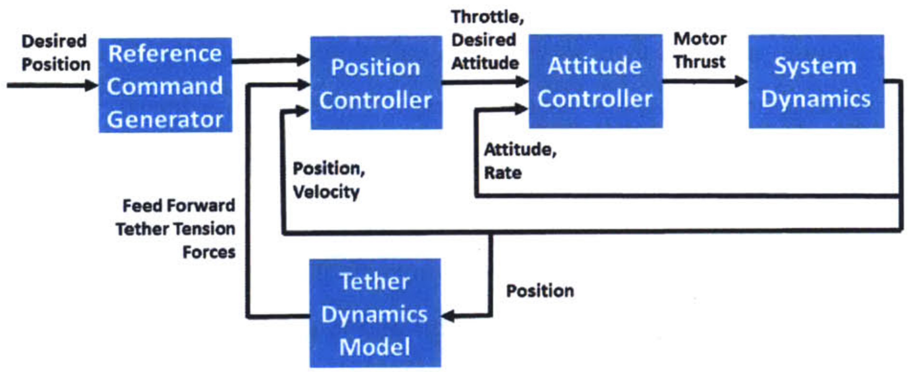

Figure 3-2: Block Diagram for the control system

3.4.2.1 Reference Command Generation

As discussed in Section 3.3, the reference locations ϕ_{ref} and θ_{ref} are set by the operator. The reference location R_{ref} is determined by solving the tether dynamics for the constrained minimum tension at $X_c = 0$, with the inputs $(\phi_{\text{ref}}, \theta_{\text{ref}}, L)$ and output R_{ref}. Due to the transcendental nature of the tether dynamics equations this algorithm must numerically solve the equations to a defined error tolerance, which is summarized in Chapter 4. With

$$F_{\text{A1}} = a\left(\cosh\left(\frac{\sqrt{R^2 - R^2\cos(\theta)^2}}{a}\right) - 1\right) - R\cos(\theta) \tag{3.13}$$

$$F_{\text{A2}} = a\sinh\left(\frac{\sqrt{R^2 - R^2\cos^2\theta}}{a}\right) - L \tag{3.14}$$

the algorithm for the reference command generation is shown below as Algorithm 1.

3.4.2.2 PID/PD Control on Reference Error

To compute the desired force vector, a position error vector (e_p) and a velocity error vector $(\dot{e_p})$ are calculated using the following method. Similar to a Cartesian position controller, this controller operates on the feedback of distance errors. In order to convert these errors to distances, the ϕ and θ components are multiplied by r to

Algorithm 1 Reference Command Generation

Input: θ_{ref}, ϕ_{ref}, L

Output: R_{ref}

$\mathbf{X_0} = \begin{bmatrix} a_0 = 1 \\ R_0 = L \end{bmatrix}$

while $e_{\text{tot}} < e_{\text{thres}}$ **do**

$\mathbf{X_k} = \begin{bmatrix} a_k \\ R_k \end{bmatrix}$

$\mathbf{J} = \begin{bmatrix} \frac{\partial F_{A1}}{\partial a} & \frac{\partial F_{A1}}{\partial R} \\ \frac{\partial F_{A2}}{\partial a} & \frac{\partial F_{A2}}{\partial R} \end{bmatrix} \Bigg|_{\mathbf{X_k}}$

$\mathbf{X_{k+1}} = \mathbf{X_k} - \mathbf{J}^{-1} \begin{bmatrix} F_{A1}(X_k; \theta_{\text{ref}}, L) \\ F_{A2}(X_k; \theta_{\text{ref}}, L) \end{bmatrix}$

$e_{\text{F}_{\text{A1}}}(X_{k+1}; \theta_{\text{ref}}, L) = F_{A1}(X_{k+1})$ (see equation 3.13)

$e_{\text{F}_{\text{A2}}}(X_{k+1}; \theta_{\text{ref}}, L) = F_{A2}(X_{k+1})$ (see equation 3.14)

$e_{\text{tot}} = \sqrt{e^2_{\text{F}_{\text{A1}}} + e^2_{\text{F}_{\text{A2}}}}$

end while

$R_{\text{ref}} = R_k$

generate an error arc length.

$$\mathbf{e}_{\text{pos}} = \begin{bmatrix} \phi r \\ \theta r \\ r \end{bmatrix}_{\text{desired}} - \begin{bmatrix} \phi r \\ \theta r \\ r \end{bmatrix}_{\text{measured}} \tag{3.15}$$

$$\dot{\mathbf{e}}_{\text{pos}} = \begin{bmatrix} \dot\phi r \\ \dot\theta r \\ \dot r \end{bmatrix}_{\text{desired}} - \begin{bmatrix} \dot\phi r \\ \dot\theta r \\ \dot r \end{bmatrix}_{measured} \tag{3.16}$$

The errors are mapped into acceleration commands using a PID controller for the unconstrained directions $\hat{\phi}$ and $\hat{\theta}$, and a PD controller in $\hat{R}$. This choice of only using a PD controller in the $\hat{R}$ direction was chosen to eliminate error integration is the direction of the tether, which was the primary problem the Cartesian PID position control system. The error integrators in the unconstrained directions allow the controller to eliminate steady state error in ϕ and θ, however the tradeoff for not integrating error in the direction constrained by the tether is that the controller will not be able to eliminate steady state error in R due to unmodeled disturbances or modeling errors.

$$\begin{bmatrix} \ddot{\phi}_{\text{cmd}} \\ \ddot{\theta}_{\text{cmd}} \end{bmatrix} = K_{\text{P,pos}} \mathbf{e}_{\text{pos}} + K_{\text{I,pos}} \int_0^t \mathbf{e}_{\text{pos}} + K_{\text{D,pos}} \dot{\mathbf{e}}_{\text{pos}} \tag{3.17}$$

$$\begin{bmatrix} \ddot{r}_{\text{cmd}} \end{bmatrix} = K_{\text{P,pos}} \mathbf{e}_{\text{pos}} + K_{\text{D,pos}} \dot{\mathbf{e}}_{\text{pos}} \tag{3.18}$$

where $K_{\text{P,pos}}$, $K_{\text{I,pos}}$, and $K_{\text{D,pos}}$ are positive definite gain matrices.

To map these desired accelerations to a desired attitude, these forces must be first transformed into Cartesian coordinates, then into the body frame of the multirotor. The transformation is

$$\ddot{x}_{\text{ctrl}} = -\ddot{\phi}_{\text{cmd}} \sin(\phi) \sin(\theta) + \ddot{\theta}_{\text{cmd}} \cos(\theta) \cos(\phi) + \ddot{r}_{\text{cmd}} \sin(\theta) \cos(\phi) \tag{3.19}$$

$$\ddot{y}_{\text{ctrl}} = \ddot{\phi}_{\text{cmd}} \cos(\phi) \sin(\theta) + \ddot{\theta}_{\text{cmd}} \sin(\theta) \sin(\phi) + \ddot{r}_{\text{cmd}} \sin(\theta) \sin(\phi) \tag{3.20}$$

$$\ddot{z}_{\text{ctrl}} = -\ddot{\theta}_{\text{cmd}} \sin(\theta) + \ddot{r} \cos(\theta) + g \tag{3.21}$$

Gravity is taken into account by adding g to the z component of acceleration. These three equations represent the desired acceleration from the position controller. According to Newton's second law, these accelerations can be multiplied by the vehicles mass m to generate the desired forces to be exerted on the aircrafts body.

$$\mathbf{F}_{\text{ctrl}} = \begin{bmatrix} F_{\text{ctrl,x}} \\ F_{\text{ctrl,y}} \\ F_{\text{ctrl,z}} \end{bmatrix} = \begin{bmatrix} \ddot{x}_{\text{ctrl}} \\ \ddot{y}_{\text{ctrl}} \\ \ddot{z}_{\text{ctrl}} \end{bmatrix} \mathbf{m} \tag{3.22}$$

These forces are designed and calculated to move the multirotor to a desired reference location in the absence of any additional inertial frame forces on the aircraft. With the presence of a tether, the controller must also compensate for the forces that the tether is exerting on the aircraft in order to reach its desired reference location. This controller uses a feed forward tether model to calculate and compensate for the tension force exerted on the aircraft by the tether, F_{T}.

3.4.2.3 Feed Forward Control for Tether Force Mitigation

This control system uses the derived tether model to predict the tether tension force that is acting upon the body of the quadrotor. Using the tether model from Chapter 2, the controller can predict that forces that it needs to exert to cancel out the forces due to the tension in the tether. The integrators I_ϕ and I_θ will then eliminate steady state error due to inaccuracies in the tether model, or other un-modeled disturbances. In the $\hat{R}$ direction, the PD controller with feed forward will not eliminate steady state error due to modeling errors in the tether dynamics, but compared to a scenario where the feed forward model is not used, this steady state error will be smaller.

The feed forward control term emanates from the tether dynamics. With aircraft state information (ϕ, θ, R), and tether length L, the dynamics can be solved to determine the force of tension in the tether and the direction it is acting upon the vehicle in the inertial frame. Due to the transcendental nature of the tether dynamics equations, the force of tension from the tether must be solved numerically to a predefined error tolerance. The complete algorithm is shown below as Algorithm 2, and the numerical methods of solving the tether dynamics are presented in Chapter 4. After solving for the tether physical properties using the specified algorithm, the force of tension is calculated using two parameters, L_{total} and X_c, that are dependent on the physical properties of the tether.

Note that in Algorithm 2,

$$F_{\text{B1}} = -a\left(\cosh\left(\frac{b}{a}\right) - \cosh\left(\frac{b + \sqrt{R^2 - R^2\cos(\theta)^2}}{a}\right)\right) - R\cos(\theta) \tag{3.23}$$

$$F_{\text{B2}} = 2\,a\sinh\left(\frac{\sqrt{R^2 - R^2\cos(\theta)^2}}{2\,a}\right)\cosh\left(\frac{2\,b + \sqrt{R^2 - R^2\cos(\theta)^2}}{2\,a}\right) - L \tag{3.24}$$

Algorithm 2 Feed Forward Tether Model

Input: θ, ϕ, R , L
Output: $\mathbf{F}_\mathrm{T}$

$\mathbf{X_0} = \begin{bmatrix} a_0 = 1 \\ b = 0 \end{bmatrix}$

while $e_\mathrm{tot} < e_\mathrm{thres}$ **do**

$\mathbf{X_k} = \begin{bmatrix} a_k \\ b_k \end{bmatrix}$

$\mathbf{J} = \begin{bmatrix} \frac{\partial F_{\mathrm{B1}}}{\partial a} & \frac{\partial F_{\mathrm{B1}}}{\partial b} \\ \frac{\partial F_{\mathrm{b2}}}{\partial a} & \frac{\partial F_{\mathrm{B2}}}{\partial b} \end{bmatrix} \Bigg|_{\mathbf{X_k}}$

$\mathbf{X_{k+1}} = \mathbf{X_k} - \mathbf{J}^{-1} \begin{bmatrix} F_{A1}(X_k; \theta_\mathrm{ref}, L) \\ F_{A2}(X_k; \theta_\mathrm{ref}, L) \end{bmatrix}$

$e_{\mathrm{F_{A1}}}(X_{k+1}; \theta_\mathrm{ref}, L) = F_{B1}(X_{k+1})$ (see equation 3.23)

$e_{\mathrm{F_{A2}}}(X_{k+1}; \theta_\mathrm{ref}, L) = F_{B2}(X_{k+1})$ (see equation 3.24)

$e_\mathrm{tot} = \sqrt{e^2_{\mathrm{F_{B1}}} + e^2_{\mathrm{F_{B2}}}}$

end while

$x_c = -b$

$L_\mathrm{total} = \int_0^{R \sin\theta \cos\phi} \sqrt{1 + (\frac{dy}{dx})^2} dx$

$m_\mathrm{total} = L_\mathrm{total} \lambda_\mathrm{m}$

$\alpha = \arctan(\sinh(\frac{b + R \sin\theta \cos\phi}{a}))$

$\mathbf{F}_\mathrm{T} = \frac{\mathbf{m_{total} g}}{\sin\alpha}$

Resulting in the components of the force of tension in the tether

$$F_{\mathrm{T,z}} = -\lambda_m g L_\mathrm{total} \Big|_{X_c}^{x_r} \tag{3.25}$$

$$F_{\mathrm{T,x}} = -|\mathbf{F}_\mathrm{T}| \cos \left(\arctan \left(\frac{\mathbf{Y}}{\mathbf{X}} \right) \right) \tag{3.26}$$

$$F_{\mathrm{T,y}} = -|\mathbf{F}_\mathrm{T}| \sin \left(\arctan \left(\frac{\mathbf{Y}}{\mathbf{X}} \right) \right) \tag{3.27}$$

Thus, the feed forward control forces $\mathbf{F}_\mathrm{FF}$ will be the negative vector to $\mathbf{F}_\mathrm{T}$, which will exactly cancel out the calculated forces due to the tether.

$$\begin{bmatrix} F_{\mathrm{FF,x}} \\ F_{\mathrm{FF,y}} \\ F_{\mathrm{FF,z}} \end{bmatrix} = - \begin{bmatrix} F_{\mathrm{T,x}} \\ F_{\mathrm{T,y}} \\ F_{\mathrm{T,z}} \end{bmatrix} \tag{3.28}$$

This feedforward control term is then added to the PID/PD controller forces, resulting in the controller desired force output F_{out}

$$\mathbf{F}_{\text{out}} = \mathbf{F}_{\text{ctrl}} + \mathbf{F}_{\text{FF}} \tag{3.29}$$

3.4.2.4 Attitude Generation

The final step of the outer control loop is to compute the desired attitude given the desired accelerations. This computation outputs the desired attitude in the inertial frame of reference. While not necessary, the multirotor can be rotated such that the front of the vehicle is aligned with the tether, given by Yaw $= -\phi$. In this case, the desired controller force commands must be rotated to account for this yaw command.

$$\begin{bmatrix} F'_{\text{out,x}} \\ F'_{\text{out,y}} \end{bmatrix} = \begin{bmatrix} \cos\phi & \sin\phi \\ -\sin\phi & \cos\phi \end{bmatrix} \begin{bmatrix} F_{\text{out,x}} \\ F_{\text{out,y}} \end{bmatrix} \tag{3.30}$$

where F'_{out} is the rotated force outputs of the controller. The final outputs of the outer loop controller are

$$\text{Throttle} = \sqrt{F_{\text{out,x}}^2 + F_{\text{out,y}}^2 + F_{\text{out,z}}^2} \tag{3.31}$$

$$\text{Roll} = \arctan\left(\frac{F_{\text{out,x}}}{F_{\text{out,z}}}\right) \tag{3.32}$$

$$\text{Pitch} = \arctan\left(\frac{F_{\text{out,y}}}{F_{\text{out,z}}}\right) \tag{3.33}$$

$$\text{Yaw} = 0 \text{ or } -\phi \tag{3.34}$$

These commands are then sent to the inner loop attitude controller. These inertial frame attitude commands are then converted to body frame commands as outlined in Section 3.4.3, and used to calculate motor commands.

3.4.3 Inner Loop Attitude Control

The attitude control loop (also referred to as the inner control loop) takes as inputs desired attitude from the outer control loop and measured attitude and angular rates from the system dynamics. Its purpose is to output motor commands to the system dynamics. For inputs Roll (Φ), Pitch (Θ), and Yaw (Ψ),

$$\mathbf{e}_{att} = \begin{bmatrix} \Phi_{des} \\ \Theta_{des} \\ \Psi_{des} \end{bmatrix} - \begin{bmatrix} \Phi_{meas} \\ \Theta_{meas} \\ \Psi_{meas} \end{bmatrix} \tag{3.35}$$

$$\dot{\mathbf{e}}_{att} = \begin{bmatrix} \dot{\Phi}_{des} \\ \dot{\Theta}_{des} \\ \dot{\Psi}_{des} \end{bmatrix} - \begin{bmatrix} \dot{\Phi}_{meas} \\ \dot{\Theta}_{meas} \\ \dot{\Psi}_{meas} \end{bmatrix} \tag{3.36}$$

where $\begin{bmatrix} \Phi_{des} & \Theta_{des} & \Psi_{des} \end{bmatrix}^T$ is the desired attitude vector, $\begin{bmatrix} \Phi_{meas} & \Theta_{meas} & \Psi_{meas} \end{bmatrix}^T$ is the measured attitude vector, $\begin{bmatrix} \dot{\Phi}_{des} & \dot{\Theta}_{des} & \dot{\Psi}_{des} \end{bmatrix}^T$ is the desired angular rate vector, and $\begin{bmatrix} \dot{\Phi}_{meas} & \dot{\Theta}_{meas} & \dot{\Psi}_{meas} \end{bmatrix}^T$ is the measured angular rate. The errors are mapped into roll, pitch, and yaw commands (Φ_{cmd}, Θ_{cmd}, and Ψ_{cmd}, respectively) using a PID controller

$$\begin{bmatrix} \Phi_{cmd} \\ \Theta_{cmd} \\ \Psi_{cmd} \end{bmatrix}^T = K_{P,att}\mathbf{e}_{att} + K_{I,att}\int_0^t \mathbf{e}_{att} + K_{D,att}\dot{\mathbf{e}}_{att} \tag{3.37}$$

where $K_{P,att}$, $K_{I,att}$, and $K_{D,att}$ are 3x3 diagonal, positive semi-definite gain matrices. The angle commands are then used with the motor throttle input (h_{cmd}) to calculate motor commands

$$\begin{bmatrix} m_1 \\ m_2 \\ m_3 \\ m_4 \end{bmatrix} = \begin{bmatrix} 1 & 0 & -1 & -1 \\ 1 & -1 & 0 & 1 \\ 1 & 0 & 1 & -1 \\ 1 & 1 & 0 & 1 \end{bmatrix} \begin{bmatrix} h_{cmd} \\ \phi_{cmd} \\ \theta_{cmd} \\ \psi_{cmd} \end{bmatrix}. \tag{3.38}$$

In simulation, the motor commands are then converted to motor thrusts (F_1, F_2, F_3, F_4) in Newtons using an experimentally-determined motor constant (k_{motor}) and then saturated to within the actuator limits

$$\mathbf{F_k} = \mathbf{k_{motor}m_k}. \tag{3.39}$$

The thrust forces are then fed into the system dynamics as the outputs of this control loop.

3.5 Summary

This section motivated and presented a new position control algorithm for a tethered multirotor aircraft. This position controller operates in spherical coordinates, and consists of three major components. These components are the reference command generation, a feedforward controller for the tether dynamics, and a PID/PD position controller. The implementation of this spherical position controller is discussed in Chapter 4. Chapters 5 and 6 present simulated and indoor flight testing results, respectively, for this position control algorithm.

This page intentionally left blank

Chapter 4

Hardware and Software Implementation

Various hardware and software implementation methods were used for testing the spherical position controller. This overview will begin with how the tether dynamics were numerically solved, followed by the flight simulation software, and the hardware and software used for indoor flight testing.

4.1 Tether Dynamics Implementation

The tether dynamics presented in Chapter 2 form a pair of transcendental functions. The shape of the tether is governed by two shape parameters, a and b, while the aircrafts location is described by the distance from the origin R, and angle θ. Similar to the derivation, this method for solving these equations will occur in 2 dimensions (θ, R), and the solution will be rotated about the inertial axis $\mathbf{I_z}$ using ϕ to form the full 3 dimensional solution. The tether length L is also used in these equations, and will be treated as a known constant during operation. Thus, two additional parameters or variables must be known in order to solve the tether dynamics.

During operation, these equations will be used for two primary functions within the controller structure, which will dictate which parameters and variables are known. The first function is the reference command generation, where the reference command

Table 4.1: Tether Dynamics Solution Scenarios

Scenario 1	Reference Generation	Scenario 2	Feed Forward
Known	Solving for	Known	Solving for
θ	R	θ	a
b	a	R	b
L		L	

R_{ref} is calculated to minimize the force of tension in the spherical position controller. In this case, the two known values are θ and b, where θ is a user defined parameter, and b is known because the minimum tension condition is $b = -X_c = 0$. As a result, the equations can be solved numerically for the parameter a and desired radius R. The second function is the tether dynamics feed forward model, which is used to determine the forces exerted on the aircraft by the tether, and is used to calculate the feed forward term for the spherical position controller. In this case, the aircraft state θ and R is known, however the tether shape parameters a and b are unknown. Thus the aircrafts state is used to solve for the tether shape parameters, which are used to determine the forces that the tether is exerting on the aircraft at a given state location. The algorithms for the reference command generation and tether feed forward model are presented in Chapter 3 as Algorithm 1 and Algorithm 2 respectively. A summary of the unknowns in each algorithm is in Table 4.1. The method for numerically solving these equations is presented in Section 4.1.1.

4.1.1 Numerical Methods

In both the discussed scenarios for solving the tether dynamics, there are two equations and two unknown values. As the two tether dynamics equations are transcendental functions they cannot be solved analytically, and must be solved numerically. The method chosen for numerically solving these two systems of two equations is the Newton Raphson method. This method is an iterative method for finding the roots of a function, or in this case, multiple functions by approximating the functions using a tangent line.

The necessary components to run the Newton Raphson method are the two cost functions for solving represented a F_1 and F_2 (presented for each scenario in Chapter 3), and the Jacobian of the two functions with respect to the two parameters that are being solved for, x_1 and x_2 (presented in Table 4.1).

$$\mathbf{J} = \begin{bmatrix} \frac{\partial F_1}{\partial x_1} & \frac{\partial F_1}{\partial x_2} \\ \frac{\partial F_2}{\partial x_1} & \frac{\partial F_2}{\partial x_2} \end{bmatrix} \tag{4.1}$$

The basic algorithm for the Newton-Raphson methods is as follow:

$$\mathbf{X}_{\mathrm{k}+1} = \mathbf{X}_{\mathrm{k}} - \mathbf{J}^{-1} \begin{bmatrix} F_1(\mathbf{X}_{\mathrm{k}}) \\ F_2(\mathbf{X}_{\mathrm{k}}) \end{bmatrix} \tag{4.2}$$

$$\text{Error} = \sqrt{F_1(X_{\mathrm{k}})^2 + F_2(X_{\mathrm{k}})^2} \tag{4.3}$$

This algorithm will continue until the Error is below a error threshold. For the purpose of simulation and indoor flight testing this parameter e_{thres} was set to 0.001, however this parameter could be set to a smaller value depending on the time available for additional iterations to refine the solution.

4.2 Simulation

In order to simulate a multirotor flying on the end of a tether, the full system was implemented into a MATLAB (Natick, MA) Simulink model [5]. Simulink allows a graphical system model to be created, allowing easy modification or parameter adjustment during testing. To simulate the multirotor aircraft, a 6DOF equations of motion block with quaternion representations was used. This block allowed the specification of the UAV's mass, inertial properties, initial conditions, and forces and moments acting upon the body. To simulate the tether system, a user-defined function calculated the inertial-frame forces that a tether would exert on the aircraft based on its current state. The dynamics for the tether are an exact implementation of the feed forward controller, acting in the negative direction.

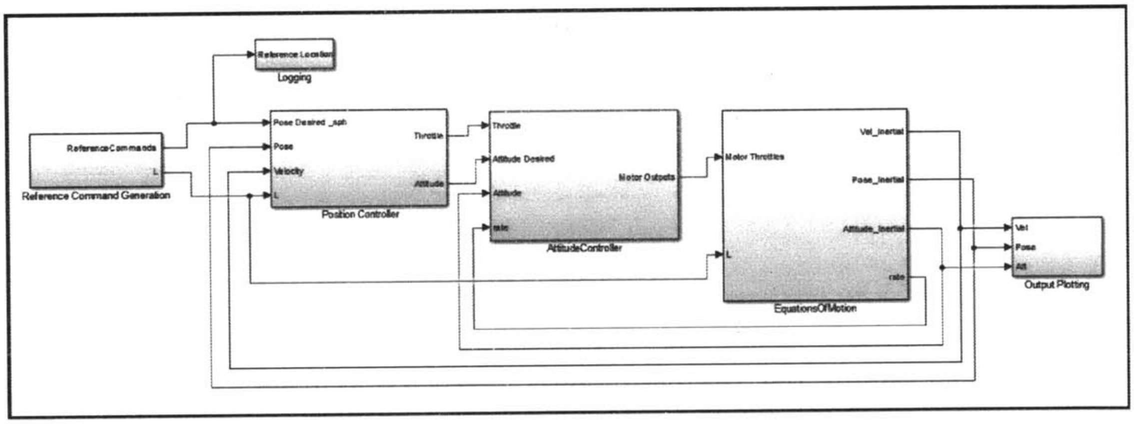

Figure 4-1: MATLAB Simulink Model for Flight Simulation

Table 4.2: Simulated Vehicle Physical Parameters

Param	Description	Value	Units
m	Total mass of the vehicle w/ battery	3.0	kg
I_{xy}	Moment of inertia about $\hat{\mathbf{b}}_\mathbf{x}$ and $\hat{\mathbf{b}}_\mathbf{y}$	0.009	kg m^2
I_z	Moment of inertia about $\hat{\mathbf{b}}_\mathbf{z}$	0.01	kg m^2
d	Distance from rotor plane to CoM in $\hat{\mathbf{b}}_\mathbf{z}$ direction	0.2	m

Table 4.3: Simulated Tether Properties

Param	Description	Value	Units
m	Total mass of the tether	0.015	kg
l	Length of the tether	15.0	m
λ_m	Linear density	0.001	$\frac{kg}{m}$

4.2.1 Simulated Vehicle Properties

For these simulated flight tests, the multirotor physical parameters were chosen to mimic a typical multirotor that is used for outdoor flight. These physical parameters are summarized in Table 4.2.

4.2.2 Tether Properties

The physical properties for the simulated tether were chosen to emulate a real-world outdoor flight scenario and are summarized in Table 4.3.

4.3 Indoor Flight System

4.3.1 RAVEN Flight Space

The indoor flight tests were performed at the RAVEN Indoor Flight Space in the Aerospace Controls Labratory at MIT [4]. This is a 5 x 10 x 3 meter indoor flight facility.

4.3.1.1 Motion Capture System

The Aerospace Controls Laboratory RAVEN Indoor Flight Space utilizes an array of Vicon motion capture cameras [11]. This system uses an array of 22 infrared cameras that track an array of small reflective dots that are rigidly attached to the aircraft, as seen in Figure 4-2. As a result, the system allows full state feedback for vehicle control during operation. It provides a realtime stream of position, velocity, orientation, and rate of the flight vehicle at 100 Hz. These cameras are placed in strategic locations around the edge of the room to allow full coverage of the flight space.

4.3.2 Flight Hardware

The multirotor used for indoor flight testing was a QAV250 model. This vehicle was outfitted with a custom autopilot that interfaced with the Vicon system, a small lithium polymer battery, and four motors. These vehicles are commonly used in the Aerospace Controls Lab, as they are a small quadrotor frames that are extremely durable. Table 4.4 outlines the components and configuration used for indoor flight testing.

Figure 4-3 is a picture of the QAV250 multirotor that was used for indoor flight testing. The battery was mounted below the vehicle, and the tether was mounted to the front of the vehicle, as close to the center of mass as possible.

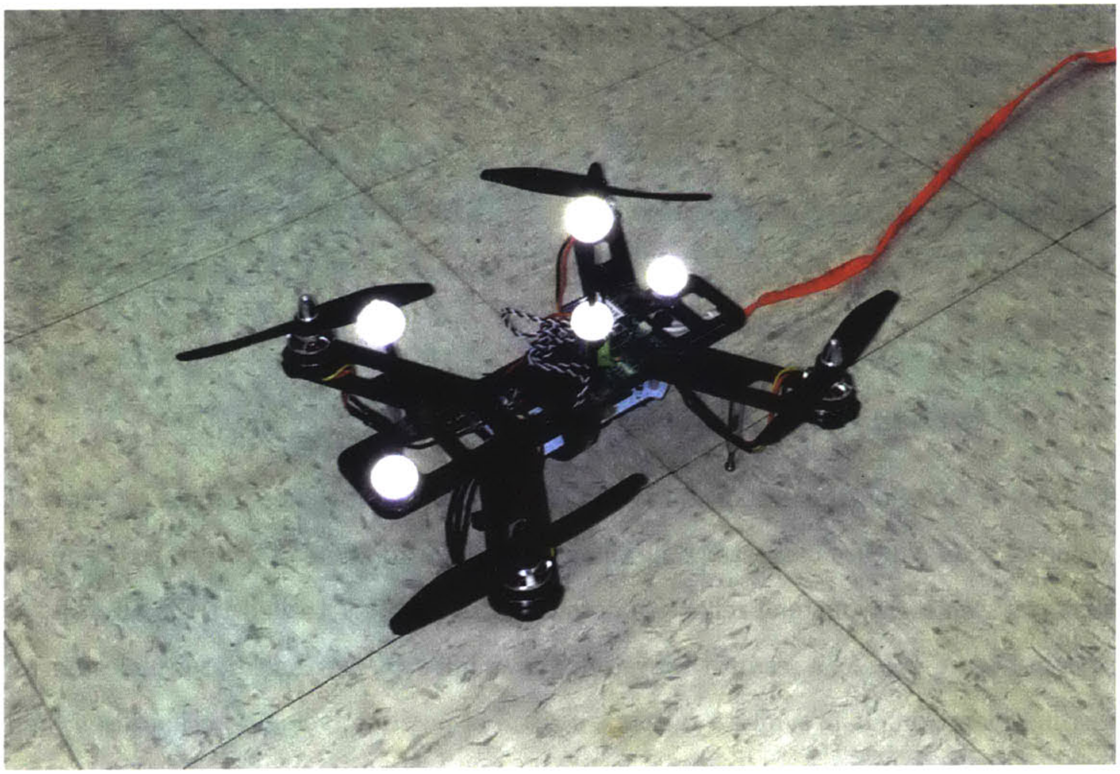

Figure 4-2: Example array of Vicon dots rigidly attached to a QAV250

4.3.3 Indoor Tether Parameters

Table 4.6 summarizes the fixed-length tether used for indoor flight testing. A tether length of $3m$ was chosen to be as long as possible without putting the aircraft at risk of striking a wall or the ceiling of the indoor RAVEN flight space.

4.3.4 Flight Software

The software used for the indoor flight testing is a feedback controller that utilizes two successive levels of loop closure. The control structure is identical to the that described in Chapter 3 of this thesis. The inner loop, called the attitude loop, runs on board the aircrafts autopilot. The outer loop controller, or the position loop, runs on a stationary computer, which supplies the inner attitude loop with reference commands. The reference inputs to the position controller can be set directly using a XBox 360 wireless controller, or from a trajectory planner. For the purposes of the

Table 4.4: QAV250 Components for Indoor Flight Testing

Component	Description
Frame	QAV250 Kit
Autopilot	Custom Aerospace Controls Lab "UberPilot"
Motors	(4) RCMC Micro Muscle Motors 1806
ESC	(4) RCMC 15 Amp Eleectronic Speed Controllers
Propellers	(4) HQProps 5x4 Carbon/Nylon
Battery	Thunder Power 3s 1350mAh Lithium Polymer

Table 4.5: QAV250 Physical Parameters

Param	Description	Value	Units
m	Total mass of the vehicle w/ battery	0.402	kg
I_{xy}	Moment of inertia about $\hat{\mathbf{b}}_\mathbf{x}$ and $\hat{\mathbf{b}}_\mathbf{y}$	0.00417	kg m^2
I_z	Moment of inertia about $\hat{\mathbf{b}}_\mathbf{z}$	0.00819	kg m^2
L	Arm length	0.085	m
d	Distance from rotor plane to CoM in $\hat{\mathbf{b}}_\mathbf{z}$ direction	0.0125	m

indoor flight tests for this project, the reference inputs were supplied by a trajectory planner with a preprogrammed flight path, which will be described in Chapter 6. This section will outline the implementation of the various control loops used for indoor flight testing.

4.3.4.1 Position Control Loop

The outer loop position controller operates on a separate off-board computer that serves as an operator console. The primary function of the position controller is to send reference attitude commands to the aircrafts inner control loop. The position control loop has access to the vehicles full state, as measured by the Vicon system. The flight software runs using the open source platform Robot Operating Software, or ROS [12]. This is a robust, extendable package that allows control "Nodes" to communicate with one another, which makes it very well suited for a complex flight control system with many discrete features, such as that implemented in the Aerospace Controls Laboratory. The wireless communication between the outer loop and inner loop control systems utilized an XBee 2.4 GHz serial radio system. The main operator

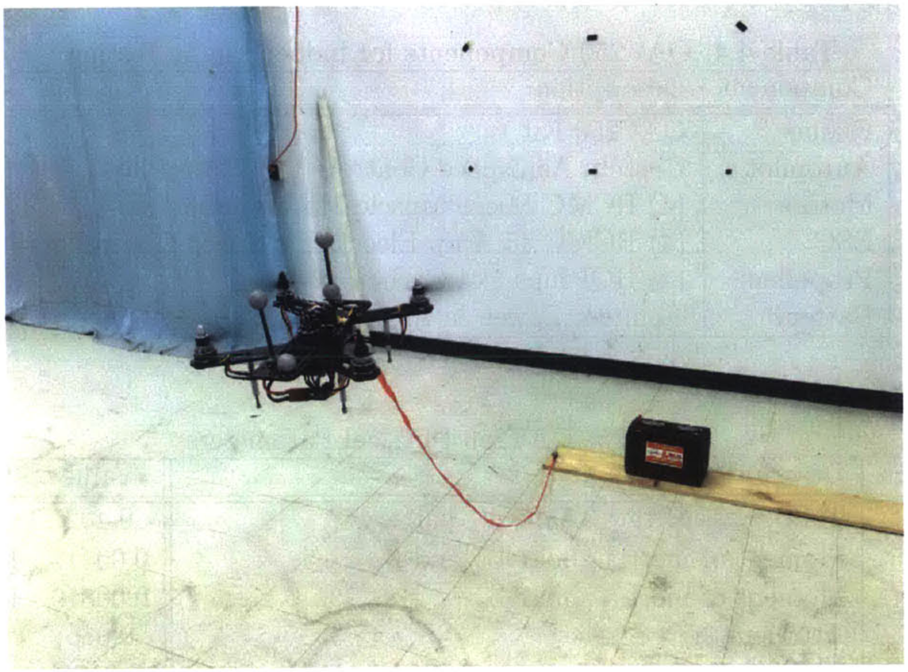

Figure 4-3: Picture of a QAV250 flying on a tether in the Aerospace Controls Lab

Table 4.6: Tether Physical Properties

Param	Description	Value	Units
m	Total mass of the tether	0.041	kg
l	Length of the tether	3.0	m
λ_m	Linear density	0.0133	$\frac{kg}{m}$
	Material	Silicon Wire	

interface with the position control system is a Microsoft XBox 360 wireless controller, which allows safe remote operation of the aircraft, utilizing the various buttons to issue commands (such as takeoff or land) or position reference locations using the joysticks.

As outlined in Section 6.2, the indoor flying involved the testing two different position controllers–a traditional Cartesian PID position controller, and the proposed spherical position controller. These two position controllers were both implemented in Python, and run separately using the existing ROS infrastructure depending on which controller was being tested. These position controllers were both fundamentally position feedback controllers, operating in the same framework, and thus used identical PID controller gains with the exception of $K_{\mathrm{I,R}} = 0$. These gains were tuned manually such that the vehicle displayed smooth and stable flight characteristics, with no steady state error.

4.3.4.2 Attitude Control Loop

The inner attitude control loop operates onboard the aircraft, utilizing the autopilots estimate of the vehicles attitude to track a desired attitude command. The primary function of the attitude loop is to output motor throttle commands, which generate forces and moments on the aircrafts body. For the purpose of these indoor flight testing, the inner attitude control loop was unmodified from the standard configuration used in the laboratory. The attitude controller is a PD controller, and the gains were previously tuned to yield good tracking performance.

The inner control loop is implemented onboard the custom autopilot used in the Aerospace Controls Laboratory. This autopilot, named the UberPilot, was developed and manufactured by Mark Cutler at the Aerospace Controls Laboratory [3].

4.3.4.3 Data Logging

During operation, the flight software logs data at 100 Hz. This data logging system records key state information, including position, velocity, control inputs, and vehicle health information. Upon the completion of a flight, the software automatically saves the flight data to a .CSV log file. This file can be imported using MATLAB or a similar program for post processing, analysis, and plotting.

4.4 Summary

This section presented the implementation methods used for simulated and experimental flight testing of the spherical position controller. For simulated flight testing, the multirotor and tether dynamics were implemented into a MATLAB Simulink model. For indoor flight testing, the spherical position control algorithm was implemented into the indoor RAVEN flight space in the Aerospace Controls Laboratory at

MIT, allowing the proposed controller to be tested using real hardware. Chapters 5 and 6 present verification and validation testing design and results of the proposed position controller for simulated and indoor flight testing, respectively.

Chapter 5

Simulation

5.1 Testing Motivation

Simulated flight provides an environment to test the proposed flight control algorithms and tether models without risking hardware safety during initial development. The primary motivation was to provide verification and validation for the proposed control system.

The first step was to verify that the proposed spherical position controller was able to stabilize the multirotor, eliminate state error, and effectively control the tether dynamics. In order to test this, the control system was tested in a variety of configurations, beginning with a traditional Cartesian position controller, with the goal of establishing a concrete understanding of controller input directions, gain settings, and baseline performance. The transition from the Cartesian position controller to the spherical position controller was taken in a series of steps in order to understand how each component of the proposed controller effected the multirotors control system. Each component of the proposed controller was designed to mitigate a specific problem with the baseline Cartesian system, and thus the verifcation steps were chosen to confirm each problem was resolved, as well as observe any additional problems arose during implementation.

The second purpose for simulated flight testing was to provide validation of the controller in preparation for indoor flight testing. This translated to testing the

Table 5.1: Simulated Cartesian Position Controller Test Flight

Test Name	Initial Location	Reference Location	Convention and Units
Cartesian Baseline	$(0, 80, 14.5)$	$(45, 60, 15)$	$(\phi \text{ deg}, \theta \text{ deg}, R \text{ m})$

controllers response to real world flying conditions, tether or aircraft modeling errors, and observing how the controller reacted. As the tether feed forward model was subject to error due to environmental changes or changes in the tether weight, it was important to understand and observe the controllers response to these external disturbances.

5.2 Experimental Design

5.2.1 Controller Verification

The first stage to simulated flight testing was verifying that the proposed spherical position controller resolved the problems associated with the baseline Cartesian position control system. In order to understand each component of the proposed system, the position controller was flown in a variety of piecewise configurations in order to show that the proposed position controller solves all the problems associated with the baseline position controller.

5.2.1.1 Baseline Cartesian Position Controller

The first simulated flight used a traditional Cartesian position controller to stabilize the aircrafts position on the tether. The goal of this flight was to generate a baseline performance and observe the problems that motivated the development of the spherical controller. For this test flight, the aircraft was given a step input reference location at $t = 0$.

There are two apparent problems with the Cartesian position control system. The first is that the control error integrators are compensating for the un-modeled tether dynamics, winding up in the $\hat{R}$ direction, and creating additional unnecessary tension in the tether. The second problem is a lack of control over tether tension, creating a situation where the tether tension is higher than necessary and increasing due to the $\hat{R}$ integration. These two problems were expected to be prevalent in this flight test.

5.2.1.2 Spherical PID/PD Position Controller

The first component of the proposed position controller that was implemented was the spherical PID/PD control system. This component was designed to eliminate the error integration in the $\hat{R}$ direction by shifting the coordinate system such that two integrators, I_ϕ and I_θ, are operating in directions that are unconstrained by the tether.

The second simulated flight used the spherical position controller without feed forward control or any tether model. This simulated flight was conducted to show that the error integration control terms were no longer growing over time, while still eliminating steady state error. The flight plan was summarized below, where the aircraft was given a step input reference location at $t = 0$.

Table 5.2: Simulated Spherical Position Controller With Error Integration Test Flight

Test Name	Initial Location	Reference Location	Convention and Units
Spherical Baseline	$(0, 80, 14.5)$	$(45, 60, 15)$	(ϕ deg, θ deg, R m)

Even with the controller moved into spherical coordinates, a fundamental problem still existed, such that the position controller was still relying on the error integrators to compensate for the tether dynamics. In order to solve this, a tether dynamics feed forward model was implemented into the simulation.

5.2.1.3 Spherical PID/PD Position Controller with Feed Forward Control

The third simulated flight test was designed to show that the feed forward (FF) model will compensate for the tether dynamics, reducing the position controllers reliance on the error integrators and refocusing that control component to eliminating steady state error due to disturbances or modeling errors. The flight plan is summarized below, where the aircraft was given a step input reference location at $t = 0$.

Table 5.3: Simulated Spherical Position Controller With Feed Forward Test Flight

Test Name	Initial Location	Reference Location	Convention and Units
Spherical FF	$(0, 80, 14.5)$	$(45, 60, 15)$	$(\phi$ deg, θ deg, R m$)$

5.2.1.4 Spherical PID/PD Position Controller with Feed Forward Control and Reference Command Generation

The one outstanding problem with the Cartesian position controller and the previous tested configurations was that the controller did not have control over the shape of the tether, and the reference command for R was such that $R = L$. This creates a situation where the aircraft is always attempting to fly to a reference location that it cannot reach due to the tether dynamics, and as a result the aircraft is always exerting more forces on the tether than needed to keep the tether off the ground, as specified by the minimum tension conditions.

To mitigate this problem, the reference command generation algorithm, as described in Chapter 3, was used. The multirotors reference command along $\hat{R}$ was not set directly by the operator, rather the tether length L was set, and the position controller determined a desired R_{ref} such that the tether tension was minimized. The operator sets the unconstrained position reference commands ϕ_{ref} and ϕ_{ref}, which effectively defines the $\hat{R_{\text{ref}}}$ direction, while the tether length L and physical properties determine a reference location along this vector that minimizes tension, subject to spacial constraints.

For the last simulated verification flight test, the reference command generation (RCG) algorithm was implemented into the system. This test was conducted to show reduced tension, and the controller effectively tracking the $\hat{R_{\text{ref}}}$. The flight plan is summarized below, where the aircraft was given a step input reference location at $t = 0$.

Table 5.4: Simulated Spherical Position Controller With Feed Forward and Reference Command Generation Test Flight

Test Name	Initial Location	Reference Location	Convention and Units
Spherical FF and RCG	$(0, 80, 15)$	$(45, 60, 15)$	$(\phi \text{ deg}, \theta \text{ deg}, L \text{ m})$

5.2.2 Controller Validation

While Section 5.2.1 discussed the tests designed to verify the controller architecture and operation, the second stage of simulated flight testing was controller validation, such that the controller will operate in a real world scenario. Practically, this translated to designing simulated tests that changed the dynamics of the tether system such that they deviate from the models, and evaluate how the position controller compensates for the new errors.

For these tests, the proposed spherical position controller was implemented as tested in the final verification test. During all of the validation testing the controller and controller parameters were left constant, while the environment parameters were modified to reflect different real-world scenarios where the simulated dynamics deviate from the controller models. The deviation in the models was designed to mimic the effect of wind on the tether, incorrect tether linear density, and incorrect tether length.

These tests evaluated the controllers response to disturbances using a reference location step input at $t = 0$, which then remained constant for $t > 0$. This structure allowed the analysis of controllers dynamic response to an input, as well as the steady state error, tether tension, and stability in the presence of disturbances.

5.2.2.1 Wind Force on Aircraft and Tether

The first simulated validation test was designed to evaluate the controllers response to a steady wind acting on the aircraft in the inertial $+\hat{X}$ direction. The wind generated a separate drag force on the aircraft and tether system, as described by

$$F_{\text{drag}} = -\frac{1}{2}\rho A v^2 C_d \tag{5.1}$$

where the parameters are defined in the following table. These values were chosen for a typical multirotor aircraft and tether system. This wind drag force was implemented into the vehicle and tether dynamics simulation, both acting in the X direction.

Table 5.5: Wind Drag Force Parameters

Parameter	Description	Aircraft	Tether	Units
ρ	Air Density	1.225	1.225	$\frac{kg}{m^3}$
A	Cross Sectional Area	0.05	0.015	m^2
v	Wind Velocity	5.0	5.0	$\frac{m}{s}$
C_d	Coefficient of Drag	0.8	0.47	None

The simulated flight plan is summarized below, where the aircraft was given a step input reference location at $t = 0$.

Table 5.6: Simulated Wind with Spherical Position Controller

Test Name	Initial Location	Reference Location	Convention and Units
Wind Validation	$(0, 80, 14.5)$	$(45, 60, 15)$	$(\phi \text{ deg}, \theta \text{ deg}, L \text{ m})$

5.2.2.2 Incorrect Tether Linear Density

The next test was to evaluate the controllers ability to compensate for an incorrect tether linear density, resulting in the mass of the tether being incorrectly estimated. The mass of the tether is defined as

$$m_{tether} = \lambda_m * L \tag{5.2}$$

and is a key term in determining the force of tension on the multirotor. The parameter λ_m could be wrong due to material variability, or it may change during the flight if it gets wet. For the purpose of this test, the true linear density of the simulated tether was increased by %25, with $\lambda_m = 0.0125\frac{kg}{m}$. The simulated flight test plan is summarized below, where the aircraft was given a step input reference location at $t = 0$.

Table 5.7: Simulated %25 Increase in λ_m with Spherical Position Controller

Test Name	Initial Location	Reference Location	Convention and Units
λ_m Validation	$(0, 80, 14.5)$	$(45, 60, 15)$	(ϕ deg, θ deg, L m)

5.2.2.3 Incorrect Tether Length

The next validation test performed in the simulated environment was to evaluate the controllers ability to compensate for an incorrect tether length. This scenario could arise if the tether length is incorrectly estimated, and will ultimately have a two-fold effect on the tether dynamics and controller. The first effect is that the tether will be shorter than the controller is compensating for, causing the controller to attempt to fly to a location it cannot reach. The second effect is that the mass of the tether will be lighter than the model estimates, as there is less tether for the aircraft to lift. For this test, the simulated tether length L was reduced by 10%, resulting in an actual tether length of $13.5m$, while the controller is still operating with information that the tether length is $15m$. The simulated flight test plan is summarized below, where the aircraft was given a step input reference location at $t = 0$.

Table 5.8: Simulated 10% Decrease in L with Spherical Position Controller

Test Name	Initial Location	Reference Location	Convention and Units
λ_m Validation	$(0, 80, 11.5)$	$(45, 60, 15)$	(ϕ deg, θ deg, L m)

5.2.2.4 Increased Tether Length

The final validation test for the spherical position controller is to confirm that it will work with a variety of tether lengths, not just the single tether length of $L = 15m$ that has been used for simulated flight testing. For this test, the tether length was increased to $L = 25m$, while maintaining the same physical properties, such as linear density λ_m. This test is primarily to demonstrate that the gain settings for the system are independent of tether length. The simulated flight test plan is summarized below, where the aircraft was given a step input reference location at $t = 0$.

Table 5.9: Increase in Tether Length to $L = 25m$ with Spherical Position Controller

Test Name	Initial Location	Reference Location	Convention and Units
λ_m Validation	$(0, 80, 24)$	$(45, 60, 25)$	(ϕ deg, θ deg, L m)

5.3 Experimental Results

5.3.1 Verification Testing Results

This section will present and analyze the results of the simulated flight verification testing.

5.3.1.1 Baseline Cartesian Position Controller

For the baseline test of the traditional Cartesian position control system, the aircrafts trajectory and state information is presented in Figure 5-1. While this controller operates in Cartesian coordinates, the state information is presented in spherical coordinates to allow comparison with later tests. Figures 5-2 and 5-3 show the state error and control error integration transformed into spherical coordinates. Figure 5-4 shows the position controller output in the inertial reference frame. Figures 5-5 and 5-6 present the force exerted onto the aircraft by the tether tension in the inertial reference frame and the tether shape in two dimensions, viewed from the side.

The state error, presented in Figure 5-2, shows that the control integrators eliminate error in the unconstrained directions ϕ and θ, however it also shows there is always error in $\hat{R}$, which is integrated by $\mathbf{I_z}$ to yield a constantly increasing control effort to reduce this error. Fundamentally it is impossible to reduce this state error to zero, as $R = L$ would require $F_T = \infty$ due to the tether dynamics. The controllers error integrators are shown in Figure 5-3, which have been transformed into spherical coordinates. An important observation for validating the problems associated with using the Cartesian position control system on a tethered system as presented in Chapter 3 is that in approximate steady state operation, the controllers integrators are always increasing in $\hat{R}$. As the Cartesian controllers three axes (x, y, z) all have

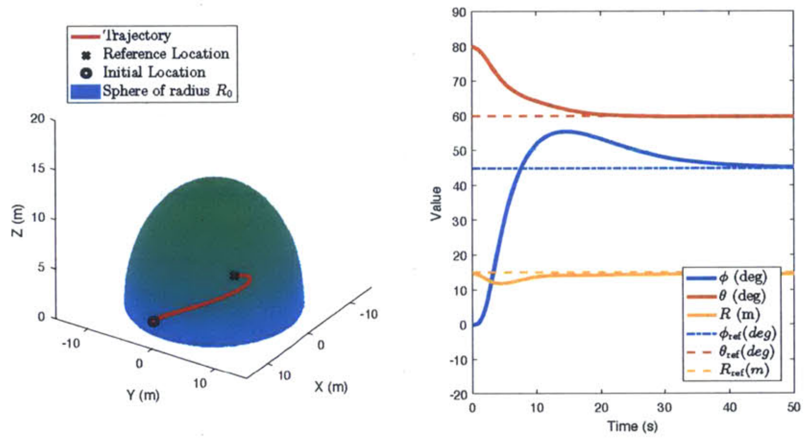

Figure 5-1: Baseline Cartesian Controller: Trajectory and State Information

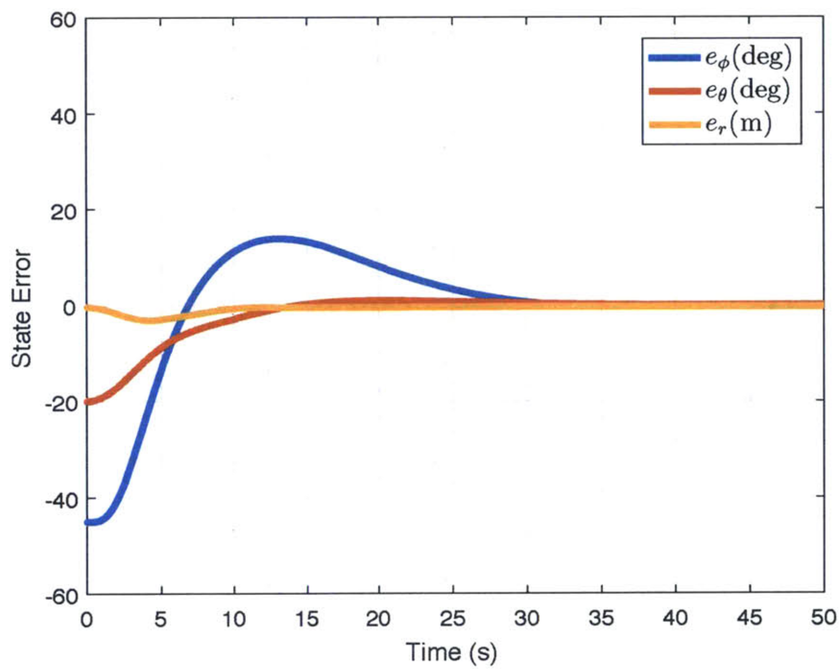

Figure 5-2: Baseline Cartesian Controller: State Error

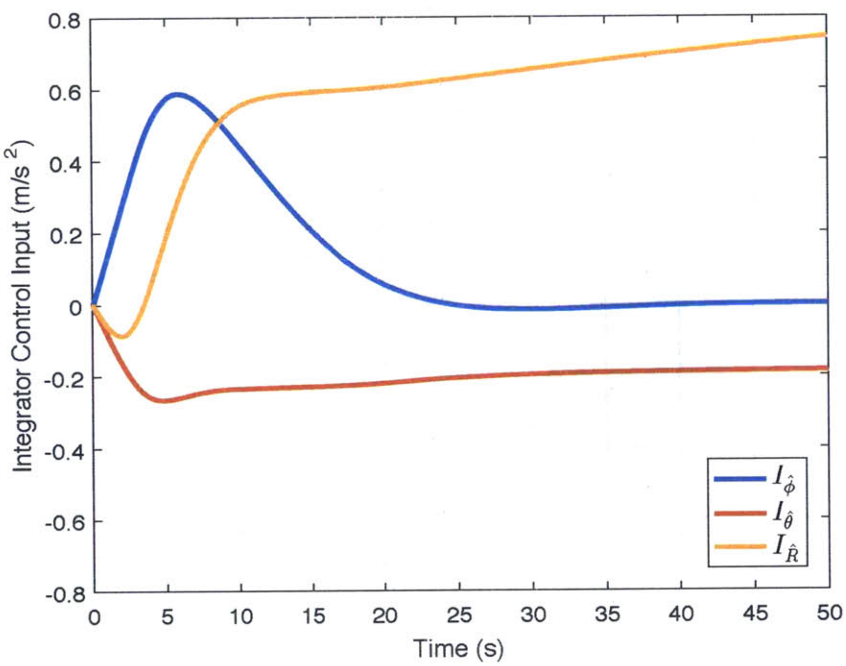

Figure 5-3: Baseline Cartesian Controller: PID Control Integrators

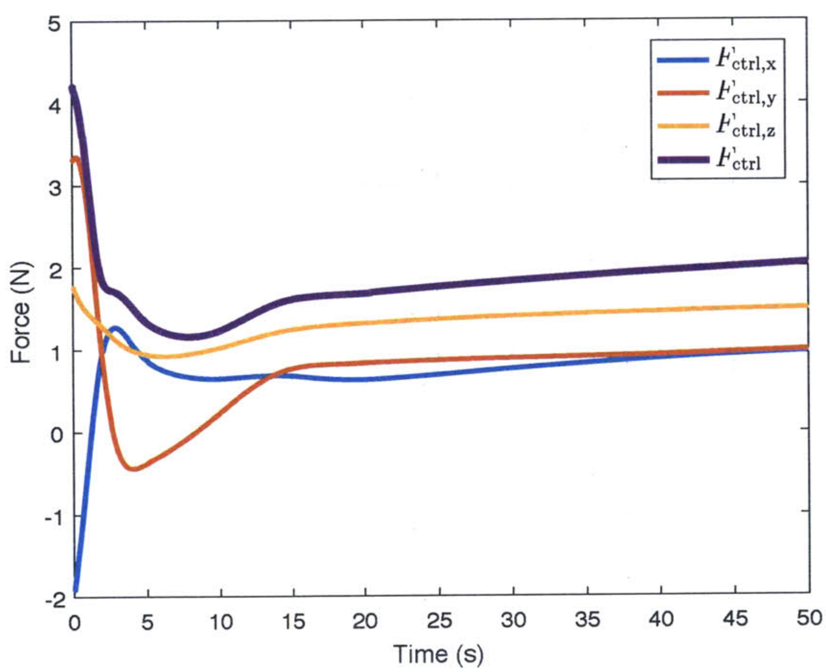

Figure 5-4: Baseline Cartesian Controller: Position Controller Force Output

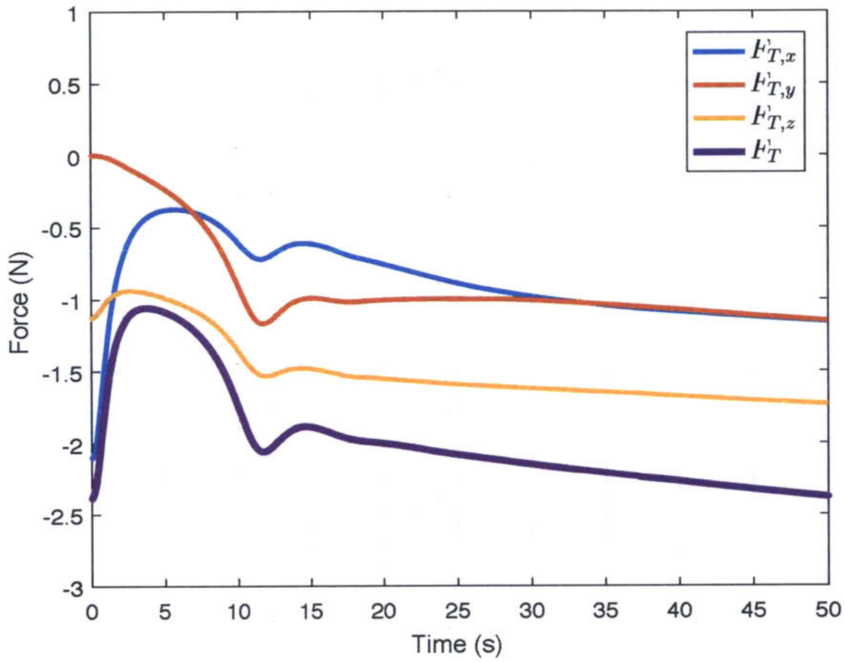

Figure 5-5: Baseline Cartesian Controller: Tether Tension on Aircraft

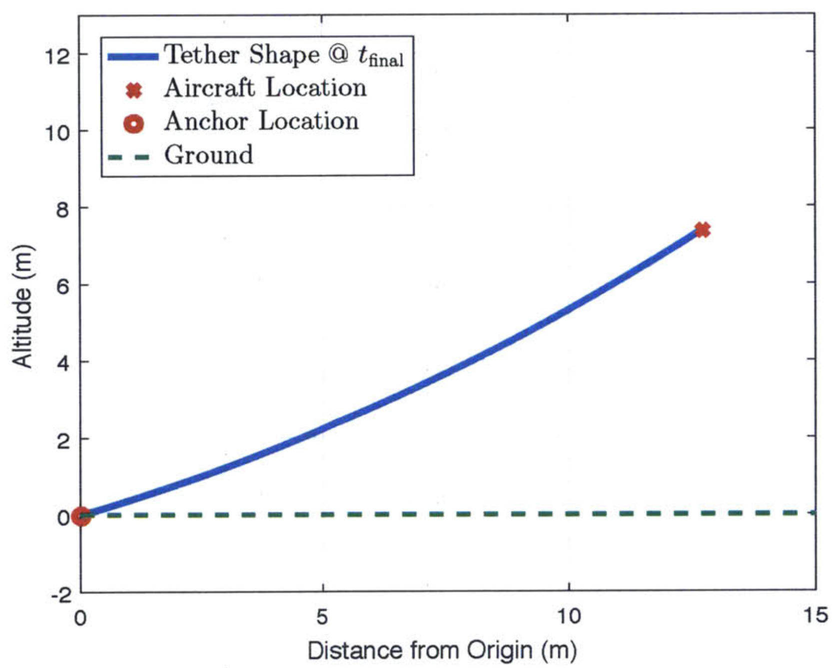

Figure 5-6: Baseline Cartesian Controller: Tether Shape

components in $\hat{R}$, all three integrators are integrating the error in R.

Often referred to as integrator windup, this increasing control effort creates excessive tension on the tether. If left uncorrected or unbounded, this increasing force on the tether can lead to aircraft destabilization if the control inputs saturate, such that the motors reach their thrust capacity. The tether tension is presented below in Figure 5-5, which can be see to be increasing over the steady state region from $t = 15 : 50$ and reaching a nominal value of $F_{\mathrm{T}} = 2.41N$ at the conclusion of the simulation. Figure 5-6 shows the tether shape at the conclusion of the test. As seen in the figure, the tether leaves the origin, the tether attachment point, with a positive angle of departure, suggesting that the tether parameter X_c is negative. This supports the claim that the Cartesian controller operates such that the tether is under more tension than necessary to keep it off the ground, or $y_{\mathrm{teth}}(x) > 0$.

This baseline evaluation test verifies the existence of problems presented in Chapter 3 associated with the traditional Cartesian PID position controller (as presented in Appendix A) while operating on the end of a tether.

5.3.1.2 Spherical PID/PD Position Controller

The aircrafts trajectory and state information for the implementation of the spherical PID/PD position controller is presented in Figure 5-7. Figures 5-8 and 5-9 show the state error and control error integration in spherical coordinates. Figure B-1 shows the position controller output in the inertial reference frame. Figures 5-10 and 5-11 present the force exerted onto the aircraft by the tether tension in the inertial reference frame and the tether shape in two dimensions, viewed from the side.

The state error shown in Figure 5-8 shows that this basic PID/PD controller eliminates error in the unconstrained $\hat{\phi}$ and $\hat{\theta}$, however there is a constant error in $\hat{R}$, similar to the performance of the Cartesian position control system. This test represented the shift from a Cartesian coordinate system to a spherical coordinate system, with the primary motivation being the elimination of integration in the direction of the tether, $\hat{R}$. This intermediary test of the spherical position controller verifies the motivation for the coordinate shift, as this step eliminates the integration of error in

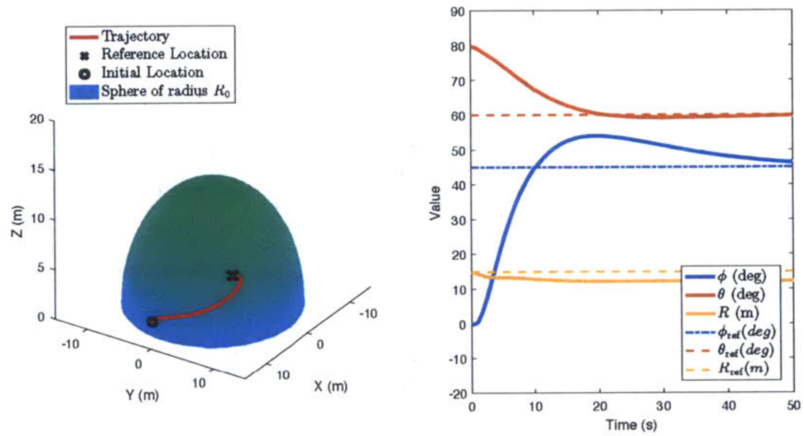

Figure 5-7: Spherical PID/PD Position Controller: Trajectory and State Information

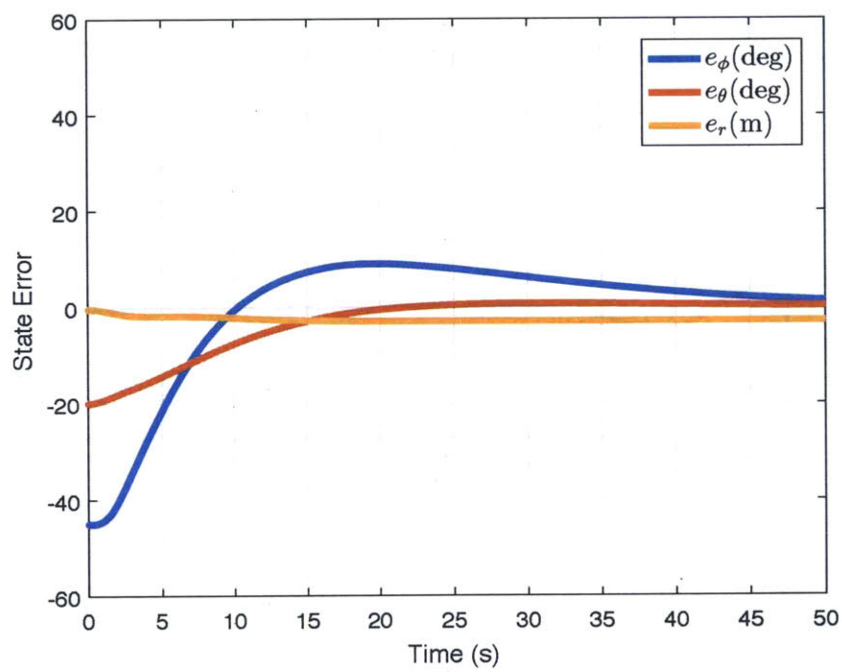

Figure 5-8: Spherical PID/PD Position Controller: State Error

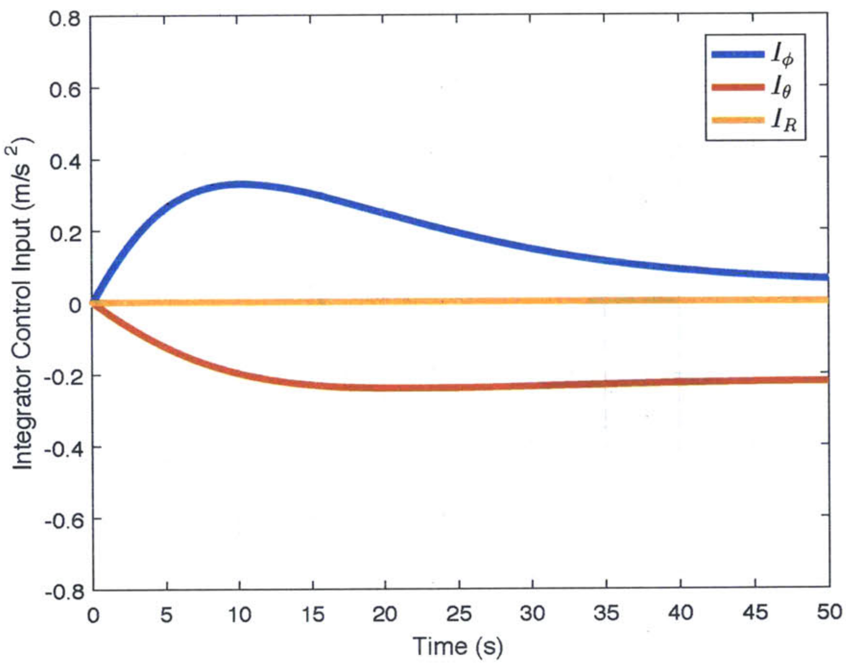

Figure 5-9: Spherical PID/PD Position Controller: PID Control Integrators

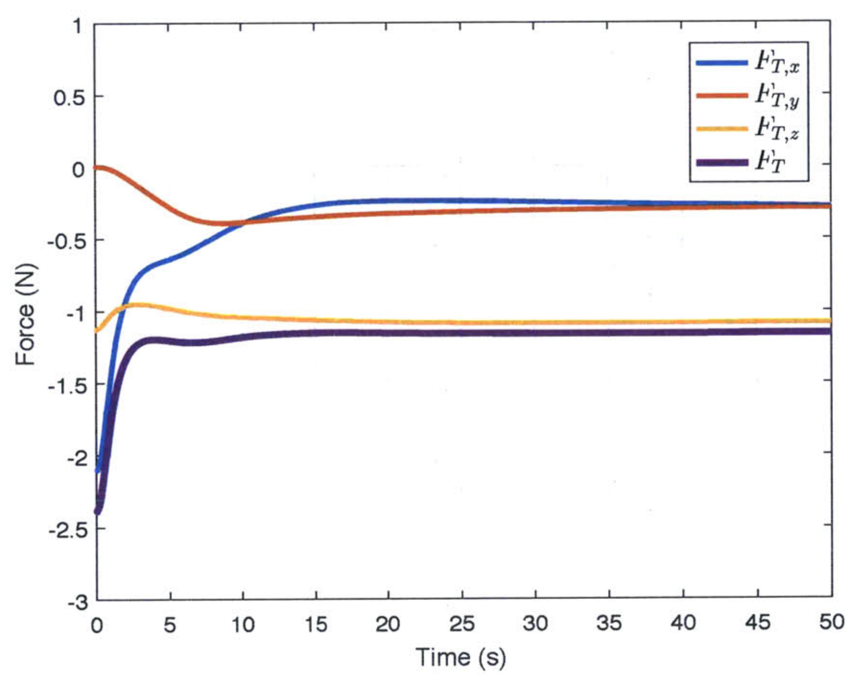

Figure 5-10: Spherical PID/PD Position Controller: Tether Tension

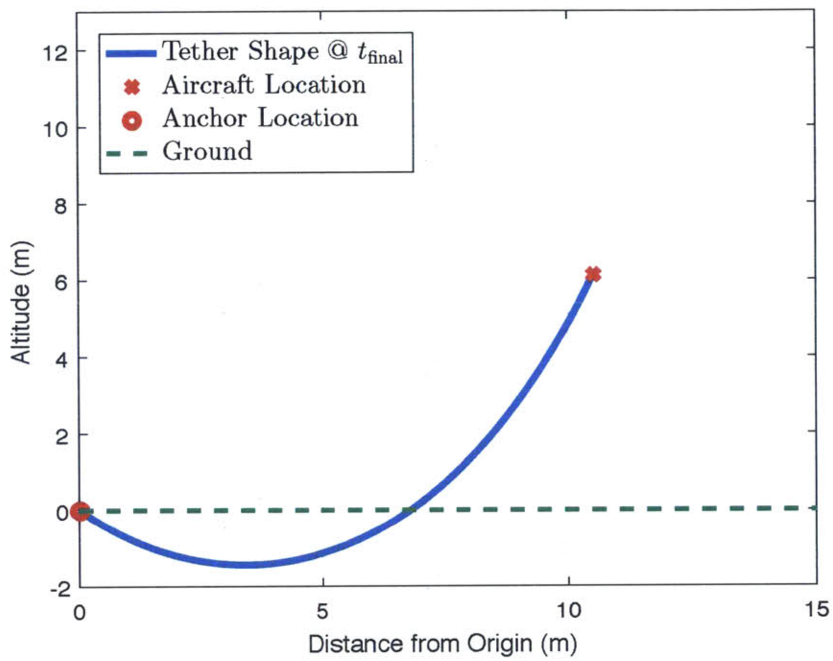

Figure 5-11: Spherical PID/PD Position Controller: Tether Shape

$\hat{R}$. Figure 5-8 shows the existence of error in $\hat{R}$, while Figure 5-9 shows there is no integration in $\hat{R}$. The integrators in $\hat{\phi}$ and $\hat{\theta}$ are non-zero, as they are correcting the multirotors positional error in the directions not constrained by the tether.

However two problems with the Cartesian system are still visible in this basic implementation of the spherical PID/PD controller. The integrators are still being used to compensate for the tether dynamics and external disturbances, and there is still no control over the tethers shape. There are no simulated external disturbances, thus the integrators being used to compensate for the tether dynamics is evidenced by the large non-zero integrator values in $\hat{\phi}$ and $\hat{\theta}$. While the nominal tension value $F_{\text{T}} = 1.16N$ is less the Cartesian case and constant in steady state, the tether is violating a desired operating condition that $y_{\text{tether}}(x) > 0$, as shown in Figure 5-11.

This initial test of the basic spherical position controller was successful in eliminating error integration in $\hat{R}$, however the controller still needs improvement to mitigate the problems associated with tether dynamics compensation and tether shape.

5.3.1.3 Spherical PID/PD Position Controller with Feed Forward Control

The aircrafts trajectory and state information for the implementation of the spherical PID/PD position controller with feed forward (FF) control of the tether dynamics is presented in Figure 5-12. Figures B-2 and 5-13 show the state error and control error integration in spherical coordinates. Figure B-3 shows the position controller output in the inertial reference frame. Figures 5-14 and 5-15 present the force exerted onto the aircraft by the tether tension in the inertial reference frame and the tether shape in two dimensions, viewed from the side.

This simulated flight shows a substantial improvement of the controllers ability to compensate for the tether dynamics. The controller no longer requires the control integrators to compensate for the tether dynamics, and achieves zero unconstrained ϕ and θ state error. The decrease in dependence on the control integrators is shown by the reduced total maximum value of total error integration, shown in Figure 5-13.

The controller now uses the feed forward model to apply tension to the tether, however there is still no control over the shape of the tether. The aircraft still has a constant state error in $\hat{R}$, which is driving the PD controller in $\hat{R}$ to apply additional unnecessary tension, similar to the Cartesian system. However the important difference is that this additional tension is constant, and not increasing with time. In this configuration, the aircraft is not at risk of destabilization due to actuator saturation, however it is operating at a reduced efficiency due to the increased force it is exerting on the tether.

5.3.1.4 Spherical PID/PD Position Controller with Feed Forward Control and Reference Command Generation

The aircrafts trajectory and state information for the implementation of the spherical PID/PD position controller with feed forward (FF) and reference command generation (RCG) is presented in Figure 5-16. Figures B-4 and B-5 show the state error and control error integration in spherical coordinates. Figure B-6 shows the position controller output in the inertial reference frame. Figures B-7 and 5-17 present the

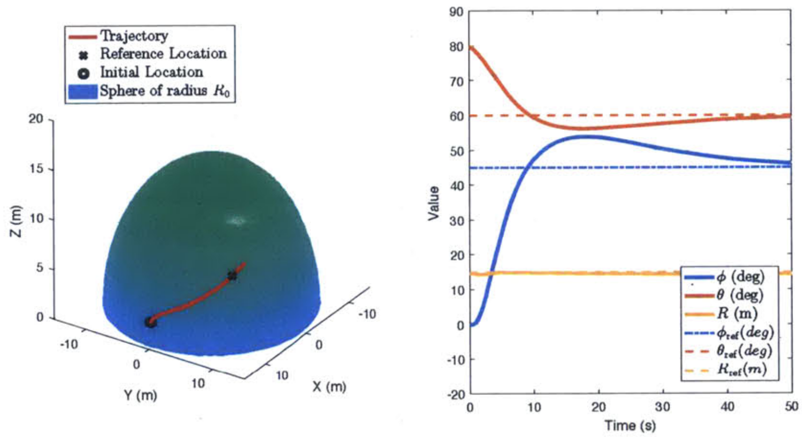

Figure 5-12: Spherical PID/PD Controller with FF: Trajectory and State Information

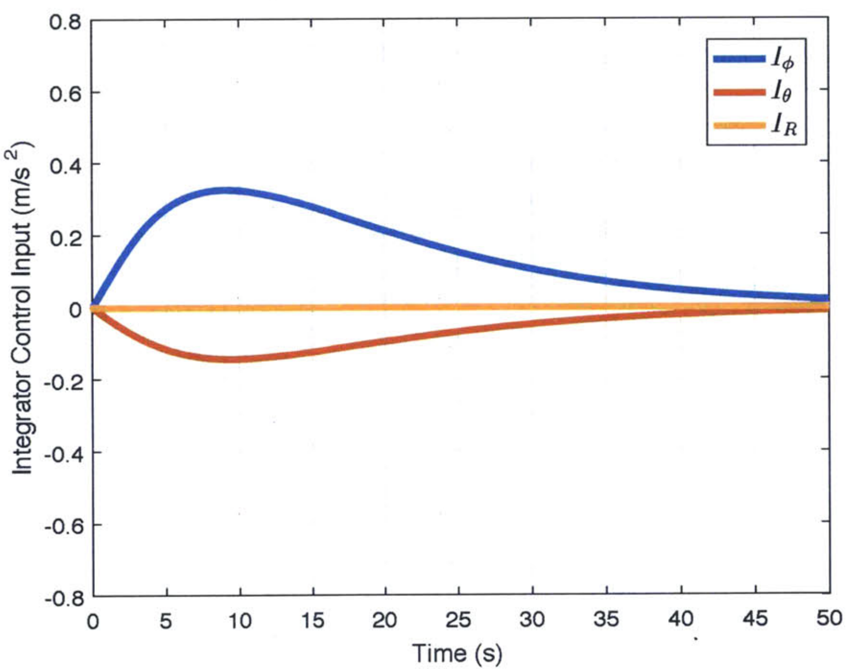

Figure 5-13: Spherical PID/PD Position Controller with FF: PID Control Integrators

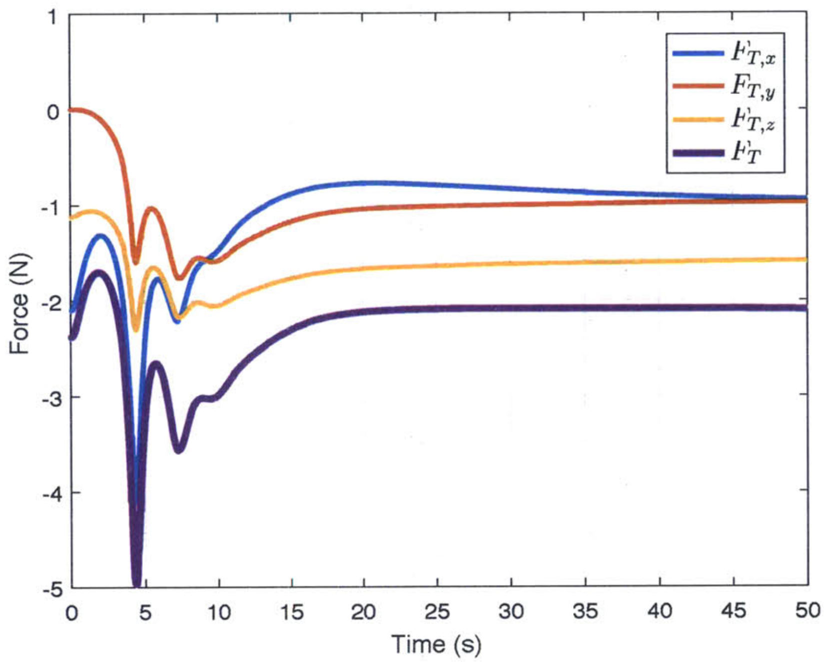

Figure 5-14: Spherical PID/PD Position Controller with FF: Tether Tension

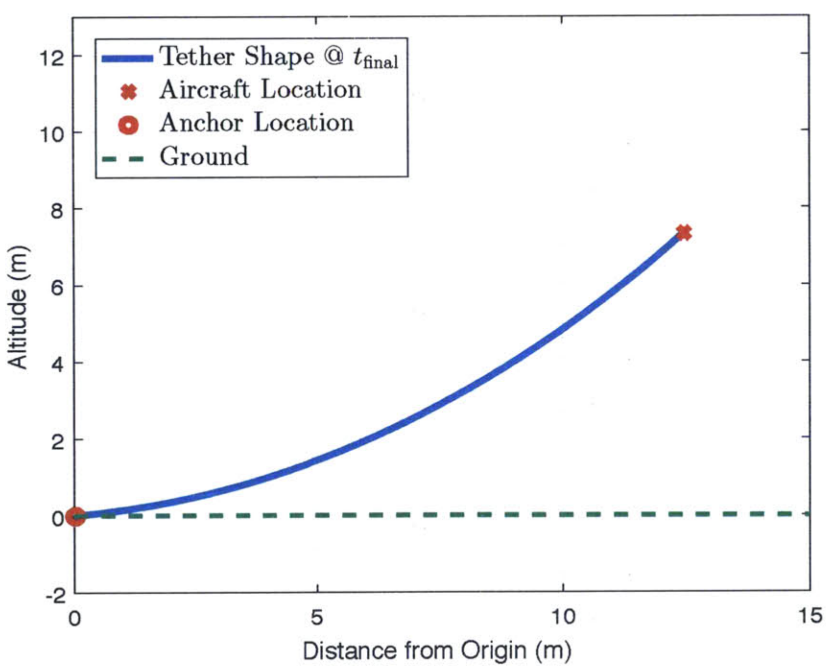

Figure 5-15: Spherical PID/PD Position Controller with FF: Tether Shape

force exerted onto the aircraft by the tether tension in the inertial reference frame and the tether shape in two dimensions, viewed from the side.

This simulated flight used the full implementation of the proposed spherical position controller. This simulation now uses the reference command generator (RCG) outlined in Chapter 3. This technique uses the tether length L, the desired $\hat{R}$, and minimal tension constraints to calculate the desired R_{ref} reference command value. For this specific flight with a tether length of L, the RCG output $R_{\text{ref}} = 14.48m$. As seen in Figure 5-17, the slope $\frac{d}{dx}y_{teth}(x) = 0$ for $x = 0$, indicating that the tension has met the minimum tension criteria and constraints established in Chapter 4.

After the controller transients settled, the tether tension for this simulated flight was $F_{\text{T}} = 1.53N$. This tension value is compared to the previous configurations below in Table 5.10 and Figure 5-18. It should be noted that for the $F_{\text{T,sph}}$ case, although the controller exerted the least tension on the tether, it violated the tether shape constraints.

Table 5.10: Final Tether Tension Comparison for Verification Tests

Test Name	|Tether Tension|	Improvement over Baseline
Cartesian Baseline	2.38 N	–
Spherical PID/PD *	1.16 N	51.3%
Spherical PID/PD with FF	1.83 N	23.1%
Spherical PID/PD with FF and RCG	1.53 N	35.7%

* Violates tether shape constraints

Figure 5-18 clearly demonstrates the problem with the Cartesian system operating on a tether as the magnitude of force of tension on the tether is increasing while the aircraft is in approximate steady state flight. This figure also verifies that the conversion to a PID/PD controller in spherical coordinates solves this problem–the force of tension for all spherical controller configurations is constant during steady state flight.

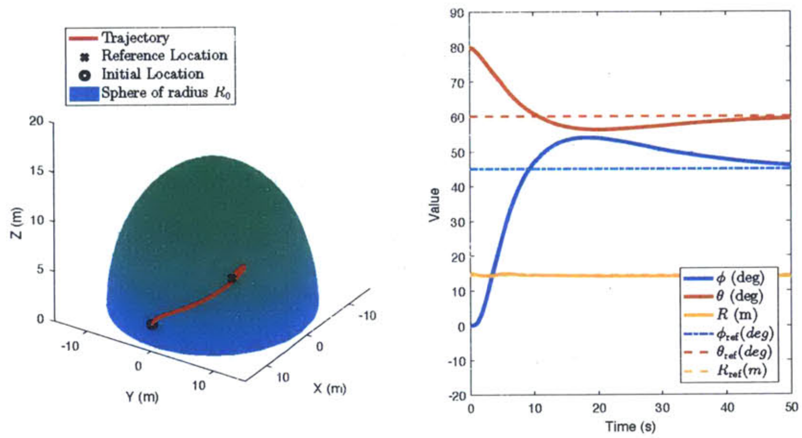

Figure 5-16: Spherical Position PID/PD Controller with FF and RCG: Trajectory and State Information

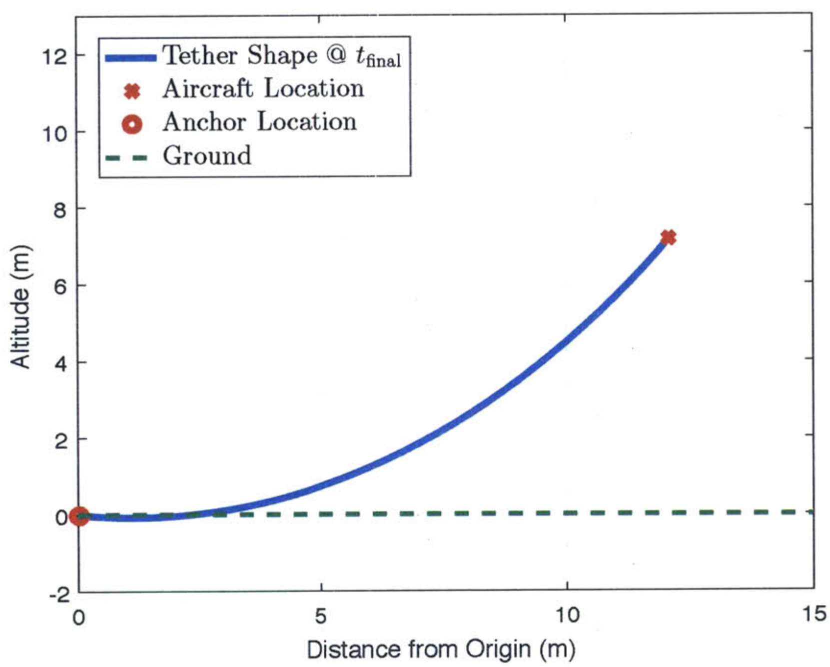

Figure 5-17: Spherical PID/PD Position Controller with FF and RCG: Tether Shape

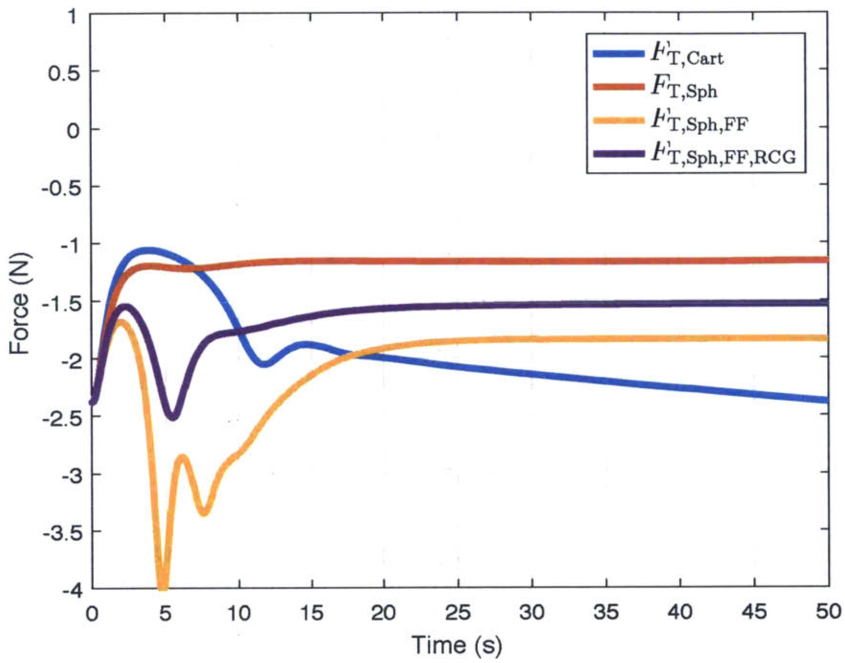

Figure 5-18: Comparison of Force of Tension on Multirotor UAV

5.3.1.5 Verification Testing Conclusion

From this series of verification flights in simulation, we have verified that the proposed spherical position controller, consisting of a PID/PD feedback loop, a feed forward tether model, and reference command generator, adequately solves the problems associated with flying a multirotor UAV on a tether.

Each component of the proposed controller was implemented sequentially in order to understand its effect on the system, but did not yield any additional concerns under standard operation. The controller retained good reference command tracking in directions unconstrained by the tether with no steady state error, and utilizes a safe and stable method for reference tracking in the direction constrained by the tether. The controller not only decreased the tension force on the aircraft, but allowed intelligent use of the dynamics to control the shape of the tether in flight.

5.3.2 Validation Testing Results

The validation testing for the proposed spherical position controller was designed to confirm the controllers stable operation under real world conditions where the specified models do not match reality. The three real world scenarios are wind acting on the multirotor and tether system, an incorrect linear density of the tether material, and an incorrect tether length. In the interest of using this controller at different tether lengths, the controller will also be tested at a longer tether length to confirm that the only controller parameter that needs to be updated is the tether length L.

5.3.2.1 Wind Force on Aircraft and Tether

The aircrafts trajectory and state information for the wind validation test of the spherical position control system is presented in Figure 5-19. Figure 5-20 shows the position controllers error integrators. Figure 5-21 shows the position controller output in the inertial reference frame. Figure 5-22 presents the force exerted onto the aircraft by the tether tension in the inertial reference frame.

This test was conducted to understand how the controller would react to a windy environment, and most importantly, confirm that the controller would remain stable, and not exhibit excessive tension forces or control outputs. It is expected that the error tracking in the unconstrained directions ϕ and θ will remain zero, and subsequently that the aircraft will remain on the specified ray $\hat{R}$. However due to the lack of an integrator in the constrained R direction, some steady state error in R is expected.

From Figure 5-22, it is apparent that the aircraft and tether have reached an equilibrium state, and is not at risk of instability or increasing tension. This test showed similar transient controller error integration to the final verification test in Section 5.3.1.4, however in this test the integrators do not return to zero, indicating that they are properly mitigating the external wind disturbance.

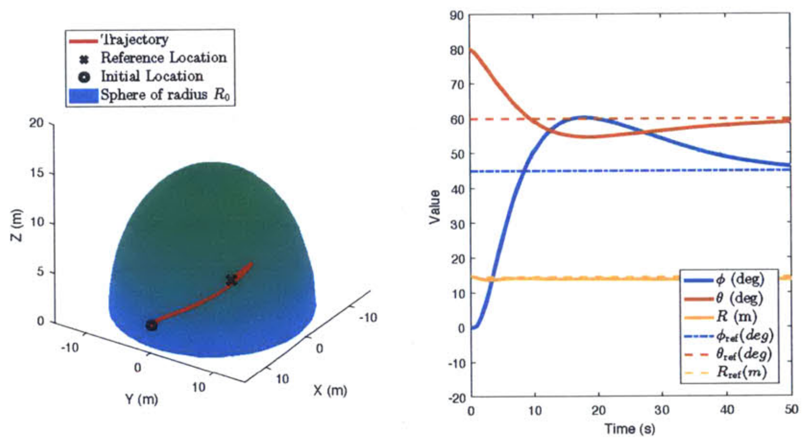

Figure 5-19: Wind Validation Testing: Trajectory and State Information

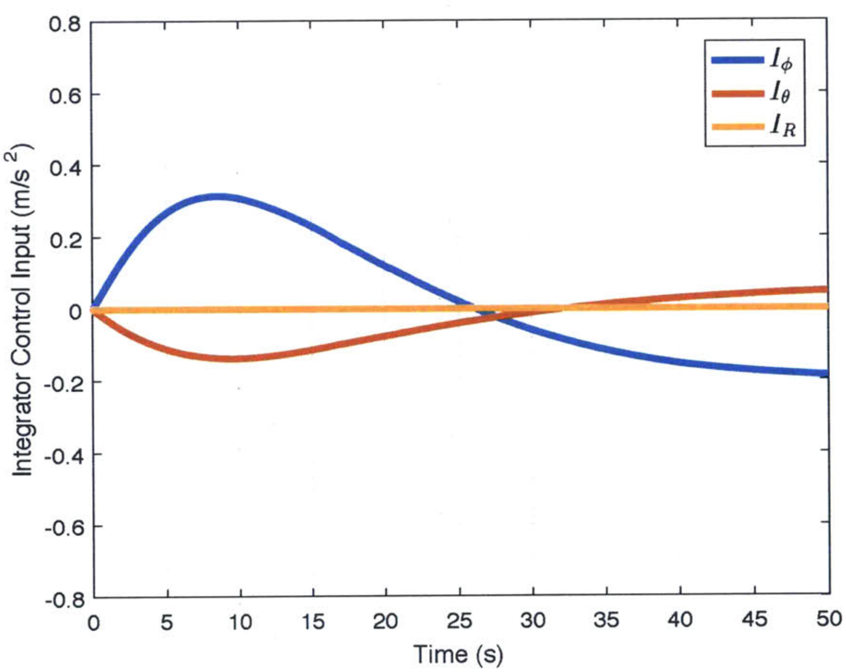

Figure 5-20: Wind Validation Testing: PID Control Integrators

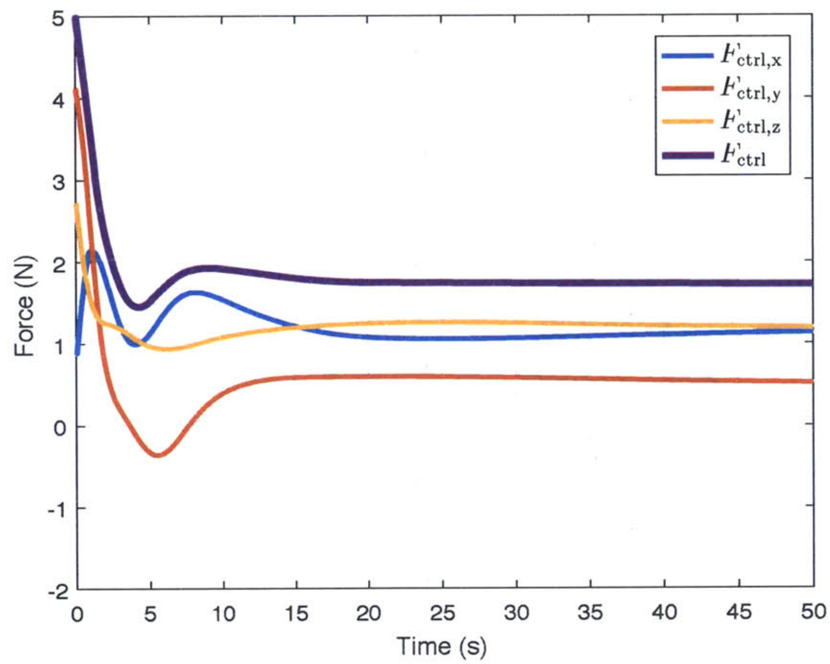

Figure 5-21: Wind Validation Testing: Position Controller Force Output

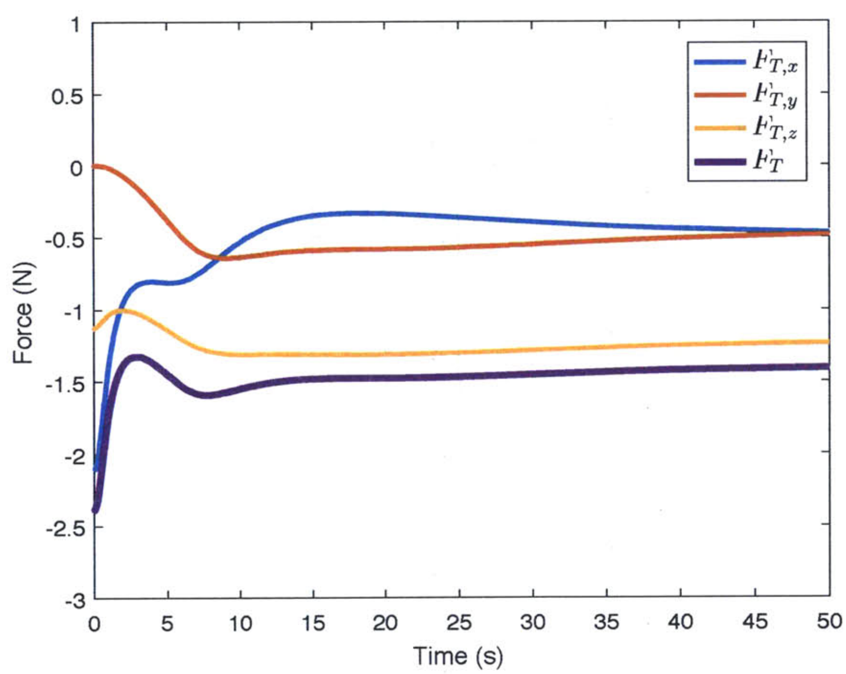

Figure 5-22: Wind Validation Testing: Tether Tension

5.3.2.2 Incorrect Tether Linear Density

The aircrafts trajectory and state information for the incorrect tether linear density validation test of the spherical position control system is presented in Figure 5-23. Figure 5-20 shows the position controllers error integrators. Figure 5-24 shows the position controller output in the inertial reference frame. Figure 5-22 presents the force exerted onto the aircraft by the tether tension in the inertial reference frame.

Practically, this validation test is simulating a heavier tether than anticipated. From that, it is expected that the tether would sag more, which is seen in Figure 5.3.2.2. Although it takes time for the integrators to compensate for the additional external force, the controller is able to reach the reference location by the end of the simulation, with only a small error in R. Similar to the wind validation testing, the controller is not expected to reduce steady state error in R to zero, but rather remain aligned with the $\hat{R}$ vector specified by the unconstrained directions reference commands ϕ_{ref} and θ_{ref}.

This test shows that the position controller is stable and reached an equilibrium value under incorrect tether mass assumptions. Neither the controller outputs nor tether tension show signs on increasing over the course of the simulation.

5.3.2.3 Incorrect Tether Length

The aircrafts trajectory and state information for the incorrect tether length validation test of the spherical position control system is presented in Figure 5-26. Figure 5-27 shows the position controllers error integrators. Figure 5-28 shows the position controller output in the inertial reference frame. Figures 5-29 and 5-30 present the force exerted onto the aircraft by the tether tension in the inertial reference frame and the tether shape in two dimensions, viewed from the side.

This validation test was designed to observe the controllers response to a situation where the real tether length is shorter then expected by the tether model, and will ultimately support the decision to not have an error integrator in the R direction. In Figure 5-29, the tether tension quickly spikes to large values, indicating that the

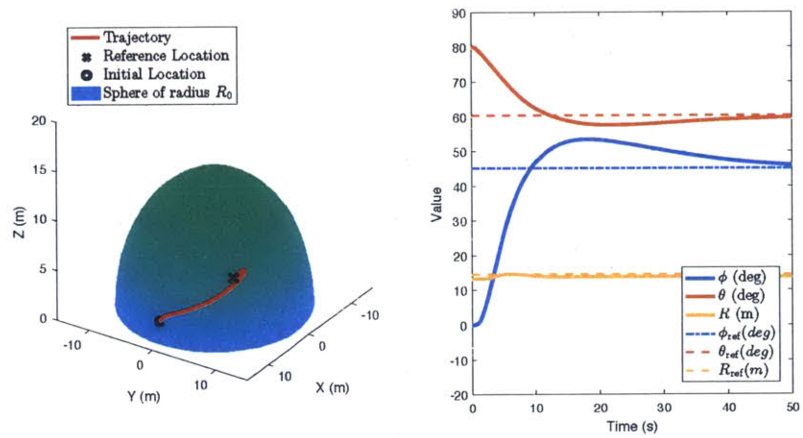

Figure 5-23: Tether Linear Density Validation Testing: Trajectory and State Information

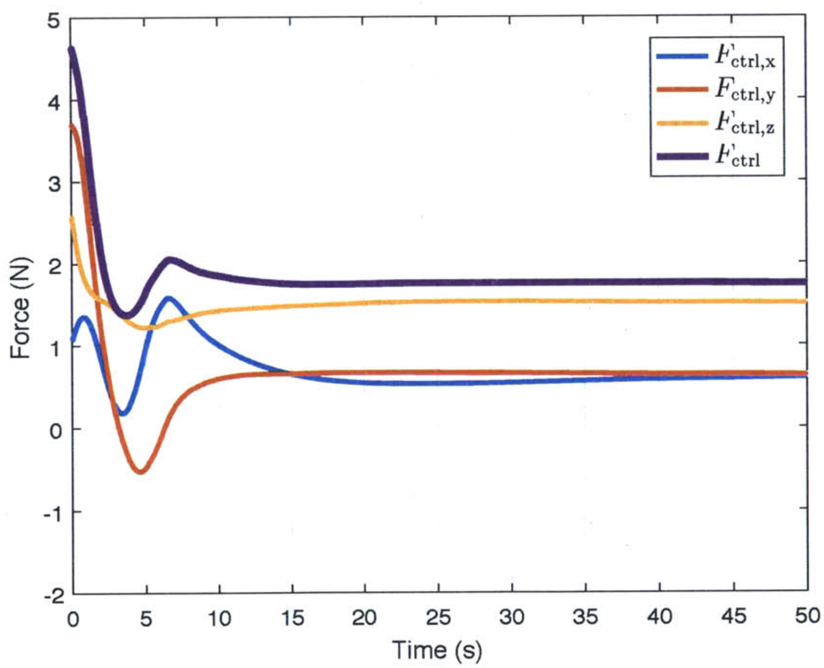

Figure 5-24: Tether Linear Density Validation Testing: Position Controller Force Output

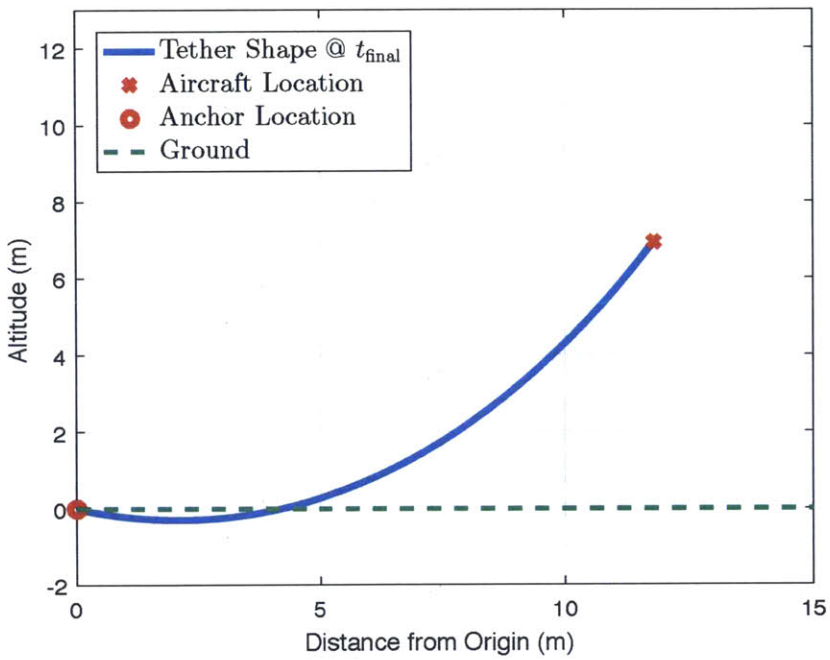

Figure 5-25: Tether Linear Density Validation Testing: Tether Shape

aircraft is attempting to fly to its reference location that is outside the area constrained by the tether. While there is a small spike in controller force output, shown in Figure 5-28 at $t = 5$ seconds, this force spike quickly settles to a steady state value, indicating two important properties of the controller. The first being that the feed forward model does not diverge under when the aircraft quickly tensions the tether, and the second is that the controller does not fight the tether to reach its reference location.

This controller simulation validates a major design choice for this tethered UAV position controller, that there should not be error integration in the R direction. In scenarios such as these, where there is a large error in R, an integrator in this direction would quickly wind up, applying excessive tension onto the tether, and risk actuator saturation if left to increase without proper saturation and and accompanying control margins.

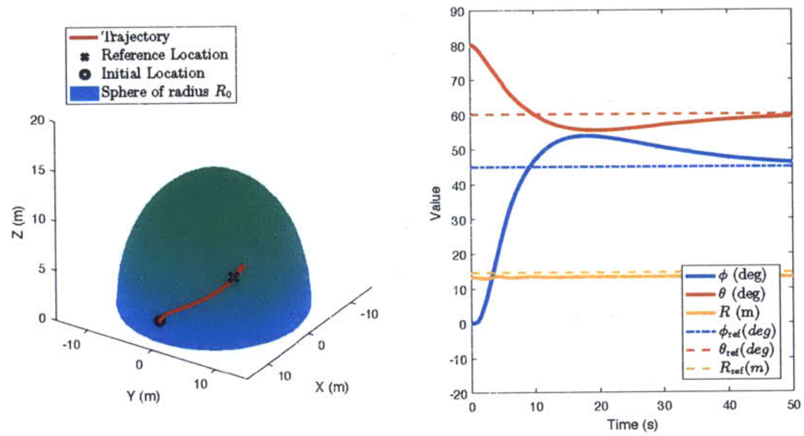

Figure 5-26: Tether Length Validation Testing: Trajectory and State Information

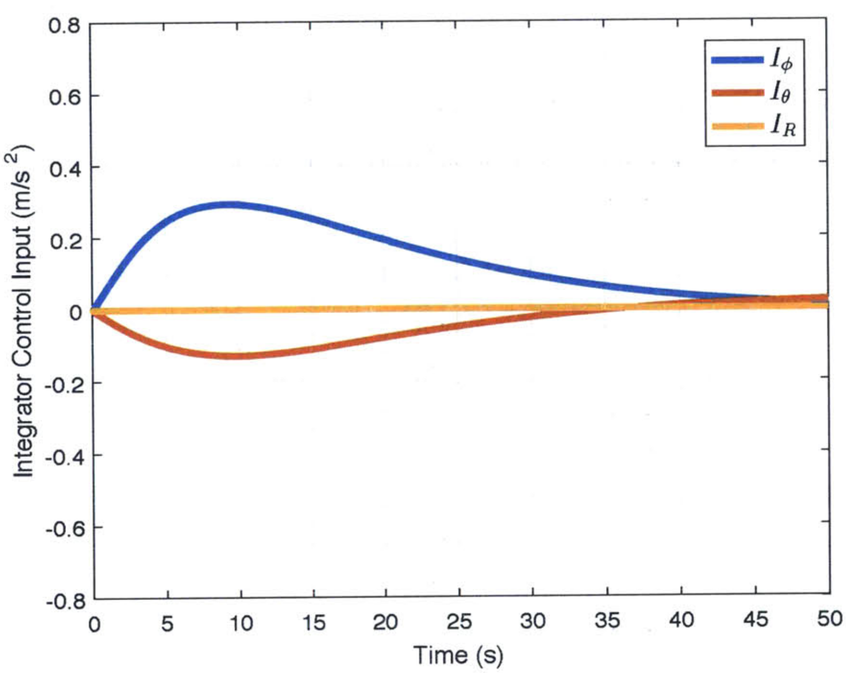

Figure 5-27: Tether Length Validation Testing: PID Control Integrators

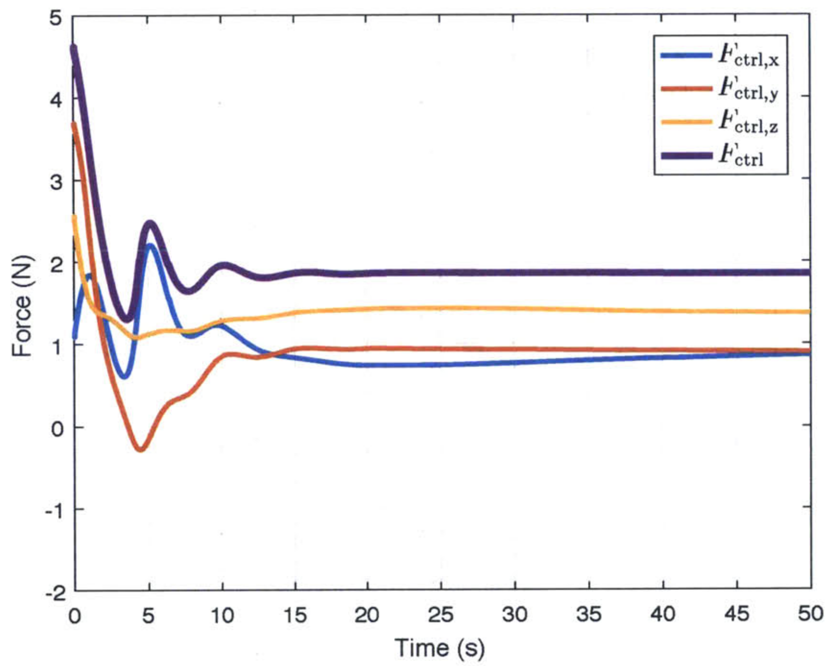

Figure 5-28: Tether Length Validation Testing: Position Controller Force Output

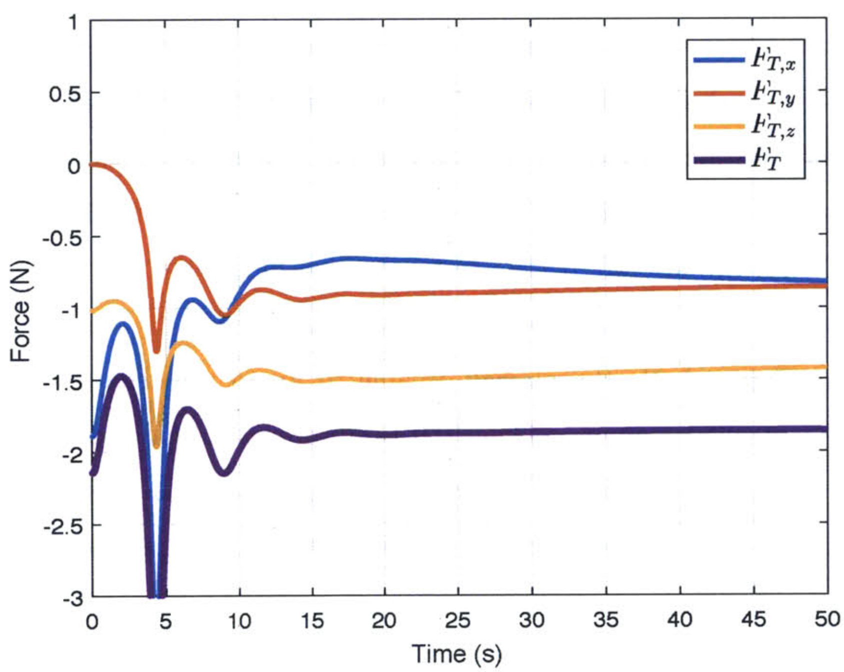

Figure 5-29: Tether Length Validation Testing: Tether Tension

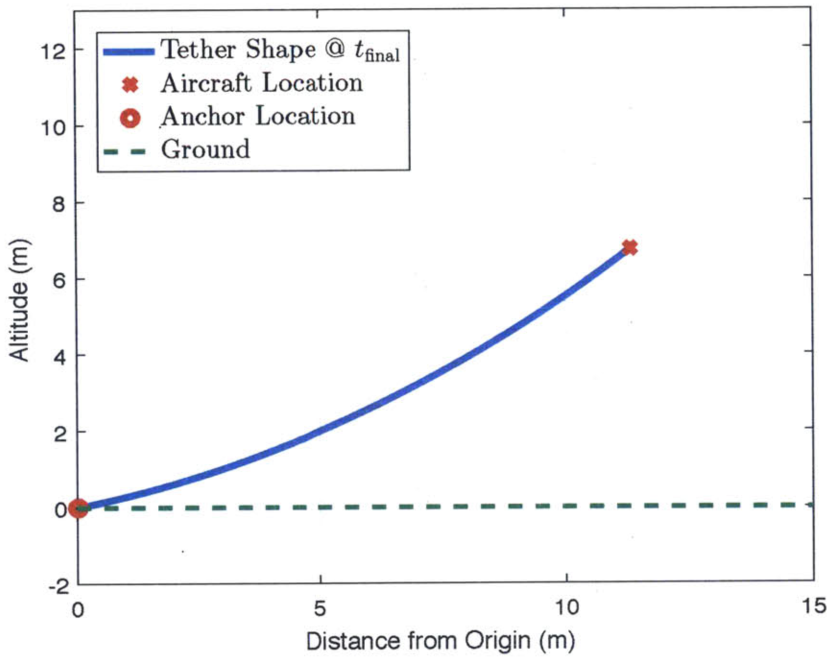

Figure 5-30: Tether Length Validation Testing: Tether Shape

5.3.2.4 Increased Tether Length

The aircrafts trajectory and state information for the increased tether length validation test of the spherical position control system is presented in Figure 5-31. Figure B-11 shows the position controllers error integrators. Figure B-12 shows the position controller output in the inertial reference frame. Figures B-13 and 5-32 present the force exerted onto the aircraft by the tether tension in the inertial reference frame and the tether shape in two dimensions, viewed from the side.

As seen in Figure 5-31, the aircraft is able to fly to the reference location in a stable and controlled manner. Thus, the position control gains are independent of the tethers operating length for the range of applicable tether lengths, with the assumption that the aircraft has enough available thrust to compensate for the tether dynamics.

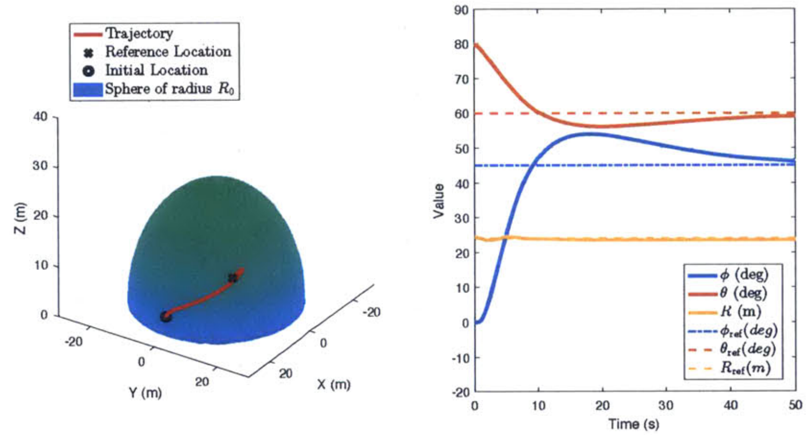

Figure 5-31: Tether Length Increase Validation Testing: Trajectory and State Information

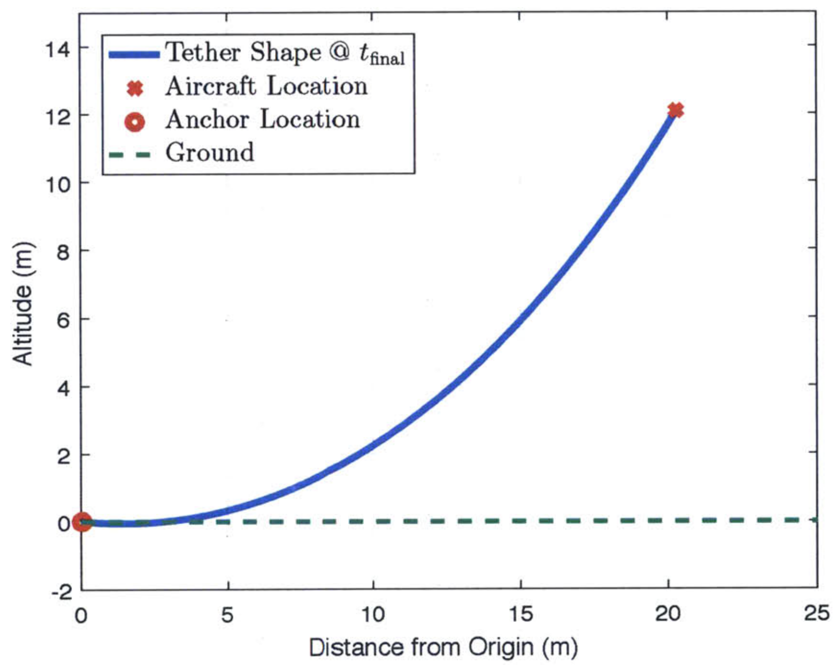

Figure 5-32: Tether Length Increase Validation Testing: Tether Shape

5.3.2.5 Validation Testing Conclusion

These validation tests aimed to evaluate the controllers ability to handle a variety of external disturbances and modeling errors that it might encounter when operating in a real world scenario. The wind test showed the aircraft remained stable and at the desired reference location with the presence of an external force acting upon both the aircraft and the tether system. Changing the simulated tether's linear density showed the controllers ability to compensate for modeling and parameter errors within the controller and controller feed forward models. The test where the tether was shorter than expected demonstrated the importance of the controllers lack of an state error integrator in the R direction, as well as the robustness compared to the traditional Cartesian system that this proposed controller was designed to replace for tethered multirotor flight operations. The final test simply confirmed that the controller works at different tether lengths without modification, not just $L = 15m$ as initially simulated. These tests established explicit confidence in the controller such that it was deemed adequate to proceed to real hardware implementation and testing.

Chapter 6

Indoor Flight Testing

6.1 Testing Motivation

Indoor flight testing in the RAVEN Indoor Flight Space at MIT's Aerospace Controls Laboratory provided a real-world test environment to observe and understand the unique problems associated with flying a multirotor aircraft on the end of a tether. The primary motivation for conducting indoor flight testing was to provide verification and validation for the proposed spherical position control system.

There were two motivations behind verification testing on the spherical position controller during indoor flight testing. The first was to confirm that the control system worked using real hardware in the indoor flight space, and that the vehicle was capable of steady, stable flight. The second verification motivation was to compare the spherical controller to the traditional Cartesian position control system, specifically to confirm the problems associated with tethered operation and compare power consumption. The Cartesian system was predicted to consume additional power due to it exerting excess force onto the tether, while the proposed spherical system was designed to only exert the minimum force required to maintain the tether shape at a minimum tension. The problems associated with Cartesian systems are outlined in Chapter 3, based around the notion that error integration in the direction of the tether will cause increasing control effort in $\hat{R}$.

While not specifically tested for, the verification testing of the spherical position controller will demonstrate that the nominal system can mitigate aircraft based disturbances that arise when using real hardware. One significant disturbance is the attitude control system on the aircraft, which operates using a PD controller and is not guaranteed to hold the position controllers desired attitude. Other small internal disturbances that can impact the aircraft control system are actuator variability and vibration. These disturbances are not directly tested against, however their presence in all indoor flight testing demonstrate the controllers ability to mitigate these small errors and maintain good performance.

The motivation for validation testing of the proposed spherical position control system is to confirm that the controller operates as expected in the presence of real world modeling errors and external disturbance forces. The controller should exhibit good tracking performance over a desired trajectory with no steady state error in the unconstrained directions ϕ and θ, and limited steady state error in R. The desired modeling errors to test are decreasing the tether length and an incorrect tether linear density λ_m. The main predicted external force on the system is a wind drag force acting upon the aircraft and tether system. The last validation test will be to demonstrate that the system is not dependent on the tether length, and can operate on a longer tether with modifying control gains or structure.

6.2 Experimental Design

The purpose of these indoor flights tests were to validate the proposed spherical control system in a real world environment, with external disturbances present.

6.2.1 Controller Verification

6.2.1.1 Nominal System

The first purpose of the spherical controller verification testing was to confirm that the control system operated in a stable, robust manner on real hardware and confirm that the controller reduces tether tension and power consumption during flight over

Figure 6-1: Picture of QAV250 flying during indoor flight testing.

the baseline Cartesian system.

In order to test these motivation's the aircraft was flown along a pre-defined trajectory on the end of the tether. This reference trajectory, summarized below in Table 6.1 and shown in Figure 6-2, was designed to emulate real operation, requiring the aircraft to fly a grid pattern around the anchor location. The chosen trajectory was a box pattern along the surface of the constrained sphere. The aircraft was flown along this reference trajectory using the baseline Cartesian position control system, followed by the proposed spherical control system.

The spherical position controllers stability and performance in the presence of real world internal disturbances was evaluated using this verification test. It was expected that the controller would show good tracking along the unconstrained directions ϕ and θ, even with small disturbances and variations in motor control and battery voltage.

Table 6.1: Reference locations for Verification Testing

ϕ_{ref} $(degrees)$	0	0	-60	-60	0	60	60	10	10
θ_{ref} $(degrees)$	90	80	80	60	60	60	80	80	90
L $(meters)$	3	3	3	3	3	3	3	3	3

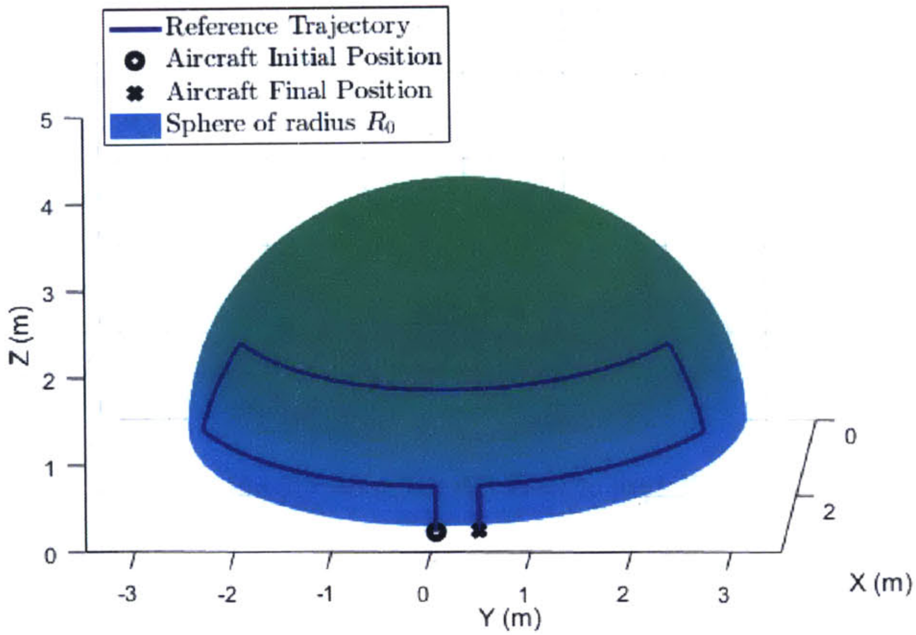

Figure 6-2: Reference Trajectory for Verification Testing

6.2.1.2 Power Consumption

The second motivation for verification testing is to evaluate the power efficiency increase of the spherical position control system over the Cartesian system. During a series of four flights per controller, the control system will log the throttle setting onboard the aircraft, allowing the average power consumption of the vehicle to be calculated after the flight. This conversion used an experimentally determined mapping between body force and power consumption. Using the same four trajectories allows the direct comparison of the aircrafts power consumption during flight between the two position control systems.

However the power consumption, mainly the excessive power consumption in the Cartesian system, is dependent on the aircrafts flight trajectory. This dependence

Table 6.2: Power Consumption Reference Flight Trajectory 1

ϕ_{ref} *(degrees)*	0	45	45
θ_{ref} *(degrees)*	90	60	90
L *(meters)*	3	3	3
Hold For (sec)	–	60	–

Table 6.3: Power Consumption Reference Flight Trajectory 2

ϕ_{ref} *(degrees)*	0	0	-60	-60	0	60	60	10	10
θ_{ref} *(degrees)*	90	80	80	60	60	60	80	80	90
L *(meters)*	3	3	3	3	3	3	3	3	3

Table 6.4: Power Consumption Reference Flight Trajectory 3

ϕ_{ref} *(degrees)*	0	0	0	60	60	10	10
θ_{ref} *(degrees)*	90	80	60	60	80	80	90
L *(meters)*	3	3	3	3	3	3	3

Table 6.5: Power Consumption Reference Flight Trajectory 4

ϕ_{ref} *(degrees)*	0	0	-50	-50	0	60	60	0	-60	-60	-10
θ_{ref} *(degrees)*	90	80	80	70	70	70	60	60	60	80	90
L *(meters)*	3	3	3	3	3	3	3	3	3	3	3

is due to the fact that the Cartesian controllers error integrators need time to wind up in the presence of error in the R direction. Scenarios where the Cartesian error in $\hat{R}$ changes sign, the excessive power consumption will be reduced. In order to both quantify the excessive power consumption and observe the dependence of power consumption on the flight trajectory, the following flight trajectories were flown using both the spherical and Cartesian system, and the average power consumption computed. Trajectory 1 aims to evaluate the power consumption at a fixed location in space for a fixed period of time, while trajectories 2-4 move the aircraft in a similar trajectory that would be seen in a real-world mission.

6.2.2 Controller Validation

The second stage to indoor flight testing was validation that the controller will operate in a real world scenario. This translated to designing indoor flight tests that changed the dynamics of the tether system such that they deviate from the models, and evaluate how the position controller compensates for the new errors.

During all of the validation testing the PID/PD, feed forward, and reference command functions and controller parameters were left constant, while the environment parameters were modified to reflect real-world deviations from the models. The deviation in the models was designed to mimic the effect of wind on the tether, incorrect tether linear density, and incorrect tether length. These tests evaluated the controllers response to disturbances using a reference trajectory, which then remained constant for for these three tests. This structure flew the aircraft on a known, fixed real-world trajectory, while allowing analysis of the state error, tether tension, and stability in the presence of a disturbance. For these three tests, the trajectory is summarized below in Table 6.6.

Table 6.6: Reference Locations for Validation Testing

ϕ_{ref} $(degrees)$	0	0	-60	-60	0	60	60	10	10
θ_{ref} $(degrees)$	90	80	80	60	60	60	80	80	90
L $(meters)$	3	3	3	3	3	3	3	3	3

The last validation testing was to demonstrate that the position controller operated independent of the tether length. For this case, the tether was extended to a longer length, and the position control system was told how long the new tether length was. No position controller gains were modified, nor any tether model parameters aside from the tether length input.

6.2.2.1 Wind Testing

The first validation test was designed to evaluate the controllers response to wind acting on the aircraft in the inertial $-\hat{Y}$ direction. The wind created a drag force on the aircraft and tether system, which was not modeled by the control system. The wind was generated using a large industrial fan during the flight, which pushed turbulent air at a measured velocity of $v_{\text{wind}} \approx 4\frac{m}{s}$. The spherical control system was expected to use the state error integrators in order to reduce steady state error during this disturbance test. The reference flight trajectory is summarized above in Table 6.6.

6.2.2.2 Incorrect Tether Linear Density

The second validation test was designed to evaluate the controllers response to an incorrectly modeled tether linear density. Practically, this test was was to see the the feed forward controllers response to the weight of the tether being incorrect, and confirm that the PID/PD controller would compensate for the error. The mass of the tether is defined as

$$m_{tether} = \lambda_m \cdot L \tag{6.1}$$

and is a key term in determining the force of tension on the multirotor. The parameter λ_m could be wrong due to material variability, or it may change during the flight if it gets wet. For the purpose of this test, the true linear density of the tether was increased by %25 within the feed forward and reference command functions, with $\lambda_m = 0.0166\frac{kg}{m}$. The reference flight trajectory is summarized above in Table 6.6.

6.2.2.3 Reduced Tether Length L

The next validation test performed in the indoor flight testing environment was to evaluate the controllers ability to compensate for an incorrect tether length. This scenario could arise if the tether length is incorrectly estimated or measured, and will ultimately have a two-fold effect on the tether dynamics and controller. The first effect is that the tether will be shorter than the controller is compensating for, causing the controller to attempt to fly to a location it cannot reach. The second effect is that the mass of the tether will be lighter than the model estimates, as there is less tether for the aircraft to lift. For this test, the tether length L was reduced by %10, resulting in an actual tether length of $2.7m$, while the controller is still operating with information that the tether length is $3m$. The reference flight trajectory is summarized above in Table 6.6.

6.2.2.4 Long Tether Length

The last validation test was performed to demonstrate that the controller gains and parameters were independent of the tether operating length. For this test, aircraft

Table 6.7: Reference Locations for Long Tether Length Validation Testing

ϕ_{ref} (*degrees*)	0	0	-10	-10	0	10	10	5	5
θ_{ref} (*degrees*)	90	80	80	70	70	70	80	80	90
L (*meters*)	10	10	10	10	10	10	10	10	10

ws flown on the end of a $L = 10m$ tether. The controller positional PID/PD gains remained constant, and the operational tether length L was changed to reflect the actual tether length. Due to indoor constraints, there was a small area where the aircraft could operate on the end of such a long tether, and as a result, the reference trajectory was modified to only include a small area where the aircraft remained visible to the motion capture system, and not endangering people or equipment. The reference trajectory for this test is summarized below in Table 6.7.

6.3 Experimental Results

6.3.1 Controller Verification Results

6.3.1.1 Nominal System

For this verification test of the spherical position controller, the aircrafts state and trajectory are shown in Figure 6-3. The state error is shown in Figure 6-4, and corresponding control error integrators are shown in Figure 6-5. Figure 6-7 show the spherical position controllers control outputs, and Figure 6-8 show the shape of the tether at $t = 40sec$. The same trajectory was flown using the Cartesian system and the control integrators are shown in Figure 6-6 and the tether shape at $t = 40sec$ is shown in Figure 6-9

This test involved two separate flights, one utilizing the traditional Cartesian position control system, and the other using the spherical position control system. This comparison was performed to confirm the fundamental problems with the Cartesian system, which was integration leading to increased force on the tether. Figures 6-5 and 6-6 show the control error integration for each controller respectively, and clearly show that the Cartesian system is integrating error in the direction of R. This error

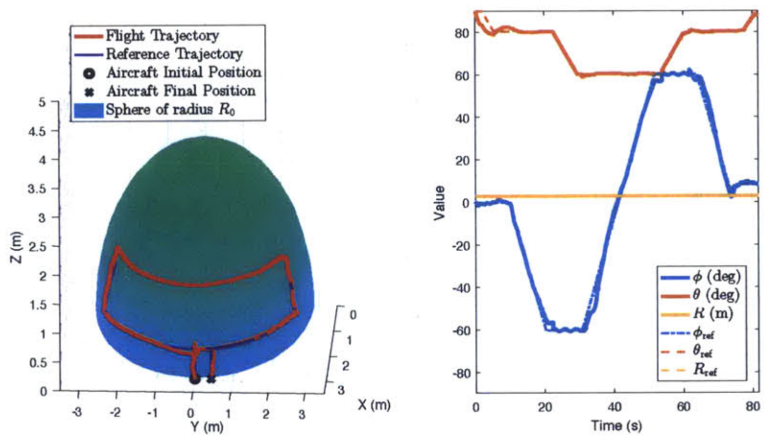

Figure 6-3: Spherical Controller Indoor Verification Flight: Trajectory and State Information

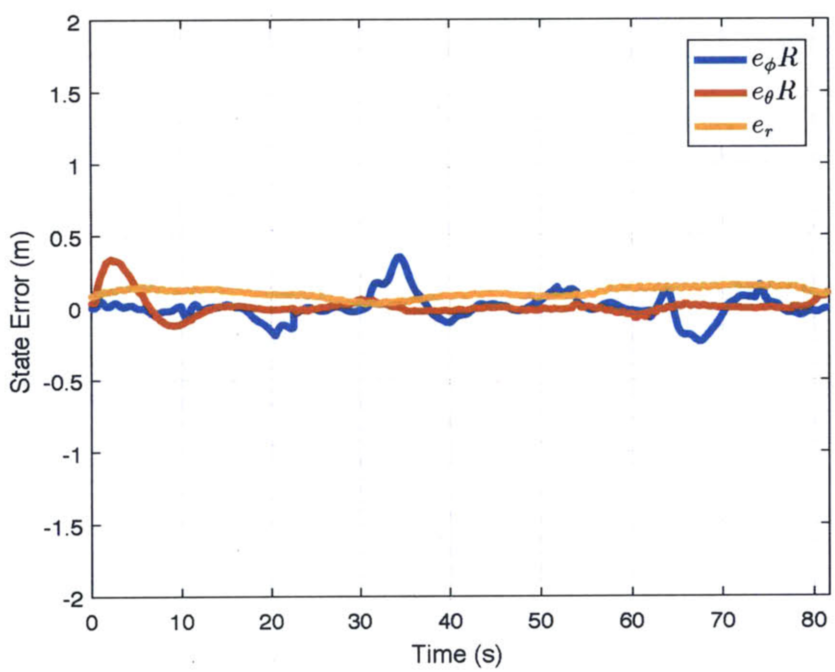

Figure 6-4: Spherical Controller Indoor Verification Flight: State Error

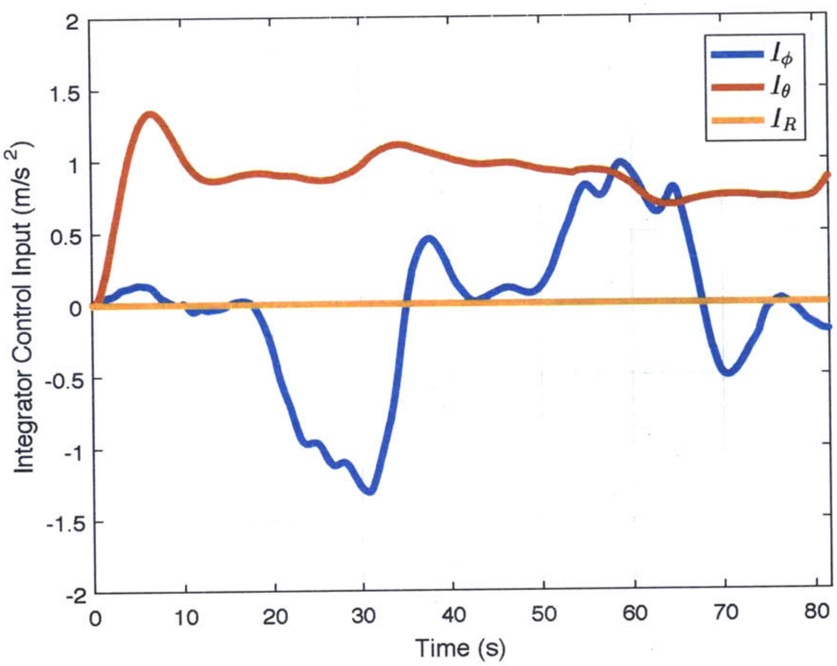

Figure 6-5: Spherical Controller Indoor Verification Flight: Control Integrators

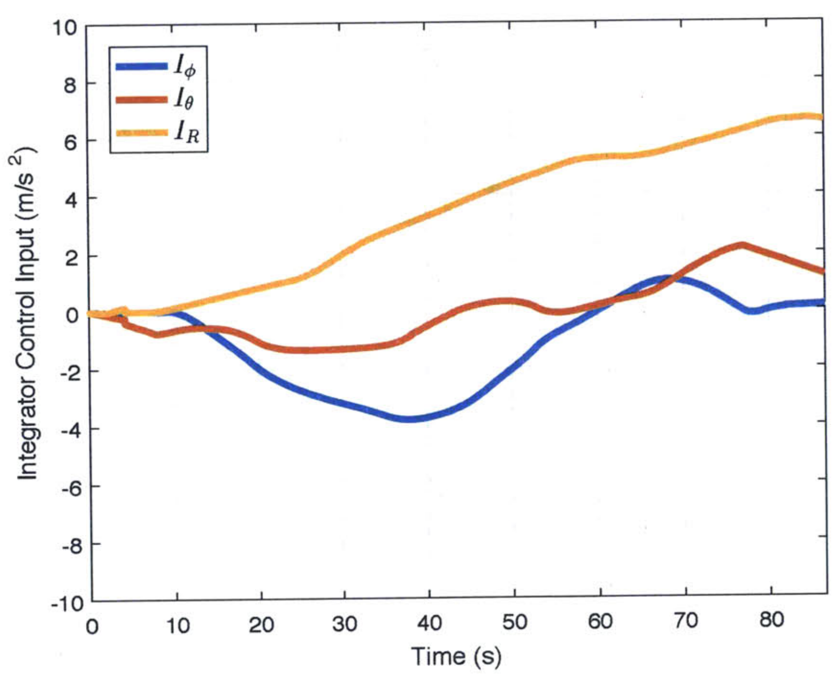

Figure 6-6: Cartesian Controller Indoor Verification Flight: Control Integrators

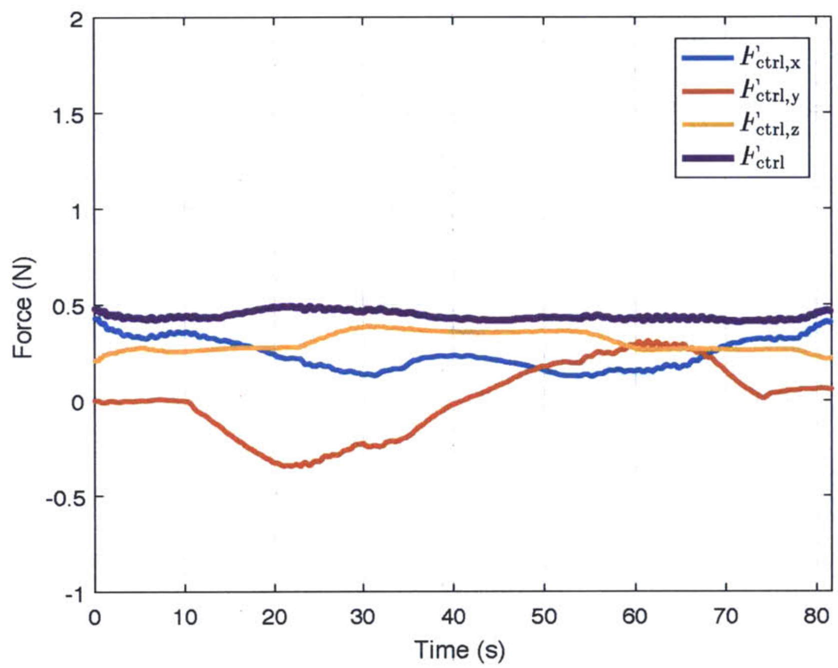

Figure 6-7: Spherical Controller Indoor Verification Flight: Control Outputs

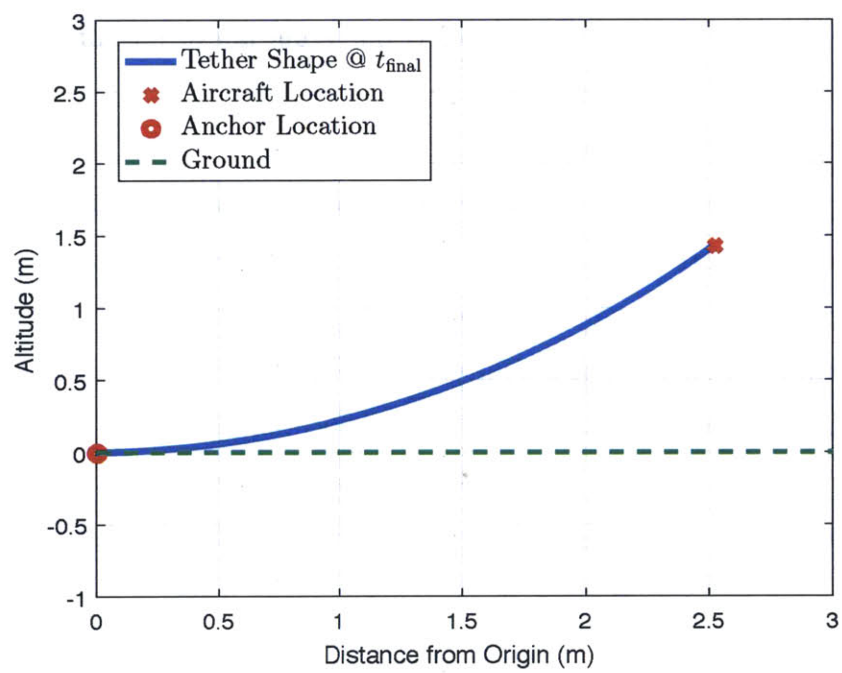

Figure 6-8: Spherical Controller Indoor Verification Flight: Tether Shape at $t = 40sec$

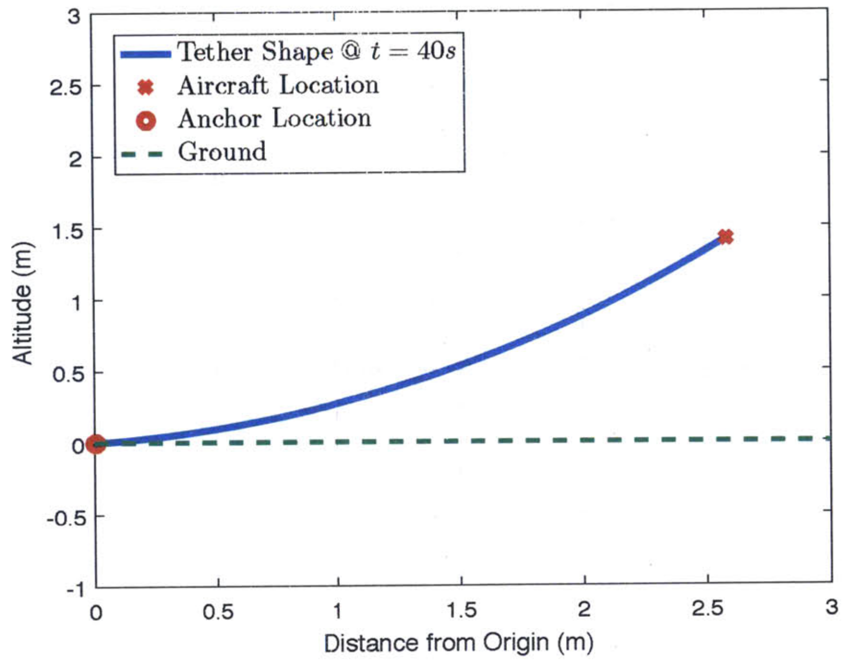

Figure 6-9: Cartesian Controller Indoor Verification Flight: Tether Shape at $t = 40sec$

integration leads to steadily increasing in tether tension, which is depicted in the tether shape in Figure 6-9, as the tether is operating above its minimum tension criteria.

These plots show that the spherical position controller can accurately follow a reference trajectory with minimal state error. Figure 6-5 shows steady state reliance on I_θ, however this control input is most likely attributed to the aircraft throttle gain not being high enough, and as it remains constant during the flight, is of no significant concern regarding the controllers stability or operation. The control inputs in Figure 6-7 show a fairly constant total control effort, indicating the system is not fighting the tether and operating as expected over the course of the trajectory. Figure 6-8 shows that the tether shape midway through the flight is close to the optimal shape with $\frac{dy}{dx} = 0$.

6.3.1.2 Power Consumption

The second part of this verification test was to quantify the power consumption between the Cartesian and the spherical position controller. It was predicted that the spherical position controller would use less power, as it was exerting the minimum tension onto the tether, opposed to the Cartesian system that as exerting excessive tension on the tether. In order to quantify this power decrease, the total throttle output, thr, was recorded during flight for both controllers and converted to power consumption using an experimentally derived mapping between throttle and power for the specific multirotor aircraft used for indoor flight testing, shown below.

$$P(thr) = 480.22(thr)^2 + 12.26(thr) + 2.1 \tag{6.2}$$

The average continuous power consumption was then calculated for each controller and shown in Table 6.8. The spherical position controller showed a 12.2% decrease in continuous power consumption over the Cartesian system. This decrease in power consumption is flight trajectory dependent, and not applicable for all flight trajectories. The specific flight trajectory can change power consumption, because the transition from a negative to positive ϕ will require the error integrators to transit through zero while eliminating steady state error. The power inefficiency of the Cartesian system stems from excessive error integration, and thus this transition temporarily decreases error integration while the vehicle is transitioning across $\phi = 0$, temporarily reducing power consumption. For this evaluation, the flight trajectory was constant between the two flights and a freshly charged battery was used for every flight. These two constraints allow comparison between the power consumption of the two controllers.

Table 6.8: Average Continuous Power Consumption Comparison

Flight Controller	Test 1 (W)	Test 2 (W)	Test 3 (W)	Test 4 (W)
Cartesian	88.59	88.72	86.93	87.31
Spherical	80.69	81.15	80.23	79.87
Percent Decrease	8.9%	8.5%	7.7%	8.5%

6.3.1.3 Verification Testing Conclusion

These verification tests were designed to confirm that the spherical position controller was stable and performed well when using a real multirotor aircraft under nominal conditions. The spherical position controller showed good tracking of the trajectory, and kept the tether under the minimum tension to fulfill the shape constraints. These tests also compared the power consumption of the spherical and Cartesian position controllers for a given pre-planned flight trajectory. The Spherical position controller showed a 7.7% to 8.9% decrease in power consumption over the traditional Cartesian position control system.

6.3.2 Controller Validation Results

6.3.2.1 Wind Testing

For this validation test of the spherical position controller, the aircraft was flown in a windy, turbulent environment, introducing external forces and disturbances onto the system. The aircrafts state and trajectory are shown in Figure 6-10. The state error is shown in Figure B-14, and corresponding control error integrators are shown in Figure B-15. Figure 6-11 show the spherical position controllers control outputs, and Figure 6-12 show the shape of the tether at $t = 40sec$.

Figure 6-10 shows that the vehicle is able to track the reference trajectory while a wind drag force is acting upon the aircraft and tether system. This validation test shows more state error and controller integration than the nominal verification test, however the quad was flying in a very turbulent environment, and remained stable for the duration of the flight. Figure 6-11 shows the control effort output by the spherical position controller remained fairly constant over the flight with no signs of arbitrary increase, and Figure 6-12 shows that the controller was able to maintain proper tether shape to minimize tension. This validation test concludes that the spherical position controller can stably and accurately follow a reference trajectory in the presence of wind.

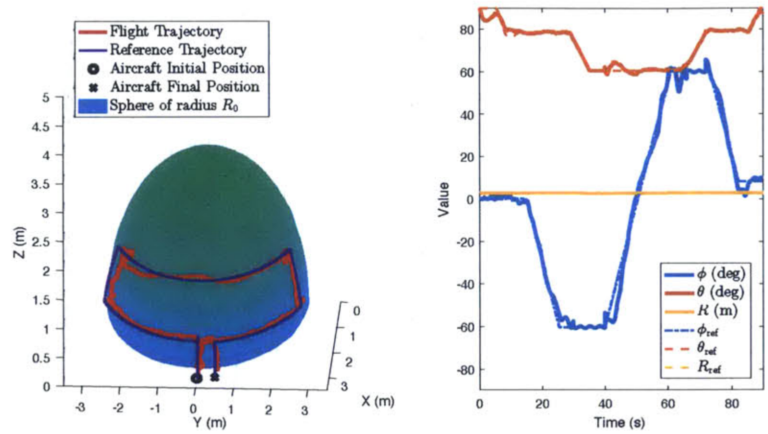

Figure 6-10: Spherical Controller Indoor Wind Testing: Trajectory and State Information

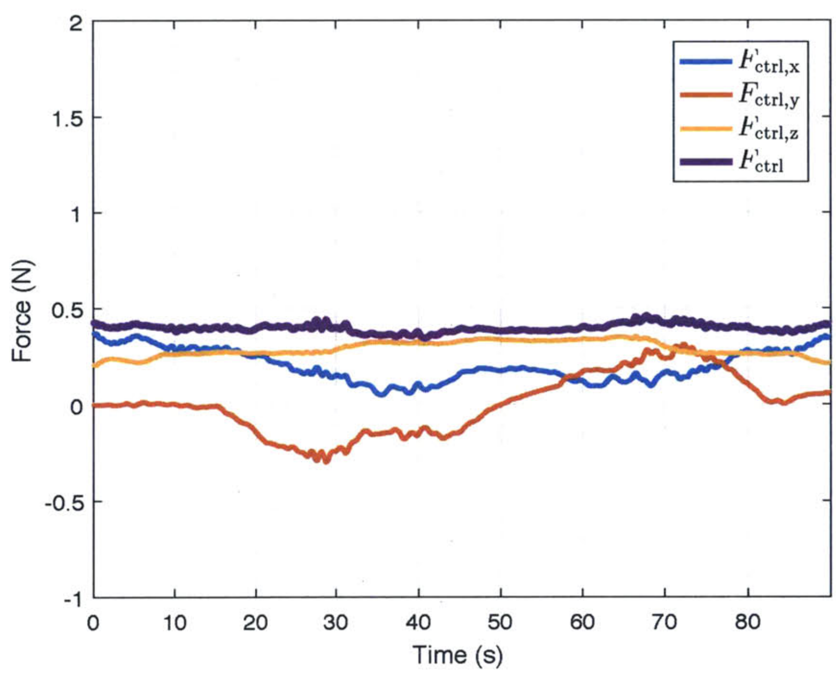

Figure 6-11: Spherical Controller Indoor Wind Testing: Control Outputs

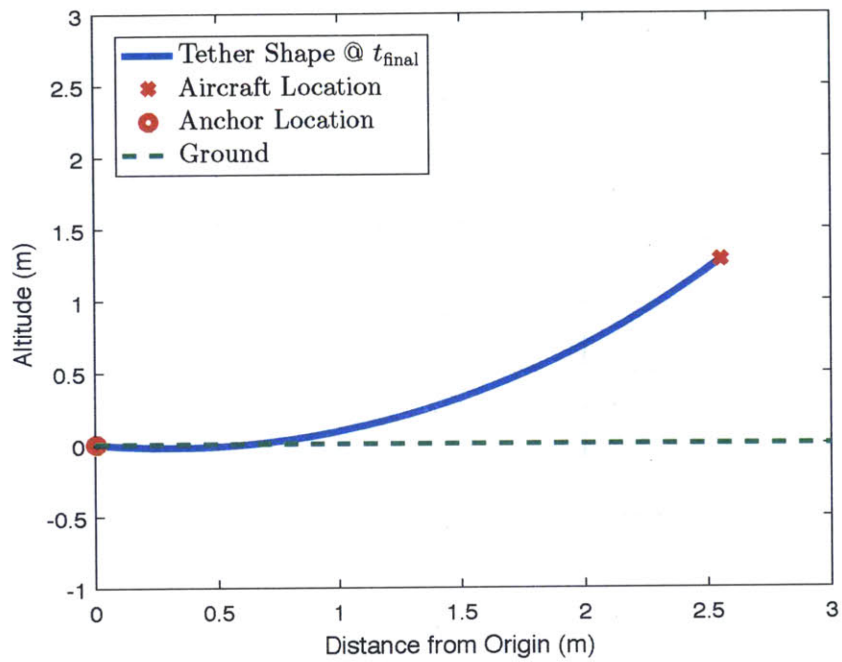

Figure 6-12: Spherical Controller Indoor Wind Testing: Tether Shape at $t = 40sec$

6.3.2.2 Incorrect Tether Linear Density

For this validation test of the spherical position controller, the controller was flown using an incorrect tether linear density, generating an incorrect mass estimate of the tether system. The aircrafts state and trajectory are shown in Figure 6-13. The state error is shown in Figure B-16, and corresponding control error integrators are shown in Figure B-17. Figure 6-14 show the spherical position controllers control outputs, and Figure 6-15 show the shape of the tether at $t = 40sec$.

In this test the tether was lighter than the spherical position controller expected, and as a result, the aircraft periodically flew at $R > R_{\text{ref}}$. this is seen in the trajectory plot in Figure 6-13, however is better understood by looking at the tether shape in Figure 6-15. With the controller compensating for a heavier tether, the multirotor is exerting more tension than necessary for the lighter tether, causing $\frac{dy}{dx} > 0$ at $x = 0$, indicating that the tether is operating above its minimum tension criteria. However this scenario was a validation test to observe how the controller reacts to real-world modeling errors, and the controller does not show signs of instability, or steadily

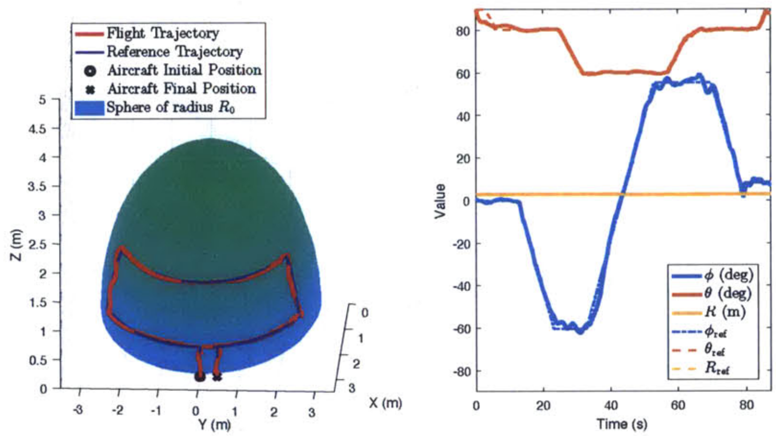

Figure 6-13: Spherical Controller Indoor Linear Density Testing: Trajectory and State Information

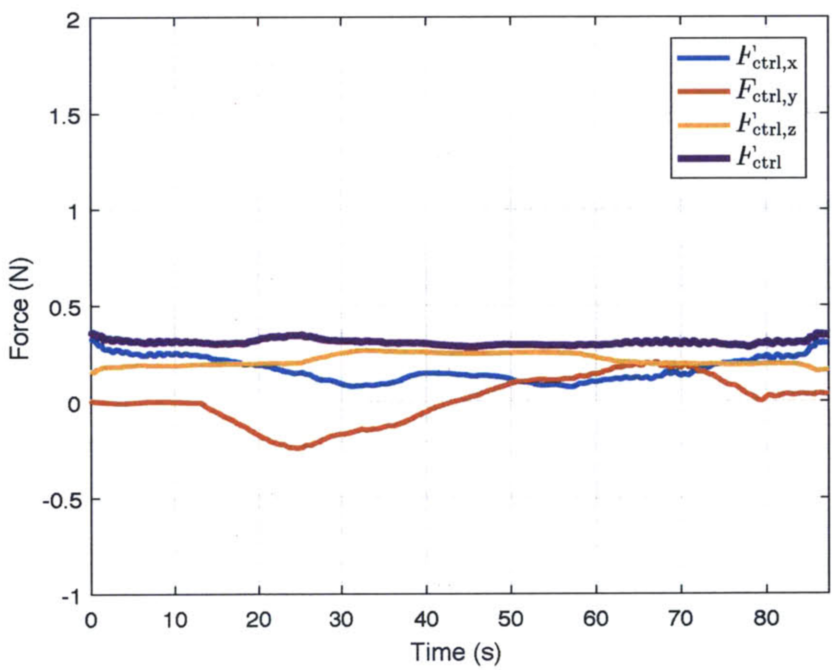

Figure 6-14: Spherical Controller Indoor Linear Density Testing: Control Outputs

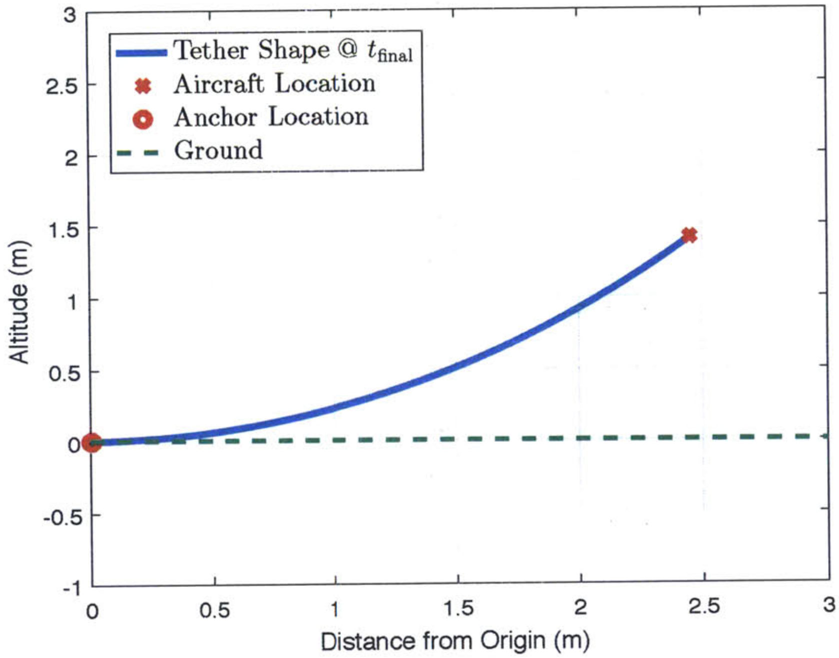

Figure 6-15: Spherical Controller Indoor Linear Density Testing: Tether Shape at $t = 40sec$

increasing control effort.

6.3.2.3 Reduced Tether Length L

For this validation test of the spherical position controller, the controller was flown on the end of a shortened tether while the controller still operated with $L = 3m$, creating a situation where the aircraft was unable to reach the desired reference position. The aircrafts state and trajectory are shown in Figure 6-16. The state error is shown in Figure 6-17, and corresponding control error integrators are shown in Figure 6-18. Figure 6-19 show the spherical position controllers control outputs, and Figure 6-20 show the shape of the tether at $t = 40sec$.

This test was particularly important because it emulated a condition that is very dangerous for a Cartesian control system. During this validation test, the tether was shortened such that the multirotor was unable to reach the R_{ref} location, with $L < R_{\text{ref}}$. Due to the constant large error in R, the Cartesian position control system

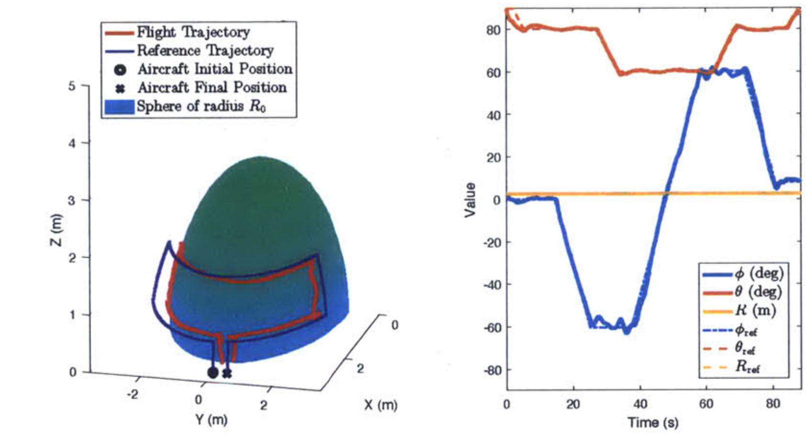

Figure 6-16: Spherical Controller Indoor Reduced Length Testing: Trajectory and State Information

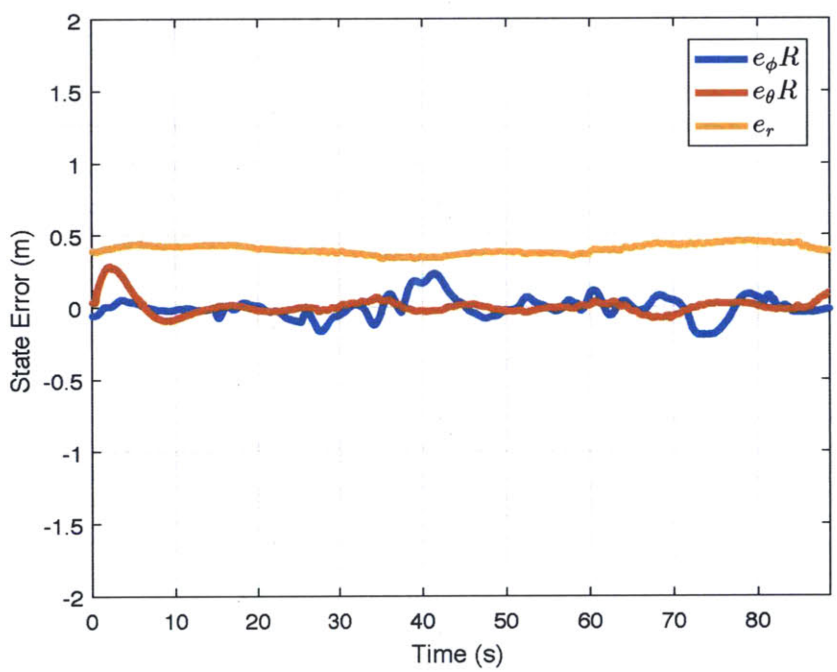

Figure 6-17: Spherical Controller Indoor Reduced Length Testing: State Error

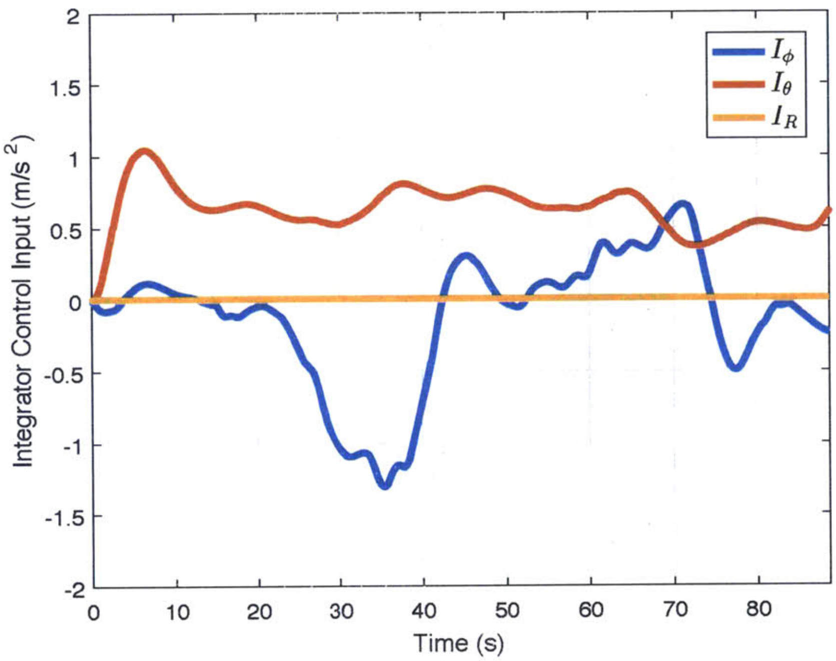

Figure 6-18: Spherical Controller Indoor Reduced Length Testing: Control Integrators

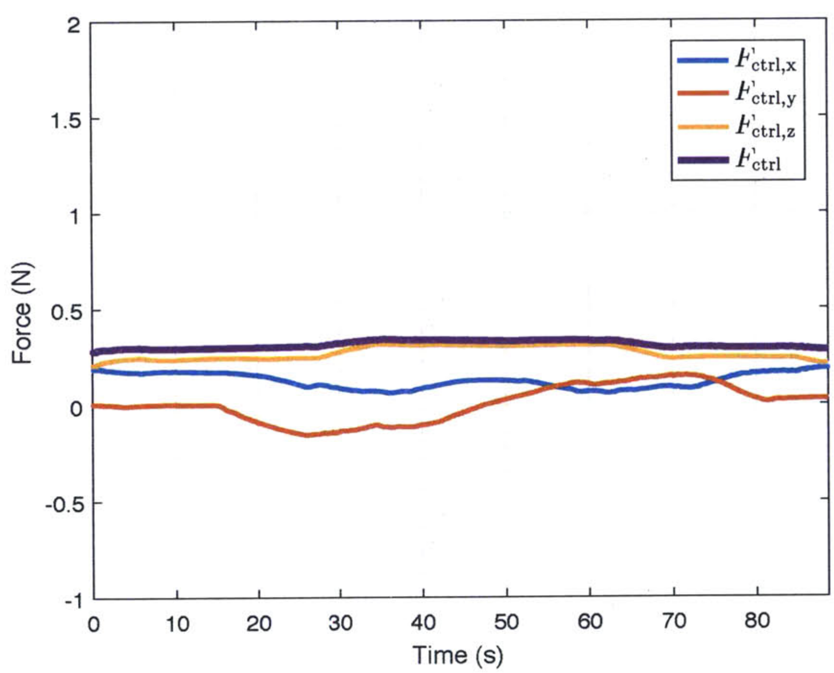

Figure 6-19: Spherical Controller Indoor Reduced Length Testing: Control Outputs

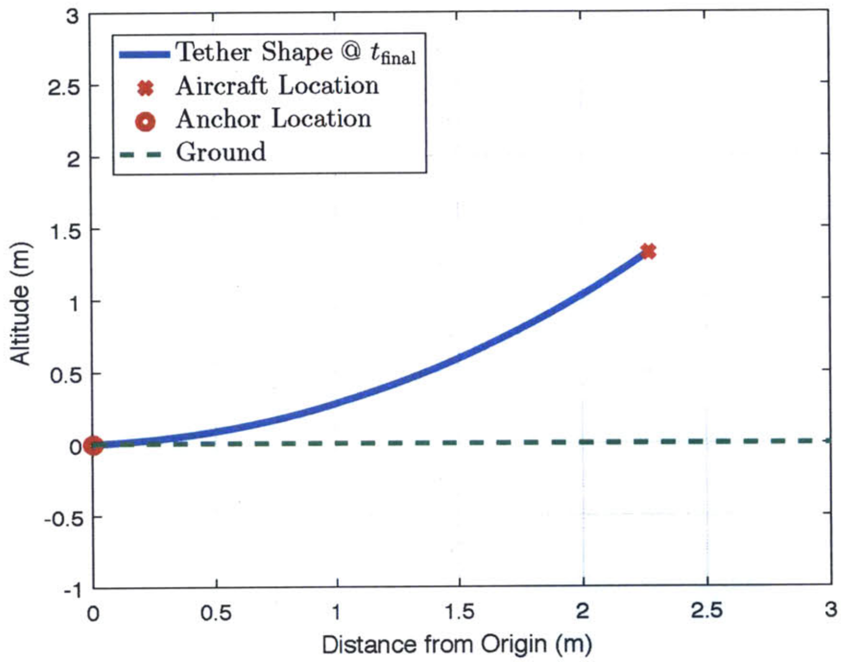

Figure 6-20: Spherical Controller Indoor Reduced Length Testing: Tether Shape at $t = 40sec$

would quickly integrate this error and create excessive and increasing tension on the tether, even though the vehicle would never be able to reach R_{ref}.

In this test, the spherical position controller performed as it was designed. It accurately tracked the reference trajectory and reduced steady state error in ϕ and θ, while allowing error in R and maintaining adequate tension on the tether. Figure 6-18 and 6-19 shows that neither integrators are diverging and the control effort is relatively constant over the course of the flight. Figure 6-20 shows that the tether is operating slightly above the minimum tension condition, but is expected as the tether is lighter than expected, similar to the previous validation test of reducing the linear density of the tether. Over the course of the trajectory, the controller shows good performance and no signs of instability or divergence.

6.3.2.4 Long Tether Length

For this validation test of the spherical position controller, the controller was flown on the end of a longer tether, where $L = 10m$. The aircrafts state and trajectory are shown in Figure 6-21. Figure 6-22 shows the spherical position controllers integrator control outputs, and Figure 6-23 shows the shape of the tether at $t = 20sec$.

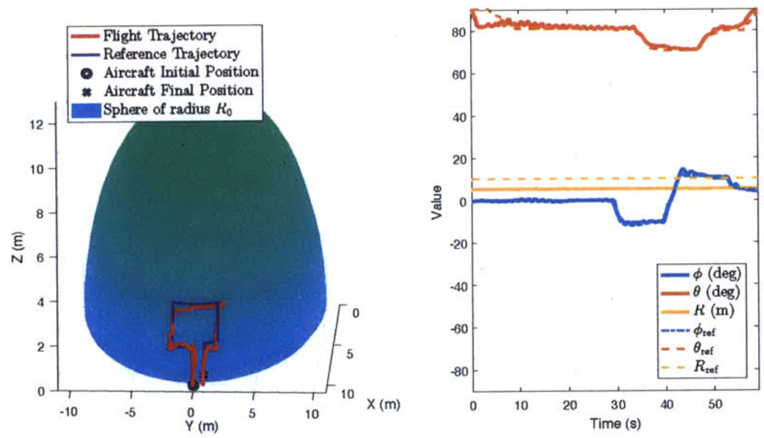

Figure 6-21: Spherical Controller Indoor Long Tether Testing: Trajectory and State Information

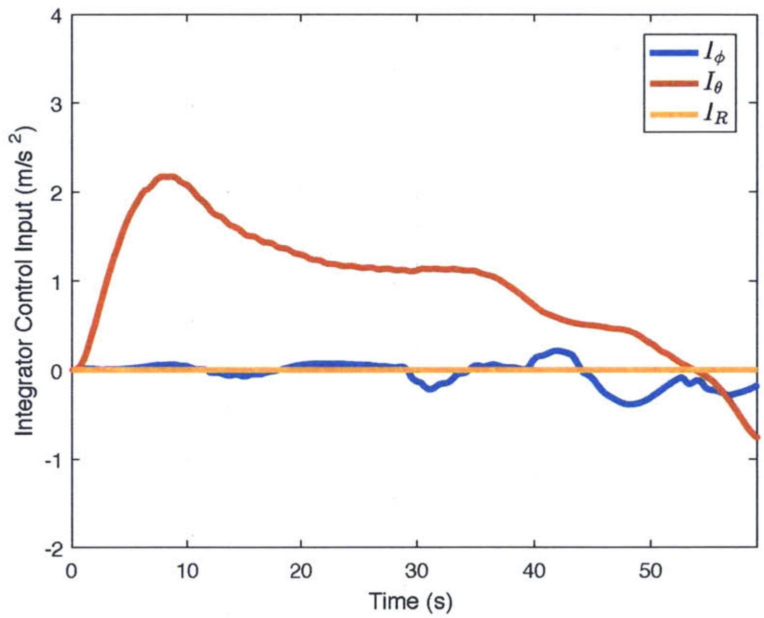

Figure 6-22: Spherical Controller Indoor Long Tether Testing: Integrator Control Outputs

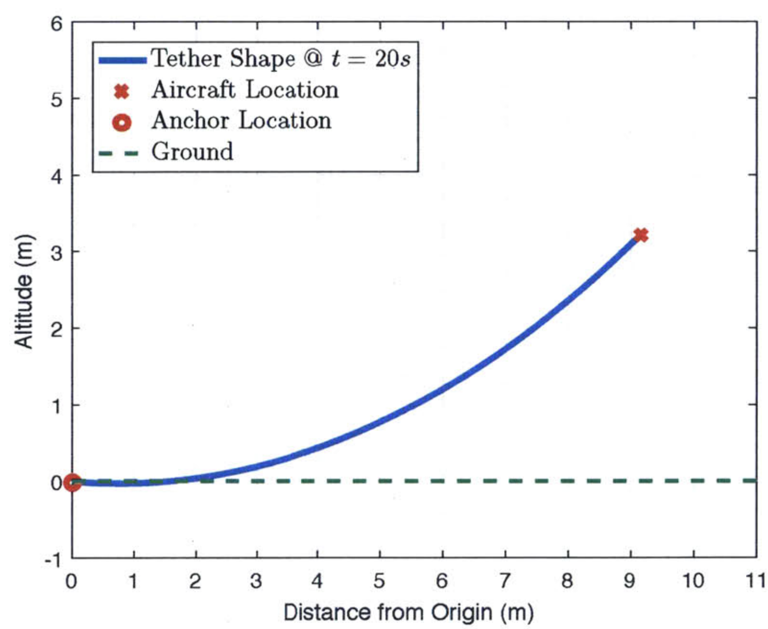

Figure 6-23: Spherical Controller Indoor Long Tether Testing: Tether Shape at $t = 20sec$

This final validation test of the spherical position controller was to confirm that the controller can operate at different tether lengths without modification of the controller gains or aside from the tether length L. Figure 6-21 shows that the system can follow the reference trajectory accurately. The control effort from the spherical position controller in Figure 6-22 show that a larger control force is required than the previous validation tests, however Figure 6-23 shows that the tether is operating at its minimum tension condition.

6.3.2.5 Validation Testing Conclusion

These validation tests aimed to evaluate the controllers ability to handle a variety of external disturbances and modeling errors while operating on a real aircraft and in a real world environment. The wind test showed the aircraft remained stable and was able to follow the reference trajectory in the presence of an external force acting upon both the aircraft and the tether system. Changing the tether's modeled linear density showed the controllers ability to compensate for real modeling and parameter errors within the controller and controller feed forward models. Testing the system with a tether taht is shorter than expected demonstrated the importance of the controllers lack of an state error integrator in the R direction, as well as the robustness compared to the traditional Cartesian system that this proposed controller was design to replace for tethered operations. The final test demonstrated the controllers ability to use a full range of tether lengths without need to modify controller gains or structure. These tests successfully established explicit confidence in the controller such that it is ready for implementation and operation in an outdoor multirotor system.

Chapter 7

Conclusion

7.1 Summary

This thesis details the motivation, design, and testing of a spherical position control system for a multirotor unmanned aircraft that is operating on the end of a tether. This proposed controller was designed to overcome a series of inherent problems with the traditional Cartesian position control system when operating in a constrained flight environment. The spherical position controller overcomes these problems by shifting into a spherical coordinate system, using the tether dynamics as a feed forward control model, and calculating reference commands that minimize tether tension subject to predefined constraints during flight. This controller structure allows a multirotor aircraft to fly on the end of a fixed length tether without expending excess energy, or risking flight instability due to actuator saturation. During simulated flight testing the spherical position controller showed a 35.7% decrease in tether tension, and during indoor flight testing the spherical position controller exhibited an 8.4% decrease in power consumption over the traditional Cartesian position controller.

The main contributions of this thesis are the motivated proposal, design derivation, implementation, and testing of a spherical position control system for a multirotor UAV that operates on the end of a fixed length tether.

Chapter 1 outlines the project overview, current trends in the aerospace community regarding the recent interest in multirotor aircraft, and a review of recent work regarding multirotor tethered flight.

Chapter 2 provides a full derivation of a multirotor rigid-body dynamics, and a full derivation of the tether system shape and dynamics. The multirotor aircraft dynamics models was utilized in the attitude control system of the spherical position controller. The tether system dynamics were used as both a feed forward control model, as well as minimum tension reference command generation algorithm.

In Chapter 3, a detailed design and discussion of the spherical position control system is presented. This process begins with the inherent problems with the traditional Cartesian position control systems, which motivate the three major components of the spherical position control system. The three major controller components are the spherical PID/PD controller, a tether dynamics feed forward model, and a reference command generation algorithm. The spherical position controller generates attitude commands for the multirotor aircraft, which are then converted to aircraft actuator commands using a typical attitude control system.

The methods used for implementing the spherical position controller is outlined in Chapter 4. The controller was implemented into a simulated flight environment, followed by the indoor flight space in the Aerospace Controls Laboratory. This chapter covers the tether dynamics numerical solving methods, aircraft and tether physical parameters, as well as a flight software overview.

The experimental design and results of the spherical position controllers simulated and indoor flight testing is presented in Chapters 5 and 6 respectively. These two testing regimes were broken into two sections: verification testing and validation testing. Verification testing of the proposed control system included confirmation that the controller succeeded in accomplishing the design goals and motivations. Validation testing consisted of confirming that the controller worked in a variety of real world flight conditions, such as the presence of modeling error and external disturbances.

7.2 Limitations and Future Work

There are a number of areas for future work regarding the flight control of a multirotor aircraft flying on a tether system. Three of these areas include introducing dynamic operation, designing and implementing a wind drag model and testing the system in a wind tunnel, and implementing the system into an outdoor testing environment.

The spherical position controller presented in this thesis used a tether dynamics model that was approximated to be operating in static conditions. Practically, this required the aircraft be flying slowly on the end of the tether system, as the dynamic forces (for example, centrifugal acceleration) are not modeled in the feed forward control model. The controller was able to handle all unmodeled forces in the validation testing, however these dynamics can be incorporated into the system model.

Along a similar path, the current spherical position controller compensates for forces due to wind drag using the controllers error integrators. The feed forward control system could be further extended to include an estimation of the drag force upon the aircraft and tether system, and correct for the external force. This extension would also require an extension of the tether dynamics model to a three-dimensional catenary curve, as the curvature of the tether system could no longer be approximated by the two dimensional solution.

Lastly, many of the disturbances discussed and emulated in the simulated and indoor flight testing were derived from outdoor flight conditions. It would be advantageous to extend the validation testing performed in this thesis to an outdoor environment, where vehicle state, tether dynamics, and environmental conditions are not perfect. Implementing this system into an outdoor aircraft system would require significant software and hardware changes from the indoor flight testing implementation, as the multirotors autopilot will no longer have access to Vicon information for state estimation, rather it will rely on GPS measurements which adds an additional layer of modeling error into the system. However most use cases for a multirotor aircraft exist outdoors or similar environments without precise state knowledge, thus this extension would be very valuable for the future application of the proposed spherical position controller.

There is significant future work that allows both the further development of the spherical position controller algorithm and the advance application of tethered aircraft. This project aimed specifically on unmanned multirotor aircraft operating behind a ship, however there are a variety of applications for tethering multirotor aircraft, as the tether could be used to transmit power to the aircraft or restrict its area of operation. One example is utilizing a tethered UAV as a communication relay [2]. There are also other applications where aircraft are required to operate in a constrained environment which could benefit from the augmented constraint and aircraft dynamics, such as tethered wind turbines for power generation [1].

Appendix A

A.1 Cartesian Feedback PID Control

This section will outline a traditional Cartesian feedback position control system, which is widely used as a basic position control algorithm and is similar in structure to that presented in [3]. This controller was used as a baseline configuration upon which to compare the spherical position controller that is presented in this thesis.

A.1.1 Position Control

The position control loop (also referred to as the outer control loop) takes as inputs the reference position and velocity and the measured position and velocity. The measured values are fed into the outer control loop from the system dynamics. The reference values are inputs into the system as a whole and can be set directly or through a trajectory generator. The position control loop is a two step process. First, desired accelerations are computed using the position and velocity inputs. The desired accelerations are then used to compute a motor throttle command and desired attitude and angular rate for the quadrotor.

To compute the desired acceleration vector, a position error vector ($\mathbf{e}_{pos}$) and a velocity error vector ($\mathbf{e}_{rate}$) are calculated

$$\mathbf{e}_{pos} = \begin{bmatrix} x_{des} \\ y_{des} \\ z_{des} \end{bmatrix} - \begin{bmatrix} x_{meas} \\ y_{meas} \\ z_{meas} \end{bmatrix} \tag{A.1}$$

$$\mathbf{e}_{vel} = \begin{bmatrix} \dot{x}_{des} \\ \dot{y}_{des} \\ \dot{z}_{des} \end{bmatrix} - \begin{bmatrix} \dot{x}_{meas} \\ \dot{y}_{meas} \\ \dot{z}_{meas} \end{bmatrix} \tag{A.2}$$

where $\begin{bmatrix} x_{des} & y_{des} & z_{des} \end{bmatrix}^T$ is the desired position vector, $\begin{bmatrix} x_{meas} & y_{meas} & z_{meas} \end{bmatrix}^T$ is the measured position vector, $\begin{bmatrix} \dot{x}_{des} & \dot{y}_{des} & \dot{z}_{des} \end{bmatrix}^T$ is the desired velocity vector, and $\begin{bmatrix} \dot{x}_{meas} & \dot{y}_{meas} & \dot{z}_{meas} \end{bmatrix}^T$ is the measured velocity vector. The errors are mapped into acceleration commands using a PID controller

$$\begin{bmatrix} \ddot{x}_{cmd} \\ \ddot{y}_{cmd} \\ \ddot{z}_{cmd} \end{bmatrix} = K_{P,pos}\mathbf{e}_{pos} + K_{I,pos}\int_0^t \mathbf{e}_{pos} + K_{D,pos}\mathbf{e}_{vel} \tag{A.3}$$

where $K_{P,pos}$, $K_{I,pos}$, and $K_{D,pos}$ are 3x3 diagonal, positive definite gain matrices. Gravity is then taken into account to compute the desired accelerations

$$\begin{bmatrix} \ddot{x}_{des} \\ \ddot{y}_{des} \\ \ddot{z}_{des} \end{bmatrix} = \begin{bmatrix} \ddot{x}_{cmd} \\ \ddot{y}_{cmd} \\ \ddot{z}_{cmd} \end{bmatrix} + \begin{bmatrix} 0 \\ 0 \\ g \end{bmatrix}. \tag{A.4}$$

To compute the motor throttle command (h_{cmd}), the desired accelerations are turned into forces, summed, and mapped to a throttle command

$$h_{cmd} = \frac{1}{k_{motor}} m(\ddot{x}_{des} + \ddot{y}_{des} + \ddot{z}_{des}) \tag{A.5}$$

using an experimentally-determined motor constant (k_{motor}). The motor throttle command is then output to the inner control loop.

A.1.2 Desired Attitude Generation

The second step of the outer control loop computes the desired attitude and angular rate given the desired accelerations. For this step, the attitude of the vehicle in the inertial frame is described by quaternion $\mathbf{q}$ and the angular rates in the body frame B defined as Ω_b. The quaternion $\mathbf{q}$ is defined as

$$\mathbf{q} = \begin{bmatrix} q^0 \\ \vec{q} \end{bmatrix}$$

where q^0 is the scalar component and $\vec{q}$ is the vector component. The desired force vector in the inertial frame is defined as

$$\mathbf{F}_{i,des} = m(\ddot{x}_{des}\mathbf{i}_x + \ddot{y}_{des}\mathbf{i}_y + \ddot{z}_{des}\mathbf{i}_z) \tag{A.6}$$

and $\mathbf{F}_{b,des}$ is the desired force vector in the body frame. Equation 3.11 in [3] gives a relation between the desired attitude quaternion ($\mathbf{q}_{des}$) and the desired force vector

$$\begin{bmatrix} 0 \\ \bar{\mathbf{F}}_{i,des} \end{bmatrix} = \mathbf{q}^*_{des} \otimes \begin{bmatrix} 0 \\ \bar{\mathbf{F}}_{\mathbf{b,des}} \end{bmatrix} \otimes \mathbf{q}_{des} \tag{A.7}$$

where $\bar{\mathbf{F}}_{\mathbf{b,des}}$ and $\bar{\mathbf{F}}_{\mathbf{i,des}}$ are unit vectors,

$$\bar{\mathbf{F}}_{\mathbf{b,des}} = \frac{\mathbf{F}_{\mathbf{b,des}}}{||\mathbf{F}_{\mathbf{b,des}}||} = \begin{bmatrix} 0 & 0 & 1 \end{bmatrix}^T \tag{A.8}$$

$$\bar{\mathbf{F}}_{\mathbf{i,des}} = \frac{\mathbf{F}_{\mathbf{i,des}}}{||\mathbf{F}_{\mathbf{i,des}}||}. \tag{A.9}$$

$\mathbf{q}^*_{des}$ is the quaternion conjugate of $\mathbf{q}_{des}$, and $\otimes$ is the quaternion multiplication operator. In this formulation, $\mathbf{q}_{des}$ corresponds to the quadrotor attitude (not including desired yaw) that aligns the body frame force vector with the inertial force vector.

The minimum-angle quaternion rotation between the two force vectors in $\mathbb{R}^3$ is [10]

$$\mathbf{q}_{des} = \frac{1}{\sqrt{2(1+\bar{\mathbf{F}}_{i,des}^T\bar{\mathbf{F}}_{b,des})}} \begin{bmatrix} 1+\bar{\mathbf{F}}_{i,des}^T\bar{\mathbf{F}}_{b,des} \\ \bar{\mathbf{F}}_{i,des}^T \times \bar{\mathbf{F}}_{b,des} \end{bmatrix}. \tag{A.10}$$

Note that Equation A.10 does not produce a unique desired attitude quaternion. In particular, quaternions define the special orthogonal group S0(3) in two ways. This results in $\mathbf{q}$ and $-\mathbf{q}$ defining the same attitude [3]. To remove this ambiguity, the sign of $\mathbf{q}_{des}$ is chosen to match the sign of $\mathbf{q}_{des}$ at the previous time step.

The desired attitude quaternion is then rotated by the desired yaw angle (ψ_{des}) to compute the full desired vehicle attitude quaternion

$$\mathbf{q}_{des,f} = \mathbf{q}_{des} \otimes \begin{bmatrix}\cos(\psi_{des}/2) & 0 & 0 & \sin(\psi_{des}/2)\end{bmatrix}^T. \tag{A.11}$$

In the Simulink implementation of the system, the desired attitude quaternion is converted into Euler angles and output to the inner control loop.

The desired angular rate ($\Omega_{b,des}$) is calculated by taking the time derivative of $\bar{F}_{i,des}$. From [3], the angular rates in the x and y body axes is

$$(\Omega_{b,des})_{xy} = \bar{\mathbf{F}}_{i,des} \times \dot{\bar{\mathbf{F}}}_{i,des} \tag{A.12}$$

where the time derivative of the inertial desired force vector is

$$\dot{\bar{\mathbf{F}}}_{i,des} = \frac{\dot{\mathbf{F}}_{i,des}}{||\mathbf{F}_{i,des}} - \frac{\mathbf{F}_{i,des}(\mathbf{F}_{i,des}^T\dot{\mathbf{F}}_{i,des})}{||\mathbf{F}_{i,des}||^3}. \tag{A.13}$$

The z component of the angular velocity (yaw rate), is directly computed from the input yaw command

$$(\Omega_{b,des})_z = \dot{\psi}_{des}. \tag{A.14}$$

The desired angular rate of the quadrotor is then output to the inner attitude control loop.

A.1.2.1 Attitude Control

The attitude control loop (also referred to as the inner control loop) takes as inputs desired attitude and angular rates from the outer control loop and measured attitude and angular rates from the system dynamics. Its purpose is to output motor commands to the system dynamics.

$$\mathbf{e}_{att} = \begin{bmatrix} \phi_{des} \\ \theta_{des} \\ \psi_{des} \end{bmatrix} - \begin{bmatrix} \phi_{meas} \\ \theta_{meas} \\ \psi_{meas} \end{bmatrix} \tag{A.15}$$

$$\mathbf{e}_{rate} = \begin{bmatrix} p_{des} \\ q_{des} \\ r_{des} \end{bmatrix} - \begin{bmatrix} p_{meas} \\ q_{meas} \\ r_{meas} \end{bmatrix} \tag{A.16}$$

where $\begin{bmatrix} \phi_{des} & \theta_{des} & \psi_{des} \end{bmatrix}^T$ is the desired attitude vector, $\begin{bmatrix} \phi_{meas} & \theta_{meas} & \psi_{meas} \end{bmatrix}^T$ is the measured attitude vector, $\begin{bmatrix} p_{des} & q_{des} & r_{des} \end{bmatrix}^T$ is the desired angular rate vector, and $\begin{bmatrix} p_{meas} & q_{meas} & r_{meas} \end{bmatrix}^T$ is the measured angular rate. The errors are mapped into roll, pitch, and yaw commands (ϕ_{cmd}, θ_{cmd}, and ψ_{cmd}, respectively) using a PID controller

$$\begin{bmatrix} \phi_{cmd} \\ \theta_{cmd} \\ \psi_{cmd} \end{bmatrix} = K_{P,att}\mathbf{e}_{att} + K_{I,att}\int_0^t \mathbf{e}_{att} + K_{D,att}\mathbf{e}_{rate} \tag{A.17}$$

where $K_{P,att}$, $K_{I,att}$, and $K_{D,att}$ are 3x3 diagonal, positive semi-definite gain matrices. The angle commands are then used with the motor throttle input (h_{cmd}) to calculate motor commands

$$\begin{bmatrix} m_1 \\ m_2 \\ m_3 \\ m_4 \end{bmatrix} = \begin{bmatrix} 1 & 0 & -1 & -1 \\ 1 & -1 & 0 & 1 \\ 1 & 0 & 1 & -1 \\ 1 & 1 & 0 & 1 \end{bmatrix} \begin{bmatrix} h_{cmd} \\ \phi_{cmd} \\ \theta_{cmd} \\ \psi_{cmd} \end{bmatrix}. \tag{A.18}$$

In simulation, the motor commands are then converted to motor thrusts (F_1, F_2, F_3, F_4) in Newtons using an experimentally-determined motor constant (k_{motor}) and then saturated to within the actuator limits

$$F_k = k_{motor} m_k. \tag{A.19}$$

The thrust forces are then fed into the system dynamics as the outputs of this control loop.

Appendix B

This appendix contains additional figures from simulated and indoor flight testing in Chapters 5 and 6.

B.1 Additional Simulation Flight Testing Figures

B.1.1 Verification Testing

B.1.1.1 Spherical PID/PD Position Controller

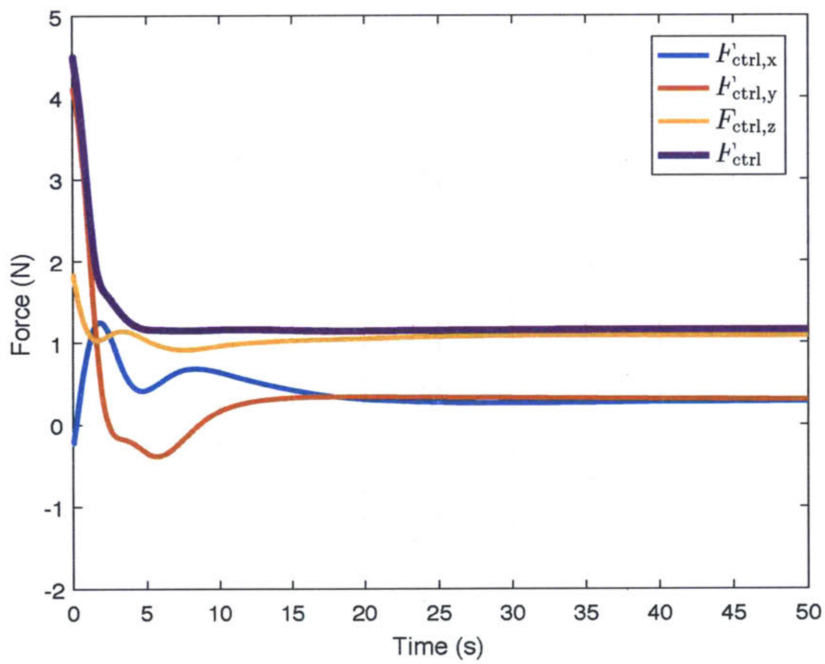

Figure B-1: Spherical PID/PD Position Controller: Position Controller Force Output

B.1.1.2 Spherical PID/PD Position Controller with Feed Forward Control

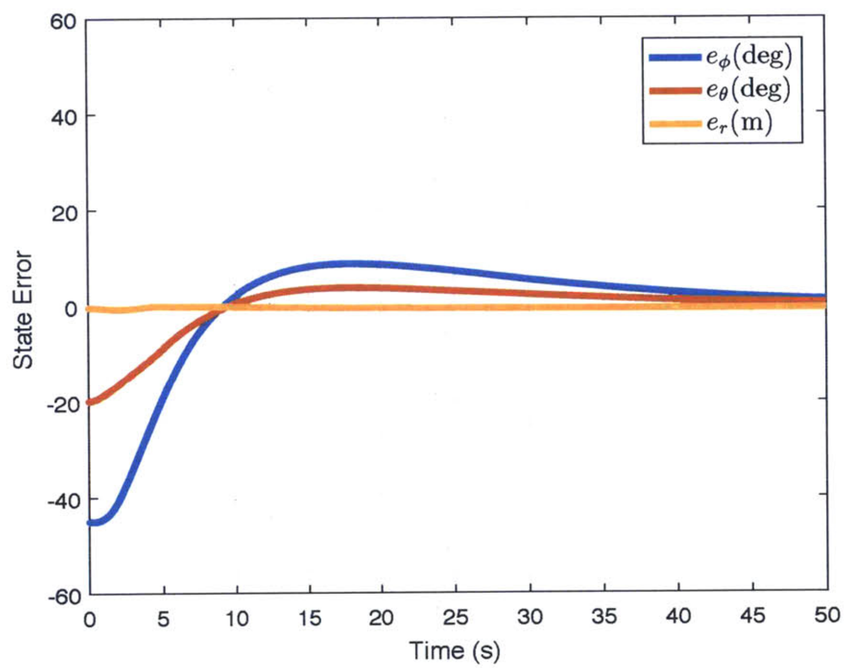

Figure B-2: Spherical PID/PD Position Controller with FF: State Error

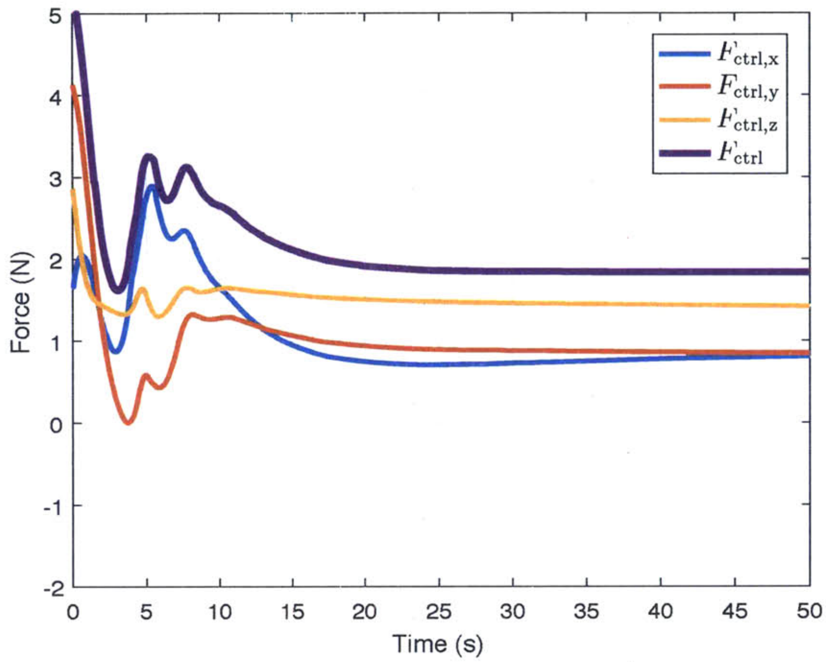

Figure B-3: Spherical PID/PD Position Controller with FF: Position Controller Force Output

B.1.1.3 Spherical PID/PD Position Controller with Feed Forward Control and Reference Command Generation

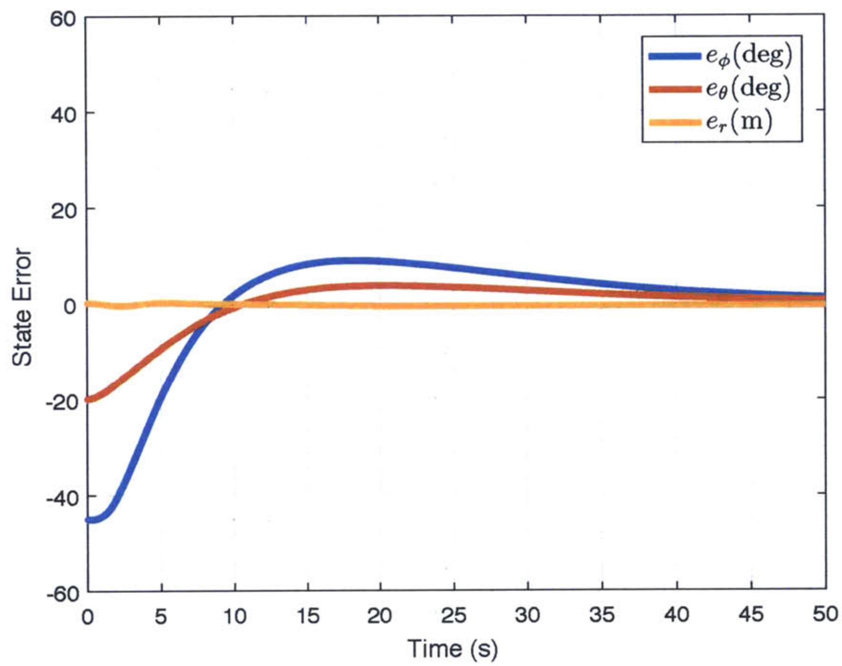

Figure B-4: Spherical PID/PD Position Controller with FF and RCG: State Error

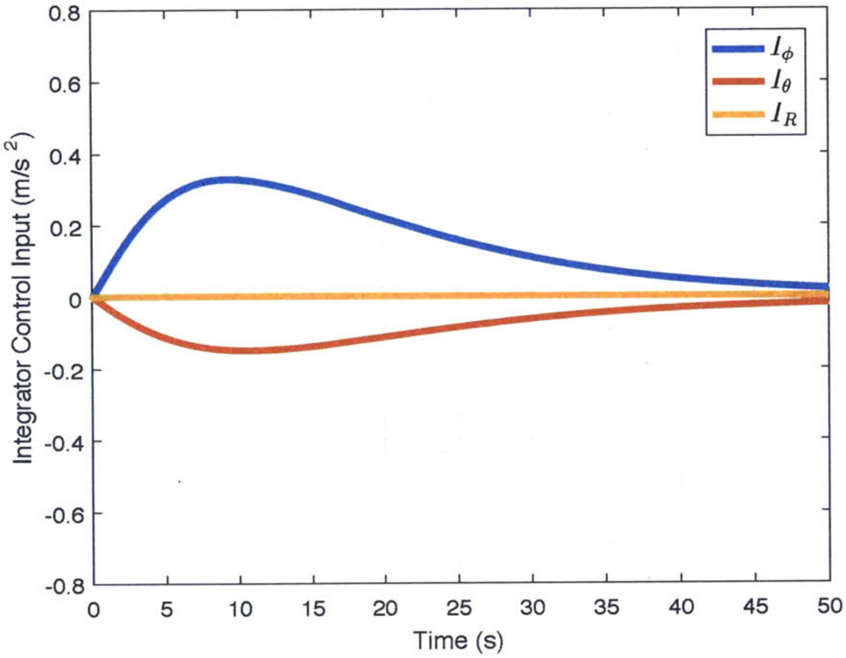

Figure B-5: Spherical PID/PD Position Controller with FF and RCG: PID Control Integrators

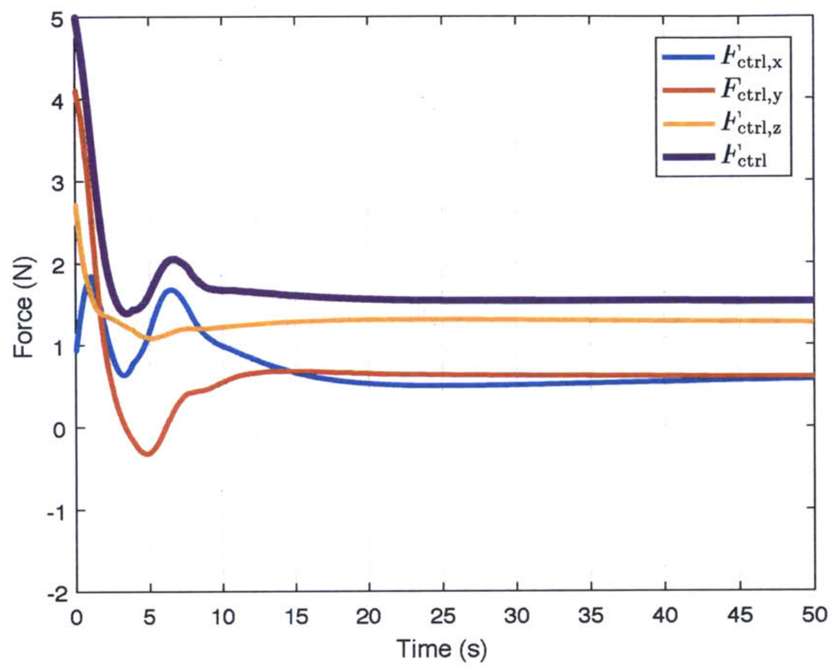

Figure B-6: Spherical PID/PD Position Controller with FF and RCG: Position Controller Force Output

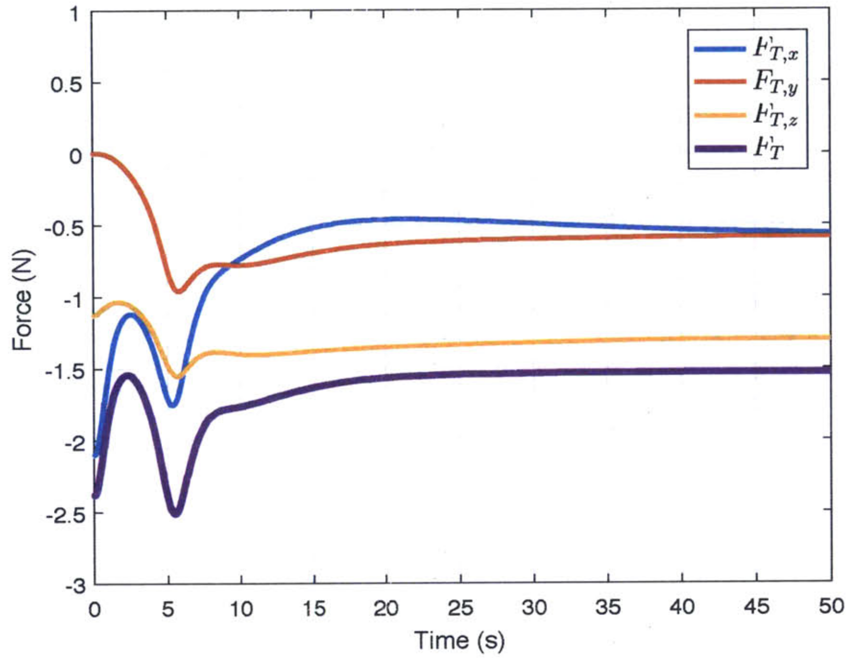

Figure B-7: Spherical PID/PD Position Controller with FF and RCG: Tether Tension

B.1.2 Validation Testing

B.1.2.1 Wind Force on Aircraft and Tether

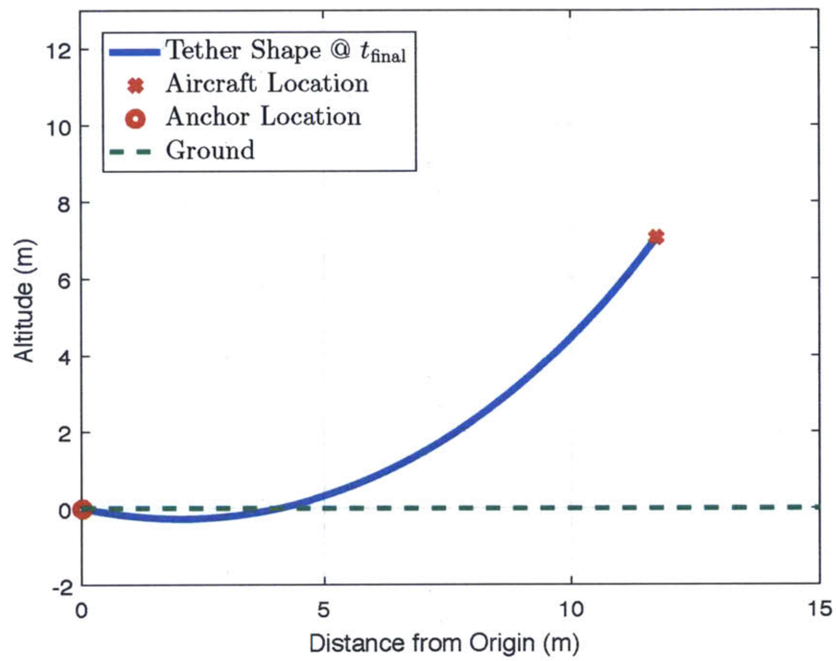

Figure B-8: Wind Validation Testing: Tether Shape

B.1.2.2 Incorrect Linear Density

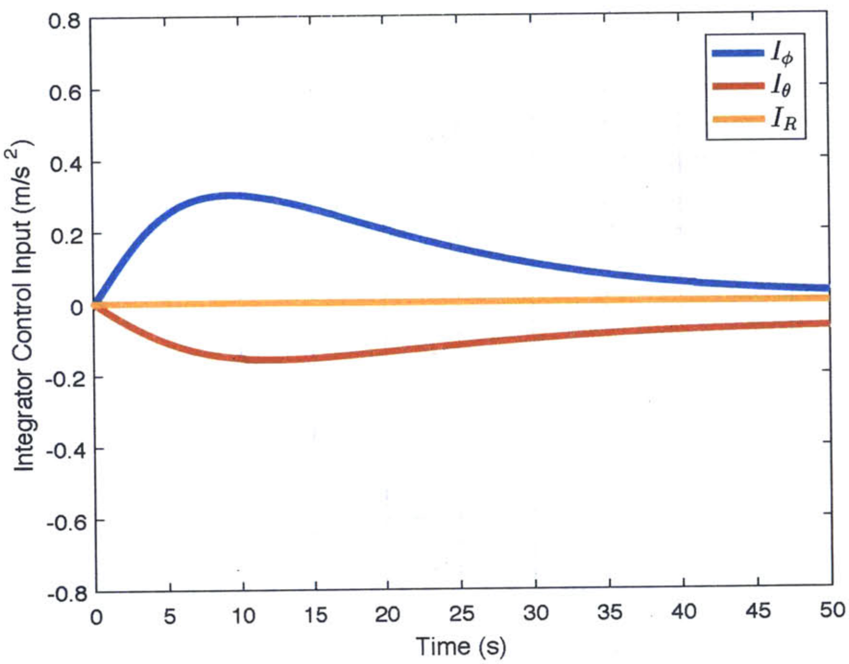

Figure B-9: Tether Linear Density Validation Testing: PID Control Integrators

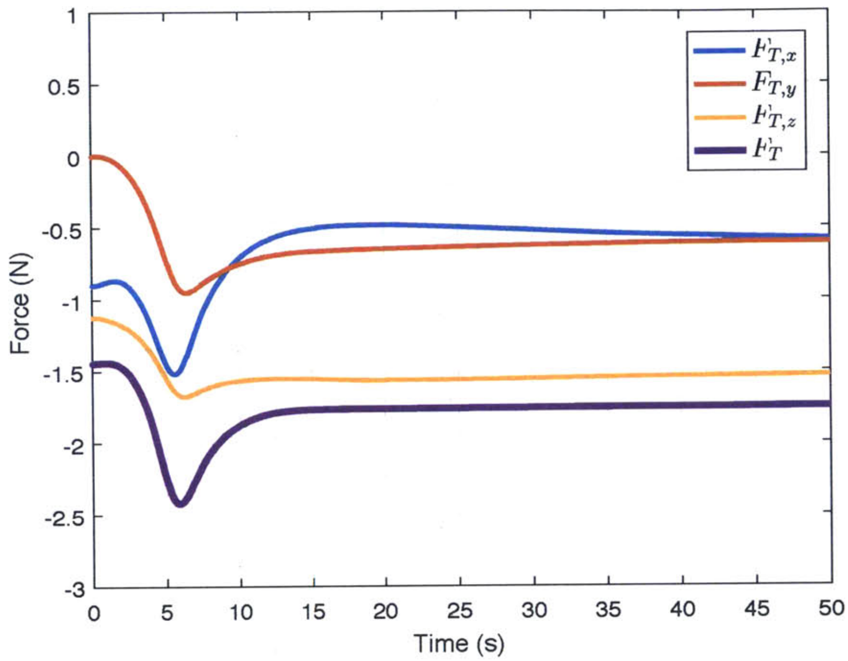

Figure B-10: Tether Linear Density Validation Testing: Tether Tension

B.1.2.3 Increased Tether Length

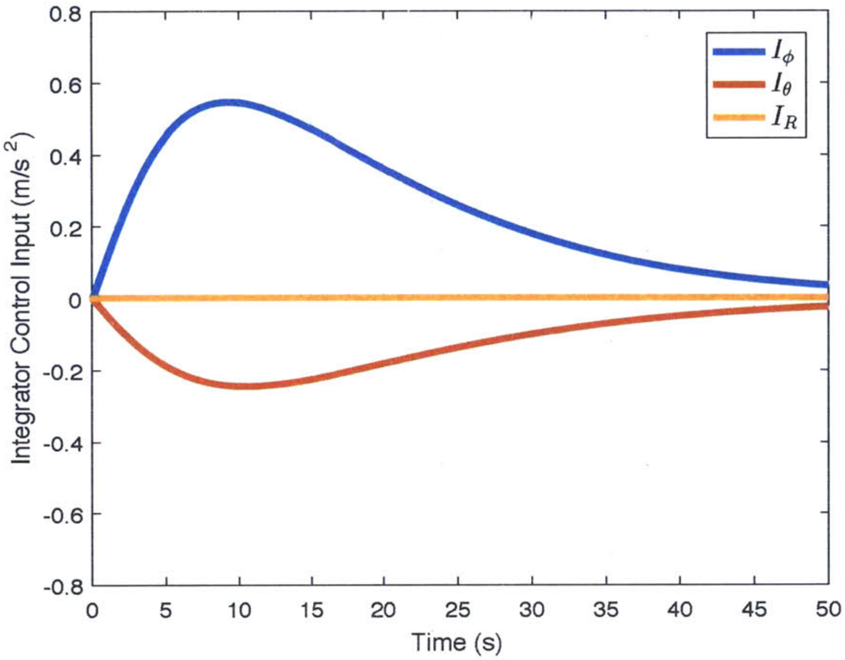

Figure B-11: Tether Length Increase Validation Testing: PID Control Integrators

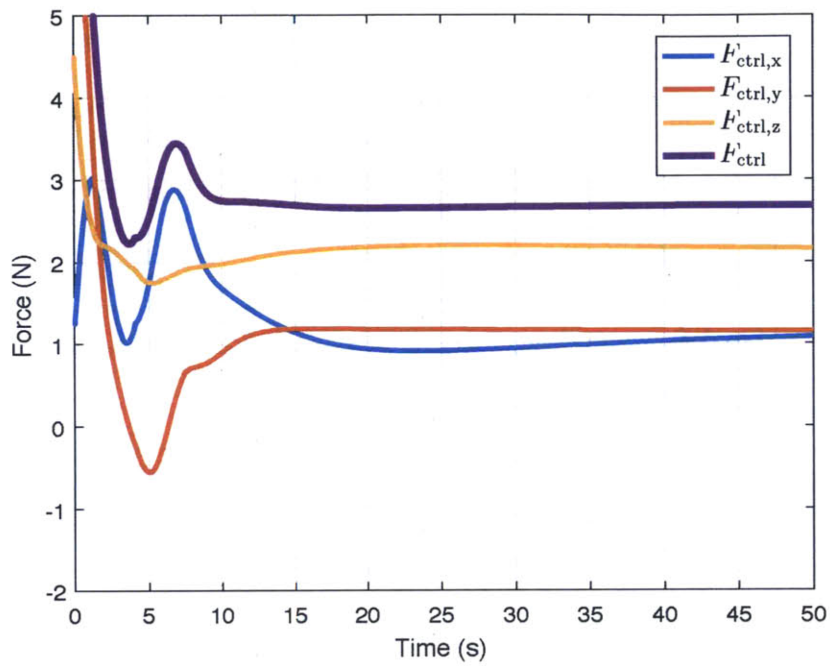

Figure B-12: Tether Length Increase Validation Testing: Position Controller Force Output

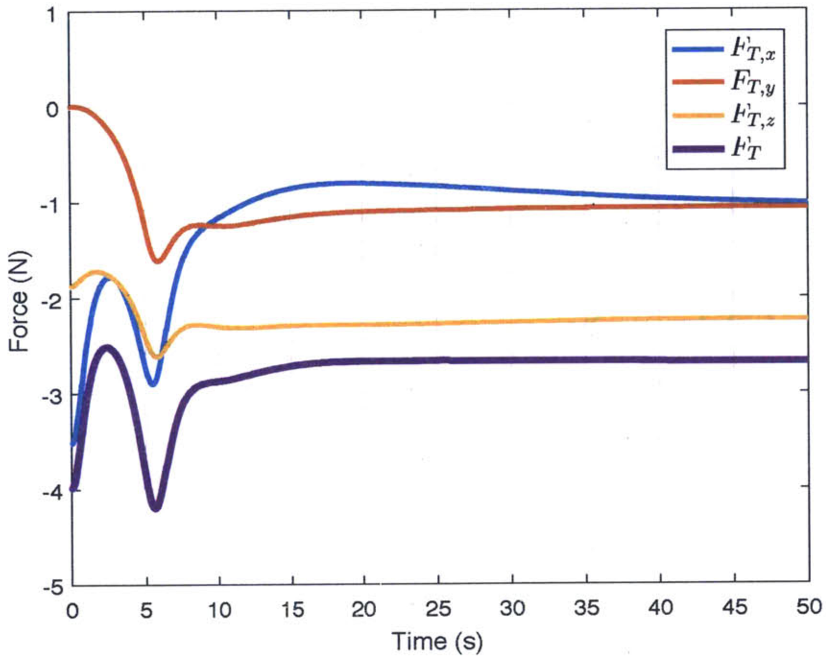

Figure B-13: Tether Length Increase Validation Testing: Tether Tension

B.2 Additional Indoor Flight Testing Figures

B.2.1 Validation Testing

B.2.1.1 Wind Testing

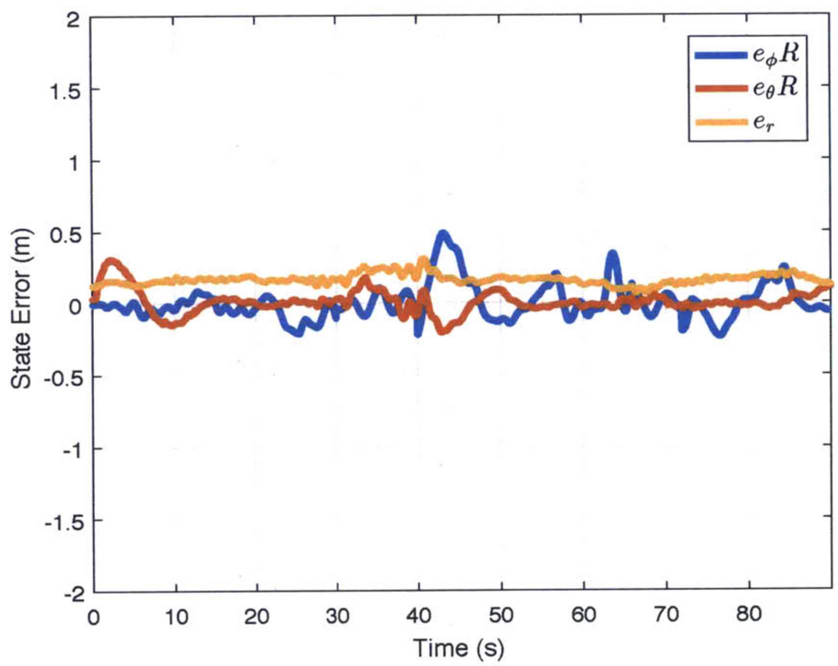

Figure B-14: Spherical Controller Indoor Wind Testing: State Error

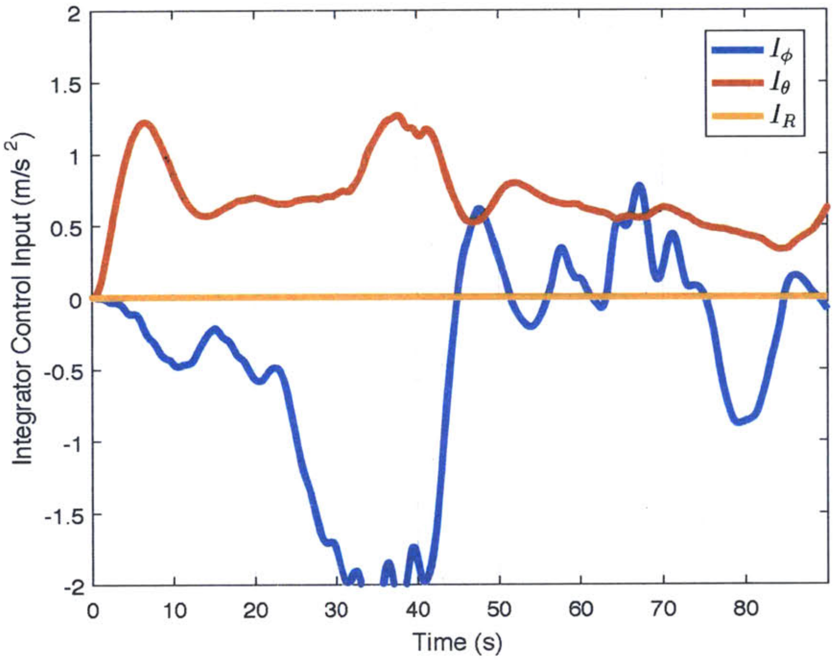

Figure B-15: Spherical Controller Indoor Wind Testing: Control Integrators

B.2.1.2 Incorrect Tether Linear Density

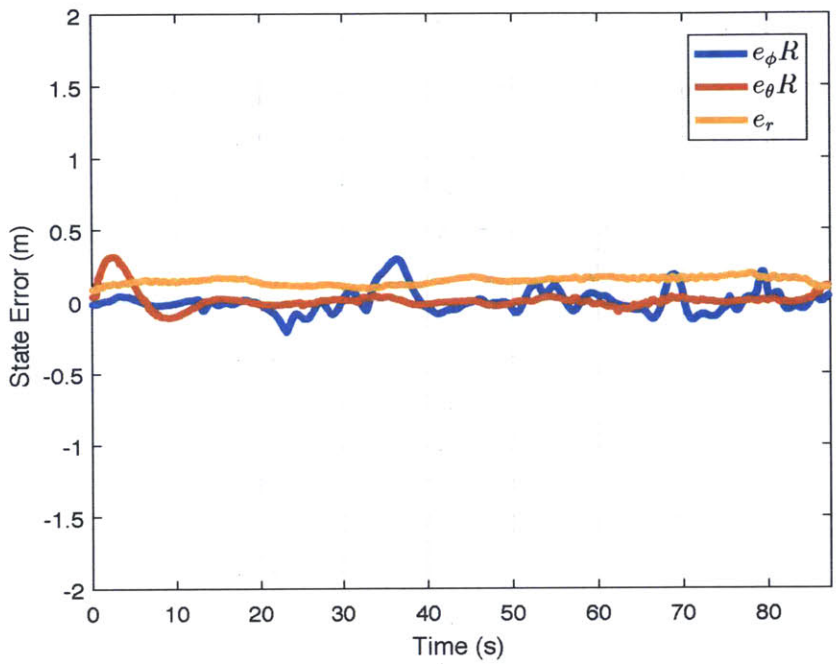

Figure B-16: Spherical Controller Indoor Linear Density Testing: State Error

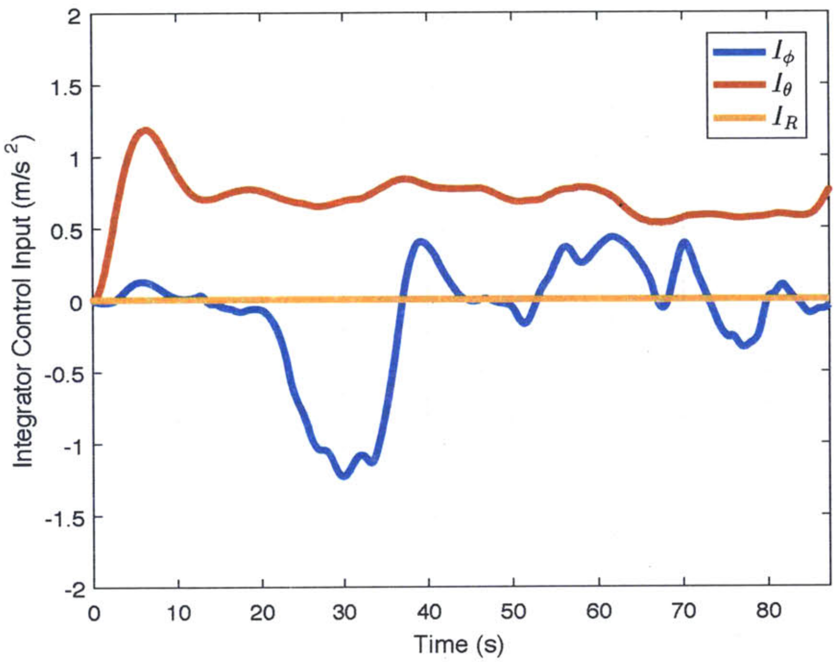

Figure B-17: Spherical Controller Indoor Linear Density Testing: Control Integrators

Bibliography

[1] M. Canale, L. Fagiano, M. Ippolito, and M. Milanese. Control of tethered airfoils for a new class of wind energy generator. In *Proceedings of the 45th IEEE Conference on Decision and Control*, pages 4020–4026, Dec 2006.

[2] D. H. Choi, S. H. Kim, and D. K. Sung. Energy-efficient maneuvering and communication of a single uav-based relay. *IEEE Transactions on Aerospace and Electronic Systems*, 50(3):2320–2327, July 2014.

[3] Mark Cutler. Design and control of an autonomous variable-pitch quadrotor helicopter. Master's thesis, Massachusetts Institute of Technology, Dept. of Aeronautics and Astronautics, Sept 2012.

[4] J. P. How, B. Behihke, A. Frank, D. Dale, and J. Vian. Real-time indoor autonomous vehicle test environment. *IEEE Control Systems*, 28(2):51–64, April 2008.

[5] The Mathworks Inc. Matlab and simulink 2016a. Natick, MA, June 2016.

[6] Daewon Lee, H. Jin Kim, and Shankar Sastry. Feedback linearization vs. adaptive sliding mode control for a quadrotor helicopter. *International Journal of Control, Automation and Systems*, 7(3):419–428, 2009.

[7] Creare LLC. Wake swarm project. Hanover, NH, June 2016.

[8] E. H. Lockwood. *Book of Curves*. Cambridge University Press, 1961. Cambridge Books Online.

[9] S. Lupashin and R. D'Andrea. Stabilization of a flying vehicle on a taut tether using inertial sensing. In *Intelligent Robots and Systems (IROS), 2013 IEEE/RSJ International Conference on*, pages 2432–2438, Nov 2013.

[10] F.L. Markley. Fast quaternion attitude estimation from two vector measurements. In *Journal of Guidance, Control, and Dynamics*, volume 25, pages 411–414, 2002.

[11] Tech. rep. Motion capture systems from vicon. Online, June 2015. `http://www.vicon.com/`.

[12] ROS. About ros. Online, June 2015. `http://www.ros.org/about-ros/`.

[13] L. A. Sandino, M. Bejar, K. Kondak, and A. Ollero. Improving hovering performance of tethered unmanned helicopters with nonlinear control strategies. In *Unmanned Aircraft Systems (ICUAS), 2013 International Conference on*, pages 443–452, May 2013.

[14] Luis A. Sandino, Manuel Bejar, Konstantin Kondak, and Anibal Ollero. On the use of tethered configurations for augmenting hovering stability in small-size autonomous helicopters. *Journal of Intelligent & Robotic Systems*, 70(1):509–525, 2012.

[15] K. Y. Wang, P. H. Lee, and S. K. Hung. Optimum electric cable selection for kite-like unmanned aerial vehicle. In *Advanced Intelligent Mechatronics (AIM), 2015 IEEE International Conference on*, pages 1537–1540, July 2015.

[16] James Wiken. Analysis of a quadrotor in forward flight. Master's project, Massachusetts Institute of Technology, Dept. of Aeronautics and Astronautics, June 2015.

[17] Li Yibo, Xie Qiling, and Han Jianda. Modeling and pid control of tethered unmanned quadrotor helicopter. In *Mechatronic Sciences, Electric Engineering and Computer (MEC), Proceedings 2013 International Conference on*, pages 258–262, Dec 2013.

[18] Bing Zhu and Wei Huo. Trajectory linearization control for a quadrotor helicopter. In *Control and Automation (ICCA), 2010 8th IEEE International Conference on*, pages 34–39, June 2010.